ALMA MATER STUDIORUM
UNIVERSITÀ DI BOLOGNA

DEPARTMENT OF PHYSICS AND ASTRONOMY ”A. RIGHI”

SECOND CYCLE DEGREE

PHYSICS

Optimisation of integrated luminosity of a circular collider in presence of levelled luminosity

Supervisor
Prof. Massimo Giovannozzi

Co-supervisors
Maria Aquilina
Dr Federico Capoani

Defended by
Edoardo Mazzola

Graduation Session December 2025

Academic Year 2024/2025

In mathematics, you don't know what you're going to find.
You just keep solving problems.

Katherine Johnson

Abstract

The performance of particle colliders is usually quantified by the *beam energy* and the *luminosity*. In fact, the integrated value of the latter is found to be proportional to the data collected by the detectors. A more efficient collection of physics events is obtained through maximisation of the integrated luminosity over the time allocated for physics. An increased efficiency has a direct impact on the physics discovery potential of a collider. In the context of the luminosity upgrade of the CERN Large Hadron Collider, HL-LHC (High Luminosity-LHC), the thesis work aims to implement a strategy to describe and maximise the integrated luminosity in a circular collider in the presence of luminosity levelling. The assessment of the proposed approach is performed using a Monte Carlo simulation of a year-long physics run, which generates a sequence of fills. Then, an optimisation strategy is applied to the same set of fills, and the integrated luminosity for the two configurations is compared, determining the potential gain of the proposed strategy.

Contents

Abstract i

List of Figures iv

List of Tables vii

1 Introduction to Accelerator Physics 1
- 1.1 Brief history of accelerator physics . . . 1
- 1.2 LHC and Run 3 . . . 5
- 1.3 Particle in a collider . . . 7
- 1.4 Transverse beam dynamics . . . 8
- 1.5 Longitudinal beam dynamics . . . 14
- 1.6 Non-linear beam dynamics . . . 17

2 Luminosity of a collider 20
- 2.1 Reduction factors . . . 24
  - 2.1.1 Crossing angles and crab cavities . . . 24
  - 2.1.2 Transverse offset . . . 25
  - 2.1.3 Hourglass effect . . . 26
- 2.2 Beam-beam effect . . . 26
- 2.3 Luminosity with DA model . . . 28
- 2.4 Luminosity levelling . . . 29
- 2.5 β^* levelling: model 1 . . . 34
- 2.6 Limits of the levelling model 1 . . . 35
- 2.7 β^* levelling: model 2 . . . 37
- 2.8 HL-LHC . . . 38

3 LHC Run 3 analysis 41
- 3.1 Run 3 Data analysis . . . 41

4 Optimisation strategy 51
- 4.1 The simplest case . . . 51
- 4.2 Two-parameter model . . . 54
- 4.3 Four-parameter model . . . 58
- 4.4 Failure probability . . . 60

5 Monte Carlo evaluation **64**
5.1 Monte Carlo simulation without failure 65
5.2 Monte Carlo simulation with failure 70

6 Conclusions and outlook **76**

7 Acknowledgements **77**

Appendix **78**

References **81**

List of Figures

1 M. S. Livingston and E. Lawrence beside the $27\,\mathrm{inch}$ cyclotron, built in 1934, Donald Cooksey [3]. 1
2 The machine room of the synchro-cyclotron [6]. 3
3 AdA on its support [2]. 4
4 The LHC ring [16]. 5
5 The LHC structure, with octants subdivision and their purposes [18] . . 6
6 The acceleration complex of CERN, upgraded for Run 3 operations [19]. 7
7 The co-rotating coordinate system of a particle in an accelerator ring, *x* and *y* represent the transverse horizontal and vertical coordinates [20]. 8
8 Most common magnets and the magnetic field generated [21]. 9
9 Synchronous (ϕ_1) and out-of-phase particles (ϕ_2 and ϕ_3). 16
10 The figure shows the plot of the beam-beam force as a function of the ratio r/σ: linear and non-linear regions are highlighted 19
11 First page of the personal notebook of Bruno Touschek [2]. 20
12 Visual representations of luminous regions for different levelling approaches 31
13 The HL-LHC designed upgrades [40] 39
14 On the left, forecast for peak luminosity (red dots) and integrated luminosity (violetline) of the HL-LHC era with nominal HL-LHC parameters; on the right, peak luminosity (red dots) and integrated luminosity (violetline) as an overview of the LHC operations and HL-LHC nominal and ultimate trends [42]. 40
15 From left to right, examples of fills of 2022, 2023, 2024 43
16 the decay part of the luminosity has been fitted using the DA model. Luminosity data were normalised over the maximum value ($L_\ell = L_0$) and time was expressed in units of turns 44
17 On the left, the histogram of the L_ℓ values, on the right L_ℓ as a function of the fill number 44
18 On the left, the histogram of t_{dec} values, on the right t_{dec} as a function of fill number 45
19 On the left, the distribution of the N_i parameter, on the right N_i as a function of fill number 45
20 Two symbols describe, for each fill, the values of the β^* at the start of the fill (blue dot) and at the end (orange square) 46
21 The value of the chi-squared as a function of the k value 46
22 on the left, the distribution of the ε parameter, on the right, ε as a function of fill number 47

23 on the left, the distribution of the ρ parameter, on the right, ρ as a function of fill number . . . 47
24 t_{ta} distribution for 2024 . . . 48
25 Distribution of MTBF . . . 48
26 Plots of correlations for year 2024 . . . 50
27 On the left, solutions of Eq. (4.5); on the right, solutions of Eq. (4.5) summed with the t_ℓ calculated for each $L_\ell/\hat{L}$ . . . 53
28 On the right, the behaviour of the optimised $\mathcal{L}_{\mathrm{tot}}$ with respect to the ratio $L_\ell/\hat{L}$, with the maximum values circled in red; on the left, the derivative of the $\mathcal{L}_{\mathrm{tot}}$ . . . 53
29 On the left, the behaviour of the ratio of $L(t_{\mathrm{fill}})/L_\ell$ with respect to the ratio $L_\ell/\hat{L}$; on the right, the behaviour of $L(t_{\mathrm{fill}})/\hat{L}$ with respect to the ratio $L_\ell/\hat{L}$ . . . 53
30 In the plot, the optimal $\hat{t}_{\mathrm{dec,f}}$ has been plot as a function of the α parameter for different values of the ratio $L_\ell/\hat{L}$; simulation run using $\varepsilon = 3.66 \times 10^{-24}$ . . . 57
31 In the plot, the optimal $\hat{t}_{\mathrm{dec,f}}$ has been plot as a function of the ratio $L_\ell/\hat{L}$ for different values of the t_{ta}; simulation run using $\varepsilon = 3.66 \times 10^{-24}$ 57
32 In the plot, the optimal $\hat{t}_{\mathrm{dec,f}}$ has been plot as a function of the ratio $L_\ell/\hat{L}$ for different values of the α; simulation run using $\varepsilon = 3.66 \times 10^{-24}$ 58
33 The behaviour of each optimisation parameter has been plotted with respect to the α value for different $\langle t_{\mathrm{ta}} \rangle$ values; simulation run using $\varepsilon = 3.66 \times 10^{-24}$ . . . 60
34 Distributions of t_{dec}, t_ℓ, t_{tot}, N_{fill}, L_ℓ, $\hat{L}$, $L_{\mathrm{end}}/\hat{L}$ and $\mathcal{L}_{\mathrm{tot}}$ . . . 66
35 on the left, the violin plots of each $L^*_\ell/\hat{L}$ case of the *Opt*, with a comparison with the *MC* case for $L^*_\ell/\hat{L} = 2 \times 10^4\ \mathrm{\mu b^{-1}Hz}$; on the right, the violin plots of the improvement of the Opt compared to MC for each $L^*_\ell/\hat{L}$ case. . . . 67
36 The distributions of the t_ℓ for different values of L^*_ℓ . . . 68
37 The distributions of the t_{dec} for different values of L^*_ℓ . . . 68
38 The distributions of the t_{tot} for different values of L^*_ℓ . . . 68
39 $L_{\mathrm{end}}/\hat{L}$ distributions for each L^*_ℓ case . . . 69
40 The distributions of the number of fills N_{fill} for each L^*_ℓ case . . . 69
41 Time for physics distributions for each case studied; the dashed line represents the nominal time for physics for the LHC Run 3 . . . 70
42 Distributions of t_{dec}, t_ℓ, t_{tot}, N_{fill}, t_{fail},N_{fail}, L_ℓ, $\hat{L}$, $L_{\mathrm{end}}/\hat{L}$, $\mathcal{L}_{\mathrm{tot}}$ . . . 71
43 In the plot, the distribution of $\mathcal{L}_{\mathrm{tot}}$ for each L^*_ℓ analysed . . . 72
44 Distribution of the t_ℓ parameter for different L^*_ℓ . . . 73
45 Distribution of the t_{dec} parameter for different L^*_ℓ . . . 73
46 Distribution of the t_{tot} parameter for different L^*_ℓ . . . 73

47 N_{fill} distributions for different value of the L_ℓ^* 74
48 N_{fail} distributions for different value of the L_ℓ^* 74
49 $L_{\mathrm{end}}/\hat{L}$ distributions for different value of the L_ℓ^* 74
50 Total time for physics distributions for each case studied; the dashed line represents the nominal time for physics for the LHC Run 3 75
51 On the left, the distribution of the t_ℓ data, on the right, the scattered plot 78
52 On the left, the distribution of the $N(t_\ell)$ data, on the right, the scattered plot 78

List of Tables

1 Statistical analysis of each parameter for year 2024 49
2 Statistical analysis of each parameter for years 2022, 2023 and 2024 . . 79
3 DA model parameters for Run 3 80

1 Introduction to Accelerator Physics

To state the relevant role of particle accelerators, it is useful to highlight how elementary particles' understanding increased concurrently with the evolution of high energy particle accelerators and adequate detectors, particularly from the late '60s of the last century.

1.1 Brief history of accelerator physics

During the first few years of the XX century, Ernst Rutherford used natural decay of radioactive sources to conduct experiments with alpha particles on hydrogen targets. The concept of using accelerated particles between two high-voltage ends was taken into account but was not chosen because the energy of the naturally emitted particles in the decay would have easily exceeded that of the accelerated particles.

The first evidence of the birth of accelerator physics emerged only in the second and third decade of the past century, thanks to Cockroft and Walton and the invention of the voltage multiplication electrostatic accelerator to artificially accelerate alpha particles, and in the same years the Van der Graaff electrostatic generator [1]. Another way to accelerate particles was found to be the use of a time-varying magnetic field, as if there was a current in the secondary circuit of a transformer. In this case, two were the possibilities: the circular accelerator, conceived by the electrical engineer Rolf Wideröe in 1923-25, and the linear accelerator, also developed by Wideröe starting from an idea by the Swede Gustav Ising in 1924 [2].

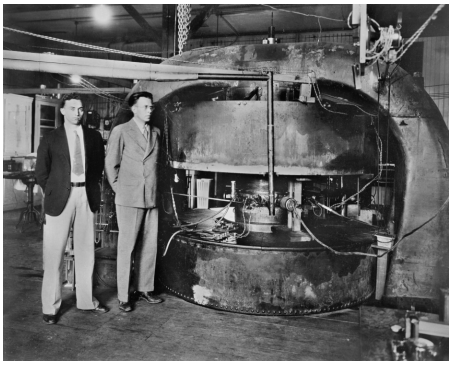

Figure 1: M. S. Livingston and E. Lawrence beside the $27\,\mathrm{inch}$ cyclotron, built in 1934, Donald Cooksey [3].

Higher energies than approximately $10\,\mathrm{MeV}$ are not obtainable through electrostatic means. The **cyclotron** (see Fig. 1), invented by Ernest Lawrence in 1930, was the first accelerator to overcome this limit[2, 4]. It used a magnetic field to make particles

curved; it was based on the well-known principle that the period of the orbit of non-relativistic charged particles, when forced to follow a circular path in the presence of a uniform magnetic field, is independent of energy. If an oscillating electromagnetic field, synchronous with the revolution frequency, is applied in a small region of space (a gap or interval) within the field, the particles gain energy every time they cross the interval and move in a spiral path, exiting the magnet. This happens because the magnetic field in cyclotrons remains constant. In the following years, larger and larger cyclotrons were built and used from the beginning for medical purposes, providing radioactive isotopes for hospitals and biological tracers for clinical investigations. Even today, these machines are used all over the world, mainly for applications in medical, industrial, and nuclear physics [2].

However, when particles become relativistic, their orbital frequency decreases, which also limits the maximum energy that can be reached. A new breakthrough was made during the war when D. W. Kerst and R. Serber built the **betatron** [5], an electron accelerator whose principle had already been outlined by Wideröe. Its topology was similar to that of the cyclotron, but the particle beam was kept in a circular orbit of constant radius instead of moving along a spiral. The cyclotron principle failed for electrons, whose motion becomes relativistic even at moderate energies. By the mid-1940s, betatrons were a significant competitor to cyclotrons, surpassing them in energy and becoming increasingly larger. Nevertheless, even the largest cyclotrons and betatrons were still inadequate for research in the field of particle physics. The maximum energy of a betatron is sharply limited by synchrotron radiation, emitted by the accelerated electrons in their circular orbit. At that time, cosmic rays were still the privileged source of high-energy events and continued to play a fundamental role until the early 1950s, revealing the existence of a large number of new particles and testing the interpretive abilities of theoretical physicists for years.

The discovery of the *synchrotron principle* by Australian physicist M. Oliphant in 1943 opened the way for a new series of circular accelerators. The use of a magnetic ring with a variable field could force particles to move along an orbit of constant curvature radius, as their energy increased during successive accelerations, imparted by an alternating electric field applied between coaxial hollow electrodes [2]. The first attempts to overcome the relativistic barrier of cyclotrons immediately followed the discovery of phase stability. The **synchrocyclotrons**, which went into operation between the late 1940s and early 1950s in the United States, Europe (see fig 2), and Russia, allowed for a significant leap forward in fundamental research. At that time, particle accelerators were beginning to take over investigations on cosmic rays, conducted with different techniques [6].

The first synchrotrons were machines for electrons, but towards the end of the 1940s, large proton synchrotrons were being planned in the United States, such as the Bevatron ($5\,\mathrm{GeV}$ - $6\,\mathrm{GeV}$) at Berkeley and the Cosmotron ($2.5\,\mathrm{GeV}$ - $3\,\mathrm{GeV}$) at

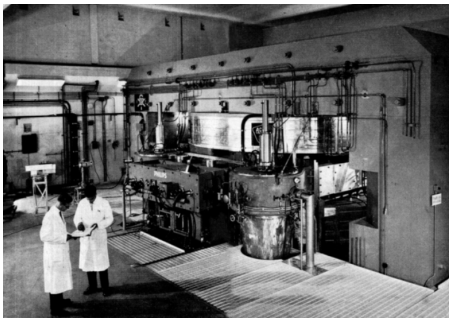

Figure 2: The machine room of the synchro-cyclotron [6].

Brookhaven, placing Americans at the forefront of high-energy physics.

The principle of *strong focusing*, independently discovered by N. Christofilos and by the group of E. D. Courant, M. S. Livingston, and H. S. Snyder in 1952, represented a new method for focusing the particles' beam through an alternating sequence of converging and diverging magnetic lenses. This greatly extended the range of energies obtainable without significant economic expenditure. The principle was immediately applied to the large $10\,\mathrm{GeV}$ **Proton Synchrotron** (PS) under construction at the newly founded CERN in Geneva, resulting in a $25\,\mathrm{GeV}$ machine for the same cost [7].

Italian research was also making a great contribution. In 1959, for example, E. Segré received the Nobel Prize in Physics for the discovery of the antiproton, made possible by the $6.5\,\mathrm{GeV}$ accelerator called the *Bevatron* in Berkeley, California. In that same year, the first Italian high-energy accelerator dedicated to fundamental research, a $1.1\,\mathrm{GeV}$ electrosynchrotron, began operation at the *INFN*'s Frascati National Laboratories. One of the main contributions from the Frascati laboratories was the construction in 1961 of a revolutionary machine. On the initiative of physicist B. Touschek, who had presented the project the year before, a vacuum chamber was built to collide beams of particles and antiparticles circulating in opposite directions, thus summing the energy of both. It was the world's first collider. It was called **AdA** (*Anello di Accumulazione*, see Fig. 3) and was a small accelerator just under two metres in diameter capable of accelerating beams to an energy of $250\,\mathrm{MeV}$. Inside it, the first artificial collisions of electrons and positrons in history took place [2, 8].

In the following years in Frascati, *ADONE* followed, with a vacuum chamber about 105 metres long and an energy of $3\,\mathrm{GeV}$. and then *DAΦNE*,with an energy of about $1\,\mathrm{GeV}$. *DAΦNE* was particularly high-performing in terms of luminosity and specialises in the production of kaons.

In the years following the introduction of *AdA* at Frascati, accelerator physics entered a new phase, characterised by international competition and the development of increasingly powerful machines. While rings like *ADONE* and *DAΦNE* were being built in Italy, globally the focus shifted to colliders, which made it possible to achieve ener-

Figure 3: AdA on its support [2].

gies much higher than those of fixed-target accelerators. CERN in Geneva led the way in 1971 with the *Intersecting Storage Rings* (ISR), the world's first proton-proton collider. During the same period, major research centres emerged in the United States. At *SLAC* (Stanford Linear Accelerator Center), the electron-positron collider *SPEAR* led to the discovery of the charm quark and the J/Ψ particle, a result that earned a Nobel Prize in 1976. Meanwhile, *Fermilab*, near Chicago, became a key player with its *Tevatron*, a $6.3\,\mathrm{km}$ synchrotron that for years held the energy record by accelerating protons and antiprotons to approximately $1\,\mathrm{TeV}$. Its greatest success was the discovery of the top quark in 1995, the last of the six quarks predicted by the Standard Model [2]. Germany's *DESY* (*Deutsches Elektronen-SYnchrotron*) in Hamburg also made significant contributions. Operational since 1965, it became famous for its storage rings, such as **HERA**, where electrons and protons were collided, allowing for in-depth studies of the proton's structure [9]. The end of the 20th century was marked by CERN's *Large Electron-Positron Collider* (**LEP**), active from 1989 to 2000 and dedicated to high-precision measurements, confirming the properties of the Standard Model and establishing that there are only three families of neutrinos [10]. These detailed investigations prepared the ground for the machine that would dominate the 21st century: the *Large Hadron Collider* (**LHC**). The *LHC*, which came into operation in 2008 in the same circular tunnel as the *LEP*, is not only the largest and most powerful accelerator in the world, but also the heir to a global scientific tradition. Its most famous achievement was the discovery of the Higgs boson in 2012, which completed the framework of the

Standard Model. Although the *LHC* holds the energy record, other projects focus on another fundamental quantity: luminosity. A prime example comes from Japan, where the *KEK laboratory* built **KEKB**, a "B-factory" that, starting in 1998, became a pioneer in the study of CP violation in B mesons, a phenomenon that explains why the universe is made of matter and not antimatter. The research conducted with *KEKB* led to the Nobel Prize in Physics in 2008 [11, 12]. The legacy of this machine continues with **SuperKEKB**, its upgrade, which is designed to achieve a luminosity about 40 times higher $8 \times 10^{35}\,\mathrm{cm}^{-2}\,\mathrm{Hz}$ [13].

1.2 LHC and Run 3

The main focus of this work will be on the LHC Run 3 (2022-2025/6). If Run 2 (2016-2018) represented the exploit of the nominal construction of LHC, during LS2 (Long Shut Down 2, 2019-2021) and thanks to the LHC Injectors Upgrade (LIU) programme [14], two main changes have been applied, making Run 3 the game changer run and preparing LHC for its HL-LHC upgrade. In particular, the centre of mass energy has increased by 4.5%, from $13\,\mathrm{TeV}$ to $13.6\,\mathrm{TeV}$, giving scientists a boost in their search for new physics and rare phenomena. The second main change is a 50% increase in the collision rate combined with luminosity levelling, a process in which the crossing angles and size of the beam are continually adjusted to maintain a steady stream of collisions for around 10 to 15 hours [15].

Figure 4: The LHC ring [16].

The LHC represents the latest addition to CERN's accelerator complex, being installed in the LEP tunnel, $100\,\mathrm{m}$ underground the French-Swiss border, and operating since 10 September 2008. The LHC consists of a 27-kilometre ring of superconducting magnets with a number of accelerating structures to boost the energy of the particles along the way (see Fig. 4). The collider works mainly with proton beams, but ions, primarily lead (Pb), are also used in the latest part of the annual collision run. The LHC

geometry basically adapts to the LEP tunnel in which it has been placed (see Fig. 5). It is made of eight straight sections and arcs. Each straight section is $529\,\mathrm{m}$ long and can carry out different tasks, experimental or utility insertion. The ATLAS and CMS high-luminosity experiments (reaching a peak luminosity of about $1 \times 10^{34}\,\mathrm{cm}^{-2}\,\mathrm{Hz}$) are located at interaction points 1 and 5, in two diametrically opposite experimental insertions. The remaining two main experiments, Alice and LHCb, are located, respectively, at IP 2 and IP8, containing also the injection system for Beam 1 and Beam 2, respectively. The remaining four straight sections do not house beam crossing points, but collimation systems (IP3 and IP7), RF systems (IP4) and beam dump insertions (IP6). The LHC arcs, instead, each contain 23 regular arc cells, $106.9\,\mathrm{m}$ long, made of two $53.45\,\mathrm{m}$ long half cells, each of which contains a quadrupole magnet and three dipoles. Additional magnetic systems, comprising trim quadrupoles and lattice skew quadrupoles, normal and skew sextupoles, lattice octupoles, spool piece sextupoles, and spool piece octupoles and decapoles complete the LHC lattice scheme [17].

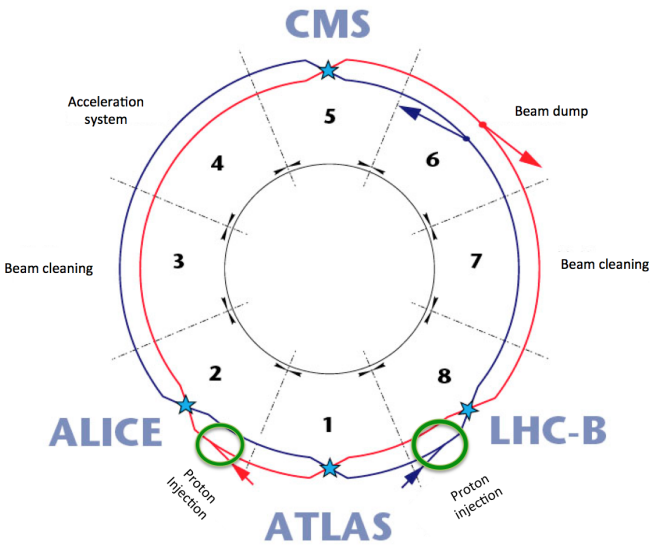

Figure 5: The LHC structure, with octants subdivision and their purposes [18]

LHC was designed to reach a centre-of-mass Energy of $14\,\mathrm{TeV}$ and a luminosity of $1 \times 10^{34}\,\mathrm{cm}^{-2}\,\mathrm{Hz}$.

To operate the LHC, particles travel through a chain of accelerators before being injected into the LHC (see Fig. 6). As happened in Run 2 operations, the proton source was obtained by subjecting hydrogen to a very intense electrical field, ionising the gas. The free protons are injected into a new H^- Linear Accelerator (Linac4), replacing Linac2, which injected protons into the Proton Synchrotron Booster (PSB), until 2018. In the

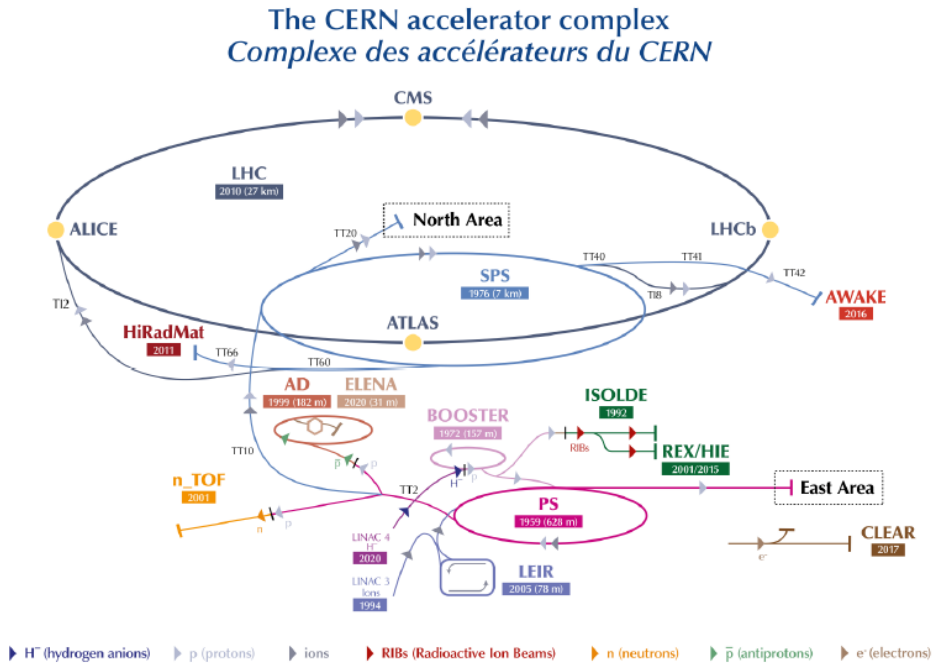

Figure 6: The acceleration complex of CERN, upgraded for Run 3 operations [19].

PSB, a new injection region had to be installed to allow the H^- charge-exchange injection at $160\,\mathrm{MeV}$ instead of the $50\,\mathrm{MeV}$ multi-turn proton injection from Linac2. The total beam energy at PSB extraction could be increased from $1.4\,\mathrm{GeV}$ to $2\,\mathrm{GeV}$ for the beams sent to the PS. The protons injected at $2\,\mathrm{GeV}$ into the PS allowed brighter beams for the same space-charge tune shift. This required an upgrade of the injection region in the PS. The PS accelerates the beams to total energies ranging from $14\,\mathrm{GeV}$ to $26\,\mathrm{GeV}$, the energy of the beams for the LHC, and determines the structure of the bunch train of the beams to be compatible with the LHC RF system. The largest machine in the injector complex is the Super Proton Synchrotron (SPS), which accelerates the beams coming from PS up to $450\,\mathrm{GeV}$. The SPS main RF system ($200\,\mathrm{MHz}$) underwent a massive upgrade in power and controls. The beam sent to LHC preserves the same time structure as before (4 trains of 72 bunches with $25\,\mathrm{ns}$ between bunches and $200\,\mathrm{ns}$ between trains), but will have double intensity and brightness [19]. At the end of the accelerating stages, the LHC ring accelerates each beam to about $7\,\mathrm{TeV}$.

1.3 Particle in a collider

To describe particles travelling in an accelerator, a co-moving coordinate system may be introduced and defined with respect to the nominal design orbit, which describes

the closed trajectory of an ideal particle in the machine (see Fig. 7). The transverse axes are denoted by the symbols *x* and *y* and describe the radial (horizontal) plane and the perpendicular (vertical) plane, respectively. The global coordinate *s* defines the zero position of the co-moving coordinate system along the design orbit with respect to an arbitrary location in the global reference frame.

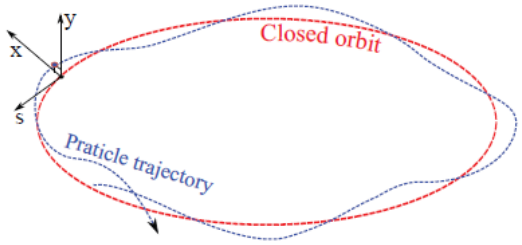

Figure 7: The co-rotating coordinate system of a particle in an accelerator ring, *x* and *y* represent the transverse horizontal and vertical coordinates [20].

Generally speaking, the key concept of physics used to manipulate and guide particles in a particle accelerator is the *Lorentz force*

$$\vec{F} = q(\vec{E} + \vec{v} \times \vec{B})\,. \tag{1.1}$$

As may be evident, the electric field $\vec{E}$ accelerates the particles in the longitudinal direction, whereas the magnetic field $\vec{B}$ is generally used to bend and focus the particles around the transverse plane. For nominal values of $v \approx c$ and $\vec{B} = 1\,\mathrm{T}$, the value of the acting force is about $3 \times 10^8\,\mathrm{N/q}$. In high-energy accelerators ($v \approx c$), bending magnets are used to steer the particle beam along the desired trajectory, whereas in low energy accelerators ($v \ll c$) electric bending and focusing are also possible.

1.4 Transverse beam dynamics

Consider a particle moving in a fixed Cartesian reference system (x, y, s) at speed $v = (\dot{x}, \dot{y}, \dot{s})$ in the presence of a magnetic field $\vec{B} = (0, B, 0)$. Its position along the trajectory is defined by the derivatives with respect to the trajectory-coordinate s, leading to

$$y'' = \frac{q}{m}\frac{1}{\dot{s}}(x' B_s - (1 + y'^2)B_x + y' x' B_y) \tag{1.2}$$

$$x'' = -\frac{q}{m}\frac{1}{\dot{s}}(y' B_s - (1 + x'^2)B_y + y' x' B_x)\,, \tag{1.3}$$

that in the specific case of $\vec{B} = (0, B, 0)$ corresponds to

$$y'' = \frac{q}{m}\frac{1}{\dot{s}}(y'x'B_y) \tag{1.4}$$

$$x'' = \frac{q}{m}\frac{1}{\dot{s}}(1 + x'^2)B_y\,. \tag{1.5}$$

So, in the horizontal plane

$$\frac{x''}{(1+x'^2)^{\frac{3}{2}}} = \frac{q}{mv}B_y = \frac{q}{p}B_y = \frac{1}{\rho}\,, \tag{1.6}$$

where ρ is the radius of the circular trajectory and p is the momentum of the particle. The quantity $\frac{p}{q} = B_y\rho$ is defined as *beam rigidity*. Increasing the momentum of the particle, the magnetic field must be increased to keep the beam on the same radius. This means that technological limitation on the intensity of the beam, reducing the maximal value desired, leads to the necessity of larger circumference accelerators ring and staged accelerators chain. Generally, the behaviour of the trajectory of a charged particle in an accelerator can be controlled using different types of magnets:

- a dipole generates a constant magnetic field across the poles ($B_y = B_0$) and is used mainly for beam deflection.
- a quadrupole generates a linear magnetic field across the poles ($B_x = gy$ and $B_y = -gx$), with g the quadrupole gradient, and is used mainly for beam focusing.

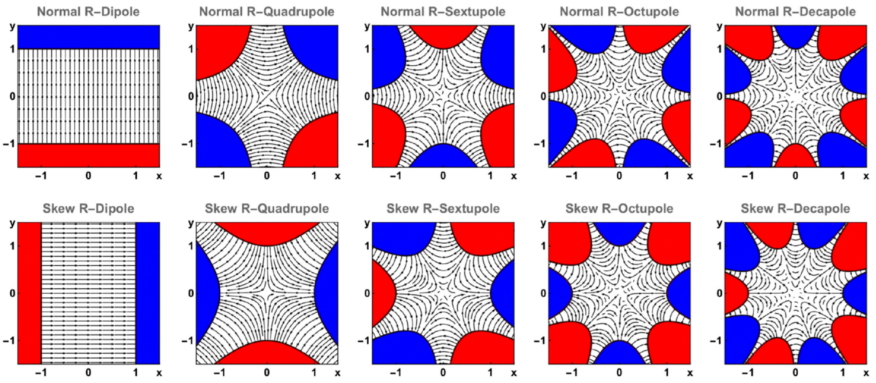

Figure 8: Most common magnets and the magnetic field generated [21].

In general, the magnetic field can be expanded around the nominal closed orbit using a multipolar expansion

$$B_y + iB_x = \frac{p}{e}\sum_n (ia_n + b_n)(x+iy)^{n-1}\,, \tag{1.7}$$

where the coefficient a_n represents the skew magnetic component and b_n the normal magnetic component. The magnetic field around the beam is then described by the superposition of multipoles (see Fig. 8), each with a specific effect on the particle's dynamic: b_0 represents the dipolar field bending the beam and b_1 the quadrupolar field focusing the beam. Not considering higher-order contributions, the beam dynamic turns out to be linear. So, for a particle feeling the effects of dipole and quadrupole

$$\begin{cases} B_y = -B_0 - gx \\ B_x = +gy \\ B_s = 0\,. \end{cases} \tag{1.8}$$

This implies that

$$x'' + \frac{\ddot{s}}{\dot{s}^2}x' - \frac{1}{\rho}\left(1+\frac{x}{\rho}\right) = \frac{q}{p}\frac{v}{\dot{s}}\left(1+\frac{x}{\rho}\right)(-B_0 - gx)\,. \tag{1.9}$$

Taking into account some assumptions, in particular that particles move with constant speed ($\ddot{s} \approx 0$) and the angle of their trajectories is small with respect to the trajectories themselves ($\frac{v}{\dot{s}} \approx 1 + \frac{x}{\rho}$, paraxial approximation), it is possible to consider that

$$p \approx p_0 + \delta p \tag{1.10}$$

$$\frac{1}{p} \approx \frac{1}{p_0} - \frac{\delta p}{p_0} = \frac{1}{p_0}\left(1 - \frac{\delta p}{p_0}\right)\,. \tag{1.11}$$

Under these hypotheses, the previous equation of motion may be rewritten as

$$x'' - \frac{1}{\rho}\left(1+\frac{x}{\rho}\right) = \frac{q}{p_0}\left(1-\frac{\delta p}{p_0}\right)\left(1+\frac{x}{\rho}\right)^2(-B_0 - gx) \tag{1.12}$$

and further

$$x'' - \frac{1}{\rho} + \frac{x}{\rho^2} = \left(1-\frac{\delta p}{p_0}\right)\left(1+\frac{x}{\rho}\right)^2\left(-\frac{1}{\rho} - k_1 x\right) = \frac{1}{\rho}\frac{dp}{p_0} - k_1 x - \frac{1}{\rho}\,. \tag{1.13}$$

So, in the horizontal plane, the equation of motion is as follows

$$x'' + \left(k_1 + \frac{1}{\rho^2}\right)x = x'' + k_x x = \frac{1}{\rho}\frac{dp}{p_0}\,, \tag{1.14}$$

where $k_x = k_1 + \frac{1}{\rho^2}$. Analysing the vertical plane under the same hypotheses, the equation of motion turns out to be

$$y'' = \frac{q}{p_0}\left(1 - \frac{\delta p}{p_0}\right)\left(1 + \frac{x}{\rho}\right)^2 gy = \frac{qgy}{p_0} = k_1 y \tag{1.15}$$

so that

$$y'' - k_y y = 0\,. \tag{1.16}$$

Hence, the motion of a particle is described by Eq.(1.14) and Eq.(1.16), known as *Hill's equations*. The Hill's equations have a solution and it is possible to analyse two different cases: the homogeneous case and the inhomogeneous one, with the introduction of a dispersion term. In the homogeneous case

$$x''(s) + k(s)x(s) = 0 \tag{1.17}$$

the general solution is a combination of sine-like and cosine-like functions, $S(s)$ and $C(s)$, also known as *principal trajectories*

$$x(s) = C(s)x_0 + S(s)x_0' \tag{1.18}$$
$$x'(s) = C'(s)x_0 + S'(s)x_0'\,, \tag{1.19}$$

so that the *transfer matrix* M is defined as

$$\begin{bmatrix} x \\ x' \end{bmatrix} = \begin{bmatrix} C(s) & S(s) \\ C'(s) & S'(s) \end{bmatrix} \begin{bmatrix} x_0 \\ x_0' \end{bmatrix}\,. \tag{1.20}$$

In the inhomogeneous case, a dispersion term must be included

$$x''(s) + k(s)x(s) = \frac{1}{\rho}\frac{dp}{p_0} \tag{1.21}$$

requiring the solution to include a particular solution of the form

$$D(s) = S(s)\int_0^s \frac{1}{\rho(\sigma)}C(\sigma)d\sigma - C(s)\int_0^s \frac{1}{\rho(\sigma)}S(\sigma)d\sigma \tag{1.22}$$

that satisfies Hill's equations and M can be expressed as

$$\begin{bmatrix} x \\ x' \\ \frac{\delta p}{p} \end{bmatrix} = \begin{bmatrix} C(s) & S(s) & D(s) \\ C'(s) & S'(s) & D'(s) \\ 0 & 0 & 1 \end{bmatrix} \begin{bmatrix} x_0 \\ x_0' \\ \frac{\delta p}{p_0} \end{bmatrix}\,. \tag{1.23}$$

With these concepts at hand, it is possible to derive the form of M for various configurations of the magnetic field. A particle simply drifting in a reference system $(x, y; s)$ without magnetic field behaves like

$$\begin{cases} x'' = 0 \\ x'(s) = x'_0 \\ x(s) = x_0 \end{cases} , \tag{1.24}$$

so

$$\begin{cases} x'(s) = x'_0 \\ x(s) = x_0 + x'_0 L \end{cases} \tag{1.25}$$

and $D(s) = D'(s) = 0$, meaning that the transfer matrix will be like

$$M_{x,y} = \begin{bmatrix} 1 & L & 0 \\ 0 & 1 & 0 \\ 0 & 1 & 1 \end{bmatrix} . \tag{1.26}$$

Instead, we analyse the behaviour of a particle passing through a focussing quadrupole of length L $\left(\frac{1}{\rho} \to 0 \text{ and } k_x > 0\right)$

$$\begin{cases} x''(s) + k_x x(s) = 0 \\ x'(s=0) = x'_0 \\ x(s=0) = x_0 \end{cases} , \tag{1.27}$$

so that

$$\begin{cases} x'(s) = -x'_0 \sin(\sqrt{k_x} L)\sqrt{k_x} + x'_0 \cos(\sqrt{k_x})L \\ x(s) = x_0 \cos(\sqrt{k_x} L) + x'_0 \frac{1}{\sqrt{k_x}} \sin(\sqrt{k_x})L \end{cases} . \tag{1.28}$$

The transfer map takes the following form:

$$\begin{bmatrix} \cos(\sqrt{k_x} L) & \frac{1}{\sqrt{k_x}} \sin(\sqrt{k_x} L) & 0 \\ -\sin(\sqrt{k_x} L) & \cos(\sqrt{k_x} L) & 0 \\ 0 & 0 & 1 \end{bmatrix} . \tag{1.29}$$

As a last example, let us consider a particle in a magnetic sector bend, allowing for a pure rotation of the particle's trajectory. In this setting, $\frac{1}{\rho} \neq 0 \text{ and } k = 0$. By defining $\phi = \frac{L}{\rho}$ the transfer map will take the following form:

$$\begin{bmatrix} \cos(\phi) & \rho \sin(\phi) & \rho(1 - \cos(\phi)) \\ -\frac{1}{\rho} \sin(\phi) & \cos(\phi) & \sin(\phi) \\ 0 & 0 & 1 \end{bmatrix} . \tag{1.30}$$

The solution of the homogeneous Hill's equation for both planes can also be found using the Floquet theorem, as a linear combination of harmonic functions:

$$u(s) = \sqrt{2J\beta(s)}\cos(\psi(s) + \psi_0)\,, \tag{1.31}$$

where J and ψ_0 are constants given by the initial conditions, $\beta(s)$ is one of the Twiss functions, known as the beta-function or amplitude function, defined by the envelope equation $2\beta\beta' - \beta'^2 + 4\beta^2 K = 4$, and $\psi(s) = \int \frac{1}{\beta(\sigma)} d\sigma$ is the betatron phase. For a particle in an accelerator ring, it is also possible to define the betatron tune, the number of betatron oscillations that a particle undergoes each turn around the ideal trajectory. The betatron tune is associated with the quadrupole arrangement and strength around the machine. It is defined as the quantity

$$Q_{x,y} = \frac{\text{number of oscillation periods}}{\text{accelerator circumference}} = \frac{1}{2\pi}\oint \frac{1}{\beta_{x,y}} ds = \frac{\nu_{x,y}}{2\pi}\,. \tag{1.32}$$

The position of the tunes in a diagram with horizontal versus vertical tunes gives the working point of the machine. It is possible to rewrite the general solution of Hill's equations as a functions of $\beta(s)$, to introduce the Courant-Snyder invariant. As

$$\begin{cases} u(s) = \sqrt{2J\beta_u(s)}\cos(\psi_u(s) + \psi_{u,0}) \\ u'(s) = \sqrt{\frac{2J}{\beta_u(s)}}\sin(\psi_u(s) + \psi_{u,0})\,. \end{cases} \tag{1.33}$$

It is worth noting that by squaring the general solutions of the Hill's equations, one obtains

$$2J_u = \epsilon_u = \gamma_u(s)u^2(s) + 2\alpha_u(s)u'(s) + \beta_u(s)u'^2(s)\,, \tag{1.34}$$

an invariant of motion representing the action of the initial conditions, the Courant-Snyder invariant or emittance ϵ, being J the action. Equation (1.34) represents an ellipse in the phase-space (u, u'), whose area is $2\pi J_u = \pi\epsilon_u$. Moreover, the phase-space coordinates of a single particle at a given location s of the machine lie on the phase space ellipse when plotted for several turns. The values of the Twiss parameters and the orientation of the phase space ellipse depend on the s location of the machine. The Twiss parameters are periodic with the machine circumference and their values are derived from the transfer matrix and are uniquely defined at any point in the machine. Generally, in phase space the particle distributions are Gaussian and this can be described using a covariance matrix Σ called the *beam matrix* and defined as

$$\begin{bmatrix} \sigma_u^2 & \sigma_{uu'} \\ \sigma_{u'u} & \sigma_{u'}^2 \end{bmatrix}\,. \tag{1.35}$$

It is interesting to note that the square root of the determinant of the covariance matrix is proportional to the area of the distribution in the phase space. In fact, defining $\Sigma_u =$

$\epsilon_u \Omega_u$, where Ω_u is the Twiss matrix $\Omega_u = \begin{bmatrix} \beta_u & -\alpha_u \\ -\alpha_u & \gamma_u \end{bmatrix}$, it turns out that $\det(\Omega_u) = 1$ and so $\det(\epsilon_u \Omega_u) = \epsilon_u^2$ and so $\epsilon_u = \sqrt{\det(\Sigma_u)}$. The geometric emittance is a constant of motion only if the beam energy is preserved in the case of $p = constant$ or in the absence of dissipative forces. Otherwise, if $P_z \to P_z + \Delta P_z$, then $x' = \frac{P_x}{P_z} \to x' = \frac{P_x}{P_z + \Delta P_z}$ and the area of the phase space shrinks. It is also possible to define a normalised emittance as $\epsilon_{\mathrm{n}} = \beta_{\mathrm{ref}} \gamma_{\mathrm{ref}} \epsilon_{\mathrm{geom}}$, which turns out to be a constant of motion even in the accelerated case. The beam size and beam divergence are, respectively, $\sigma_x = \sqrt{\epsilon_{\mathrm{geom}} \beta_x}$ and $\sigma_{x'} = \sqrt{\frac{\epsilon_{\mathrm{geom}}}{\beta_x}}$

1.5 Longitudinal beam dynamics

Generally, in the presence of a constant electric field $\vec{E}$ such that

$$\frac{d\vec{p}}{dt} = -e\vec{E}\,, \tag{1.36}$$

the direction of the force is always parallel to the field, and the trajectory and velocity of the particle can be modified, so that both the energy and the momentum can be modified. This force is suitable for being used to accelerate and decelerate particles. In the case of constant $\vec{B}$ field, so that

$$\frac{d\vec{p}}{dt} = -e(\vec{v} \times \vec{B})\,, \tag{1.37}$$

the direction is always perpendicular to the velocity, and only the direction can be modified, so that the energy of the particle stays constant. Taking into account a time varying $\vec{E}$ defined as

$$E(s, r, t) = E_1(s, r) E_2(t)\,, \tag{1.38}$$

where the time component turns out to be a sinusoidal time dependent function $E_2(t) = E_0 \sin \Phi(t)$ with $\Phi(t) = \int_{t_0}^{t} \omega_{\mathrm{RF}} dt + \Phi_0$, it is possible to describe the behaviour of a particle crossing an acceleration cavity known as *RF (Radio Frequency) Cavity*. Let V_{RF} be the amplitude of the RF voltage across the gap g, so that the particle crosses the gap at a distance r. The energy gain is

$$\Delta E = e \int_{-g/2}^{g/2} E(s, r, t) ds\,. \tag{1.39}$$

In a circular accelerator, the origin of time is taken at the zero crossing of the RF voltage with positive slope, whereas, in a linear accelerator, the origin of time is taken at the positive maximum of the RF voltage. Accounting for a more simple model, defined as

$$\begin{cases} E_1(s, r) = \frac{V_{\mathrm{RF}}}{g} = \text{constant} \\ E_2(t) = \sin(\omega_{\mathrm{RF}} t + \Phi_0) \end{cases} \tag{1.40}$$

and for $t = 0$, $s = 0$, and $v \neq 0$ parallel to the electric field, the energy variation is equal to

$$\Delta E = eV_{\mathrm{RF}} T_{\mathrm{a}} \sin \Phi_0 \tag{1.41}$$

and the transit time factor, related to the time required to fill the cavity with the electric field, equals to

$$T_{\mathrm{a}} = \frac{\sin \frac{\omega_{\mathrm{RF}} g}{2V}}{\frac{\omega_{\mathrm{RF}} g}{2V}} , \tag{1.42}$$

such that $T_{\mathrm{a}} \to 1 \text{ for } g \to 1$. It is clear that longitudinal motion is deeply connected with synchronisation between the particles and the accelerating system, by creating an electric field in the direction of the desired acceleration. To fulfil these requirements, the condition

$$T_{\mathrm{rev}} = hT_{\mathrm{RF}} \implies f_{\mathrm{rev}} = hf_{\mathrm{RF}} \tag{1.43}$$

must be fulfilled, where h is defined as the harmonic number, indicating the maximum number of beam bunches it is possible to load into the accelerator. In a generic particle transport system, a nominal trajectory is defined for the nominal momentum p. For a particle with a momentum distribution $p + \Delta p$, the trajectory length may differ from the nominal one, L.

The momentum compaction factor is defined as

$$\alpha_{\mathrm{c}} = \frac{dL/L}{dp/p} , \tag{1.44}$$

and it can be proven that

$$\alpha_{\mathrm{c}} = \frac{1}{L} \int_0^L \frac{D_x(s)}{r(s)} ds , \tag{1.45}$$

where $D_x(s)$ represents the dispersion term, r the radius of the trajectory of the particle. For small momentum deviation, taken at first order,

$$\frac{\Delta L}{L} = \alpha_{\mathrm{c}} \frac{\Delta p}{p} . \tag{1.46}$$

This rule simply states that, if the particle's momentum is greater than the nominal one, the trajectory results to be longer. In the specific case of a ring collider, given that the trajectory circumference is $C = 2\pi r$ and the radius r is strongly affected by the magnitude of the momentum p of the particle, increasing the latter without increasing the magnetic field strength, leads to

$$\frac{\Delta C}{C} = \alpha_{\mathrm{c}} \frac{\Delta p}{p} . \tag{1.47}$$

The momentum compaction with respect to the energy of the particle and with respect to the magnetic field strength, turns out to obey, respectively, the following laws:

$$\alpha_c = \beta^2 \frac{\frac{dR}{R}}{\frac{dE}{E}} \tag{1.48}$$

$$\alpha_c = 1 - \frac{\frac{d<B>}{<B>}}{\frac{dp}{p}} . \tag{1.49}$$

The momentum compaction value for the ion and proton machines is positive, meaning that an increase in the nominal momentum would lead to a grater radius. However, there exists an energy at which the velocity variation is compensated by the trajectory variation, called the transition energy

$$\gamma_{tr} = \sqrt{\frac{1}{\alpha_c}} . \tag{1.50}$$

Below the transition value, higher energy leads to higher revolution frequency, whereas above the transition, higher energy leads to lower revolution frequency. Taking a simple case of constant magnetic field and $\gamma < \gamma_{tr}$, a particle is defined synchronous if it is always in phase with the RF phase, as in $\omega = \omega_{RF}/h$. To maintain the resonant condition, the particle energy must be kept constant and the phase must be $\phi_1 = 0$. If the particle's phase is negative (ϕ_3 in Fig. 9), then $V_{RF} < 0$, and the particle decelerates and decreases in energy. This leads to a decrease in the revolution frequency and the phase tends to zero. However, when the phase is positive and $V_{RF} > 0$, (ϕ_2 in Fig. 9), the particle is accelerated and an increase in energy leads to an increase in revolution frequency, so that its phase again tends to zero.

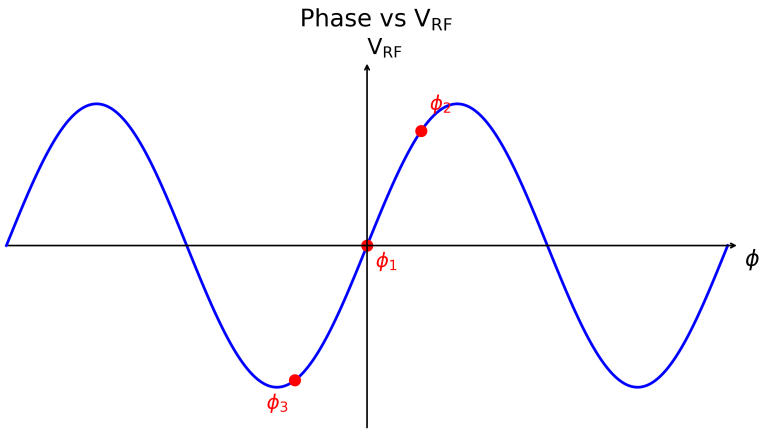

Figure 9: Synchronous (ϕ_1) and out-of-phase particles (ϕ_2 and ϕ_3).

In the phase-space portrait, the orbits of the asynchronous particles rotate around the synchronous particle.

1.6 Non-linear beam dynamics

Thus far, the particle dynamic explored was strictly related to linear behaviours, in particular the transverse dynamic was described by the *Hill's equations* Eqs. (1.14)(1.16). However, such an ideal scheme does not apply in real accelerators or colliders. As a matter of fact, non-linear phenomena should be included in the description of the particles' behaviours, being incorporated in the accelerator lattice by design purpose or due to intrinsic lattice imperfections.

Non-linearities are caused by several factors, including the presence of higher-order magnetic fields from multipole magnets (such as sextupoles and octupoles), which are fundamental for *chromatic aberration correction* or *Landau damping*, respectively. Furthermore, *beam-beam effects*, as colliding particle bunches exert electromagnetic forces on each other, and *space-charge forces* within a bunch are significant sources of non-linearity, especially for high-intensity beams. The consequences of these effects are profound, as they can excite resonances that cause particle loss and lead to a reduction in the dynamic aperture, the extent of the region in phase space where bounded motions occur [22].

The beam-beam interaction turns out to be of particular interest for the following analysis. In fact, It leads to emittance blow-up, beam losses, and reduction of the beam lifetime, generating non-linear electromagnetic potentials affecting the machine's luminosity production. Assume a bunch with a Gaussian charge distribution

$$\rho(x,y,z) = \frac{nq}{4\pi\epsilon_0} e^{-\left(\frac{x^2}{2\sigma_x^2}+\frac{y^2}{2\sigma_y^2}+\frac{z^2}{2\sigma_z^2}\right)} \tag{1.51}$$

generating an electric potential

$$\phi(x,y,z) = \frac{nq}{\sqrt{\pi}} \int_0^\infty dt \frac{e^{-\left(\frac{x^2}{2\sigma_x^2+t}+\frac{y^2}{2\sigma_y^2+t}+\frac{z^2}{2\sigma_z^2+t}\right)}}{\sqrt{(2\sigma_x^2+t)(2\sigma_y^2+t)(2\sigma_z^2+t)}} \,. \tag{1.52}$$

The transverse electric field is given by

$$\vec{E}(x,y,z) = -\nabla\phi(x,y,z) \,. \tag{1.53}$$

In the simplified assumption of infinitely long round beams, with $\sigma = \sigma_x = \sigma_y$, the radial electric field may be computed by the Gauss theorem, so that

$$2\pi r E_r = \frac{1}{\epsilon_0}\int_0^r dt \frac{nqt}{\sigma^2} e^{-\frac{t^2}{2\sigma^2}} = \frac{nq}{\epsilon_0}\left(1 - e^{-\frac{r^2}{2\sigma^2}}\right) \tag{1.54}$$

Calculating also the magnetic component in the same way, namely

$$2\pi B_\phi = \mu_0 \int_0^r dt 2\pi t \beta c \rho(t)\,, \tag{1.55}$$

the beam-beam force is

$$\vec{F} = q(\vec{E} + \vec{v} \times \vec{B}) = q(E_r + \beta c B_\phi) \times \hat{r}\,, \tag{1.56}$$

corresponding to

$$F_r = \frac{nq^2(1+\beta^2)}{4\pi\epsilon_0\sigma^2 r}\left(1 - e^{-\frac{r^2}{2\sigma^2}}\right)\,. \tag{1.57}$$

For particles near the centre of the beam, $r \ll \sigma$,

$$F_r = \frac{nq^2(1+\beta^2)}{4\pi\epsilon_0\sigma^2} r \tag{1.58}$$

the radial force is linear in the radial direction, and a linear focusing (respectively, defocusing) effect arises for positive (respectively, negative) values of the ratio r/σ, with a gradient

$$k_x = k_y = \frac{nq^2(1+\beta^2)}{4\pi\epsilon_0\sigma^2}\,. \tag{1.59}$$

In this regime, a quadrupole-like kick is generated, which induces a linear tune shift. Instead, for a particle far from the centre, $r \gg \sigma$,

$$F_r = \frac{nq^2(1+\beta^2)}{2\pi\epsilon_0 r}\,, \tag{1.60}$$

with $\frac{dF_r}{dr} = -\frac{nq^2(1+\beta^2)}{2\pi\epsilon_0 r^2}$. This means that the induced tune spread is amplitude dependent and of opposite sign with respect to the one of particles near the centre of the bunch, a highly non-linear scenario. The beam-beam force function and the two behaviours described here have been reported in Fig. 10

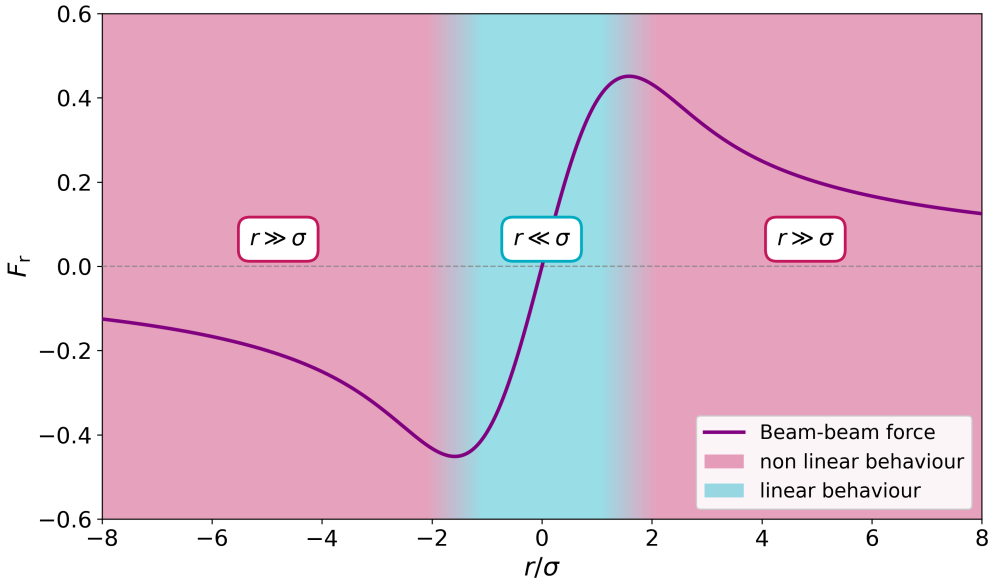

Figure 10: The figure shows the plot of the beam-beam force as a function of the ratio r/σ: linear and non-linear regions are highlighted

2 Luminosity of a collider

Luminosity represents, together with the *energy at the centre of mass*, a key concept for evaluating the performance of a particle collider. Although the concept of collision rates had been implicit in earlier fixed-target experiments, the formal definition of luminosity as a figure of merit for comparing collider performance became essential with the development of storage rings and beam-beam collision experiments in the late 1950s and early 1960s.

Among the papers of Bruno Touschek preserved in the archive of the Physics Department at *"La Sapienza" University of Rome*, a notebook labelled *"Q. L. AdA (laboratory notebook)"* with the acronym "SR", *Storage Ring*, written in red pencil, turns out to be extremely precious for our aims. It is therefore evident that this notebook, which extends at least until February 25, constitutes the first explicit testimony of Touschek's reflections and the first concrete exploration of his theoretical intuitions. On the first page, where he immediately notes *"State of affairs. Discussed plan with Ghigo"* the formula for the luminosity of the ring ("Basic formula") appears, defined as the proportionality factor between the beam intensities and the number of relevant events produced per unit of time. Touschek shows that the available parameters are plausible for obtaining the desired results at AdA [2, 23].

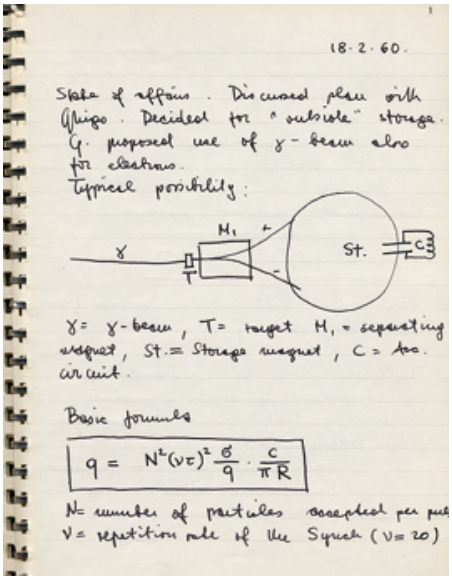

Figure 11: First page of the personal notebook of Bruno Touschek [2].

Moreover, the results reported in the paper *Measurements of the Rate of Interaction between Stored Electrons and Positrons* [23] may represent one of the first trace of the concept of luminosity. In particular, analysing the paper, a formula describing

the rate of events and comprehending what we nowadays call luminosity is reported. In particular, the authors define the target volume through the overlap integral of the particle densities:

$$\frac{N_+ N_-}{V} = \int \varrho_+(\mathbf{x})\, \varrho_-(\mathbf{x})\, d^3x\,, \tag{2.1}$$

where $\varrho_+(\mathbf{x})$ and $\varrho_-(\mathbf{x})$ represent the spatial density distributions of positrons and electrons, respectively, N_+ and N_- are the total numbers of positrons and electrons, and V is the target volume. The interaction rate is then expressed as:

$$\dot{n} = f_{\mathrm{rev}} \sigma N_+ N_- \frac{L\eta}{V}\,, \tag{2.2}$$

where f_{rev} is the revolution frequency of the particles in the beam of AdA ($f_{\mathrm{rev}} = 7.451\,07\,\mathrm{Hz}$) and σ is the cross-section of the monitoring reaction. L is the total length of the beam path monitored by the detector, and η is the total efficiency that accounts for counter arrangement and geometric factors. If L is very small compared to the r.m.s length of the bunches, no correction needs to be made for the density distribution in the bunches: in this case η is the efficiency of the counter arrangement. In fact, the term

$$\tilde{L} = f_{\mathrm{rev}} N_+ N_- \frac{L\eta}{V} \tag{2.3}$$

represents instantaneous luminosity.

The concept of luminosity has evolved significantly since these early measurements. Instead of calculating collision rates directly using formulas like Eq. 2.2, which combined beam properties, detector geometry, and cross-sections in a single expression, the modern notion of luminosity emerged as a cleaner way to separate machine characteristics from physics processes. This abstraction, where the event rate is simply expressed as $\dot{N} = \sigma \tilde{L}$, made it easier to compare different colliders and experiments independently of the specific reactions being studied, establishing luminosity as the standard figure of merit for collider performance.

Taking into account two colliding particles of mass m_1 and m_2, the total centre-of-mass energy E_{cm} is defined as

$$(\boldsymbol{p_1} + \boldsymbol{p_2})^2 = E_{\mathrm{cm}}^2 = (E_1 + E_2)^2 - (\vec{p_1} + \vec{p_2})^2\,, \tag{2.4}$$

where $\boldsymbol{p_i} = (E_i, \vec{p_i})$. For a collider experiment, $\vec{p_1} = -\vec{p_2}$, and so

$$E_{\mathrm{cm}} = E_1 + E_2\,. \tag{2.5}$$

The energy of the centre of mass is fundamental in defining the mass of the products of a collision. The luminosity, instead, determines the number of events generated in

a period of time, taking into account the probability that each happens. Generally, the luminosity can be defined as

$$L = \frac{1}{\sigma_p}\frac{dR}{dt}\left[\mathrm{cm}^{-2}\mathrm{Hz}\right] \tag{2.6}$$

where dR/dt is the rate of events, σ_p the cross section of events considered. The total number of events collected in a certain time interval would then be defined as

$$N_{\mathrm{tot}} = \sigma_p \mathcal{L}_{\mathrm{int}} = \int_{t_1}^{t_2} L(t)dt \tag{2.7}$$

where $\mathcal{L}_{\mathrm{int}}$ represents the integrated luminosity, usually measured in fb^{-1}. To increase the value of N_{tot}, due to the small cross section values ($< \mathrm{nb}$), the luminosity must be maximised.

To provide context for typical luminosity values achieved in modern colliders, it is instructive to examine the progression across different facilities and operating periods. The Large Electron-Positron Collider (LEP) at CERN achieved an instantaneous luminosity of $1.6 \times 10^{31}\,\mathrm{cm}^{-2}\mathrm{Hz}$ during its initial phase (LEP1), subsequently reaching peak values of $1.0 \times 10^{32}\,\mathrm{cm}^{-2}\mathrm{Hz}$ in the higher-energy LEP2 phase [24, 25].

The B-factory accelerators demonstrated significantly improved performance, with KEKB achieving a record instantaneous luminosity of $2.11 \times 10^{34}\,\mathrm{cm}^{-2}\mathrm{Hz}$ during its operational period from 1999 to 2010 [26], and PEP-II at SLAC reaching $1.21 \times 10^{34}\,\mathrm{cm}^{-2}\mathrm{Hz}$ [27], substantially exceeding their design specifications of $3 \times 10^{33}\,\mathrm{cm}^{-2}\mathrm{Hz}$.

The Large Hadron Collider (LHC) has achieved remarkable luminosity performance during its operational periods. During Run 2 (2015-2018), the LHC surpassed its nominal design luminosity of $1.0 \times 10^{34}\,\mathrm{cm}^{-2}\mathrm{Hz}$ by more than a factor of two, with a peak instantaneous luminosity reaching approximately $2.1 \times 10^{34}\,\mathrm{cm}^{-2}\mathrm{Hz}$ for the ATLAS and CMS experiments [28]. This exceptional performance enabled the delivery of approximately $160\,\mathrm{fb}^{-1}$ of integrated luminosity per experiment over the four-year period, providing unprecedented statistical samples for precision measurements and searches for new physics phenomena. The main focus of the thesis work would be on the LHC case and its forthcoming luminosity upgrade, the High-Luminosity LHC (HL-LHC) [17].

The luminosity can be formally derived from first principles by considering the collider's operational parameters and beam dynamics. For bunched beams that collide along the longitudinal coordinate s, with a temporal evolution characterised by $s_0 = ct$, and assuming perfect overlap at the interaction point, the luminosity is expressed as

$$L = N_1 N_2 K \int_x \int_y \int_s \int_{s_0} dxdyds ds_0 \rho_1(x, y, s, -s_0)\rho_2(x, y, s, s_0) \tag{2.8}$$

where N_1 and N_2 are the populations of the bunch, while K is the kinematic factor, a constant defined as $\sqrt{(\mathbf{v}_1 - \mathbf{v}_2)^2 - \frac{(\mathbf{v}_1 \times \mathbf{v}_2)^2}{c^2}}$ [29], related to the speed of the collid-

ing particles and the crossing angle by the vectorial product, equal to $2c$ in the case of symmetric beams; $\rho_1(x, y, s, -s_0)$ and $\rho_2(x, y, s, s_0)$ are the density distribution of the particles, normalised to 1, respectively for the counter-clockwise and clockwise rotating bunches, integrated over x and y, the transverse coordinates, s the longitudinal coordinate, and s_0 the time variable. Assuming:

- head-on collisions between bunches
- $\mathbf{v}_1 = -\mathbf{v}_2$
- uncorrelated Gaussian densities in all planes as $\rho_u = \frac{1}{\sigma_u\sqrt{2\pi}} e^{-\frac{(u-u_0)^2}{2\sigma_u^2}}$
- beams circulating in the machine ring f_{rev} times per second (storage ring)
- k_b colliding bunch pairs per beam
- σ_s the r.m.s bunch length
- σ_x^*,σ_y^*, transverse beam size at the collision point

then the definition of luminosity becomes

$$L = \frac{2 f_{\mathrm{rev}} k_{\mathrm{b}} N_1 N_2}{(\sqrt{2\pi})^6 \sigma_s^2 \sigma_x^{*2} \sigma_y^{*2}} \int_x \int_y \int_s \int_{s_0} dx dy ds ds_0 e^{-\frac{x^2}{\sigma_x^{*2}}} e^{-\frac{y^2}{\sigma_y^{*2}}} e^{-\frac{s^2}{\sigma_s^2}} e^{-\frac{s_0^2}{\sigma_s^2}} \tag{2.9}$$

and, by solving the Gaussian integrals, one obtains

$$L = \frac{N_1 N_2 f_{\mathrm{rev}} k_{\mathrm{b}}}{4\pi \sigma_x^* \sigma_y^*} \,. \tag{2.10}$$

The definition can be rewritten in a more explicit form, including the emittance function, the relativistic gamma factor, and the amplitude function at the interaction point β^* associated to the collider

$$\sigma_x^* = \sigma_y^* = \sqrt{\frac{\beta^* \epsilon}{\gamma_{\mathrm{r}}}} \,, \tag{2.11}$$

so

$$L = \frac{k_{\mathrm{b}} N_1 N_2 f_{\mathrm{rev}} \gamma_{\mathrm{r}}}{4\pi \beta^* \epsilon} \,. \tag{2.12}$$

In light of this definition, the luminosity optimisation can be performed in different ways: increasing the relativistic gamma factor, thus increasing the energy of the collider; increasing the number of bunches circulating in the collider,thus changing the harmonic number of the system; reducing β^*.

It should be noted that Eq. (2.12) represents the maximum achievable luminosity under ideal conditions. In practice, several physical effects contribute to the reduction in luminosity, including transverse beam offsets, crossing angles, the hourglass effect, non-Gaussian beam profiles, non-zero dispersion at the interaction point, and variations in the beta function ($\delta\beta^*/\delta s \neq 0$).

Crossing angles, commonly employed in high-intensity machines such as the LHC, CESR, and KEKB to prevent parasitic bunch collisions, introduce a geometric reduction in the effective volume overlap. This reduction can be partially compensated for by crab cavities, which rotate bunches to achieve head-on collisions in the centre-of-mass frame. Transverse offsets between the colliding beams—whether intentional (for luminosity control or calibration purposes) or arising from beam-beam interactions—further diminish the overlap integral and hence the luminosity.

The hourglass effect manifests itself as a longitudinal variation in the transverse beam size when the bunch length becomes comparable to the beta function at the interaction point. This violates the assumption of constant beam size throughout the collision region, necessitating a geometric correction factor to evaluate the actual value of the luminosity. Similarly, non-Gaussian beam profiles and non-zero dispersion at the interaction point increase effective beam sizes, while optical aberrations that displace the collision point from the betatron function minimum introduce additional penalties [30].

For the current analysis, we focus primarily on the effects of transverse offsets, crossing angles, and the hourglass effect, as these represent the dominant luminosity reduction mechanisms in modern collider operations.

2.1 Reduction factors

2.1.1 Crossing angles and crab cavities

As mentioned above, this effect may be desired or not. Assuming the angle of collision Φ lies in the horizontal plane, the overlap integrals between the two distributions must be computed considering the x and y coordinates, applying then a transformation of coordinates in the $x-s$ reference system. In particular, in the rotated reference system, for Beam 1 and Beam 2, respectively,

$$\begin{cases} x_1 = x\cos\Phi/2 - s\sin\Phi/2 \\ s_1 = s\cos\Phi/2 + x\sin\Phi/2 \end{cases} \qquad \begin{cases} x_2 = x\cos\Phi/2 + s\sin\Phi/2 \\ s_2 = s\cos\Phi/2 - x\sin\Phi/2 \end{cases} \tag{2.13}$$

and the overlap integral can be written as

$$
\begin{aligned}
L = {} & 2\cos^2\Phi/2 N_1 N_2 f_{\mathrm{rev}} k_{\mathrm{b}} \\
& \times \int\int\int\int dx dy ds ds_0 \rho_{1x}(x_1)\rho_{1y}(y_1)\rho_{s_1}(s_1 - s_0) \\
& \times \rho_{2x}(x_2)\rho_{2y}(y_2)\rho_{s_2}(s_2 + s_0)
\end{aligned}
\tag{2.14}
$$

where $\cos^2\Phi/2$ is the kinematic term for non-collinear bunches. Integrating over y and s_0 using

$$
\int_{-\infty}^{+\infty} du e^{-(au^2+bu+c)} = \sqrt{\frac{\pi}{a}} e^{\frac{b^2-ac}{a}} , \tag{2.15}
$$

$$
L = \frac{N_1 N_2 f_{\mathrm{rev}} k_{\mathrm{b}}}{8\pi^2 \sigma_s \sigma_x^2 \sigma_y^2} 2\cos^2\frac{\Phi}{2} \iint e^{-\frac{x^2\cos^2(\Phi/2)+s^2\sin^2(\Phi/2)}{\sigma_x^2}} e^{-\frac{x^2\sin^2(\Phi/2)+s^2\cos^2(\Phi/2)}{\sigma_s^2}} dx ds \, . \tag{2.16}
$$

As both x and $\sin\Phi/2$ are small, terms proportional to $\sigma_x^k \sin^l\Phi/2$ and $x^k \sin^l\Phi/2$ for $k+1>4$ can be neglected and approximated as $\sin\Phi/2 \approx \tan\Phi/2$ so that

$$
L = \frac{N_1 N_2 k_{\mathrm{b}} f_{\mathrm{rev}}}{4\pi\sigma_x\sigma_y} C \tag{2.17}
$$

where $C \approx \frac{1}{\sqrt{1+(\frac{\sigma_s\Phi}{\sigma_z 2})^2}}$ represents the reduction term and $\frac{\sigma_s\Phi}{\sigma_z 2}$ is the Piwinski angle [30].

2.1.2 Transverse offset

The transverse offset reduction factor is generally associated with the presence of a non-head-on bunch collision. Assuming a displacement d_1 for Beam 1 and d_2 for Beam 2 with respect to the nominal trajectories, the coordinates of the colliding bunches turn out to be

$$
\begin{cases} x_1 = d_1 + x\cos\Phi/2 - s\sin\Phi/2 \\ s_1 = s\cos\Phi/2 + x\sin\Phi/2 \end{cases}
\qquad
\begin{cases} x_2 = d_2 + x\cos\Phi/2 + s\sin\Phi/2 \\ s_2 = s\cos\Phi/2 - x\sin\Phi/2 \end{cases}
\tag{2.18}
$$

Using the same calculations performed in Eqs. (2.14) and (2.16) with the new set of coordinates, the luminosity turns out to be

$$
L = \frac{N_1 N_2 f_{\mathrm{rev}} k_{\mathrm{b}}}{4\pi^{3/2}\sigma_s} \cos\Phi/2 \int ds \frac{W}{\sigma_x\sigma_y} e^{-(As^2+2Bs)} \tag{2.19}
$$

where

$$A = \frac{\sin^2\frac{\Phi}{2}}{\sigma_x^2} + \frac{\cos^2\frac{\Phi}{2}}{\sigma_s^2}, \qquad B = \frac{(d_2 - d_1)\sin(\Phi/2)}{2\sigma_x^2}, \qquad W = e^{-\frac{1}{4\sigma_x^2}(d_2-d_1)^2}. \quad (2.20)$$

The luminosity equation, including both reduction factors analysed until now, turns out to be

$$L = \frac{N_1 N_2 f_{\mathrm{rev}} k_b}{4\pi\sigma_x\sigma_y} \cdot W \cdot e^{\frac{B^2}{A}} \cdot S\,, \quad (2.21)$$

where W accounts for the offset, S for the crossing angle, $e^{\frac{B^2}{A}}$ for the presence of both effects simultaneously [30] .

2.1.3 Hourglass effect

The model introduced up to this point assumes constant transverse beam sizes over all the collision region. However, since the β function is a function of s,

$$\beta(s) = \beta^*\left(1 + \left(\frac{s}{\beta^*}\right)^2\right) \quad (2.22)$$

with a minimum at the collision point, the assumption may be incorrect. It is also evident that the beam size increases approximately linearly with the distance to the collision point as $\sigma = \sqrt{\beta(s)\varepsilon}$. Due to the shape of the function β, the name hourglass effect is given. The effect is particularly relevant whenever $\beta^* \approx \sigma_s$. The formula for the luminosity accounting for this reduction term is

$$L = \frac{N_1 N_2 f_{\mathrm{rev}} k_{\mathrm{b}}}{4\pi\sigma_x^*\sigma_y^*}\frac{\cos\frac{\Phi}{2}}{\sqrt{\pi}\sigma_s}\int_{-\infty}^{+\infty}\frac{e^{-s^2A}}{1+\left(\frac{s}{\beta^*}\right)^2}ds \quad (2.23)$$

$$A = \frac{\sin^2\frac{\Phi}{2}}{\sigma_x^{*2}\left[1+\left(\frac{s}{\beta^*}\right)^2\right]} + \frac{\cos^2\frac{\phi}{2}}{\sigma_s^2}. \quad (2.24)$$

The integral is hardly solvable by analytical means, and numerical approaches are to be preferred.

2.2 Beam-beam effect

Taking into account what has been described in 1.6, particles that experience the linear part of the beam-beam force are subjected to a quadrupole-like kick, which can be

evaluated to find the radial deflection. Considering the two-dimensional force and the longitudinal distribution, the beam beam kick for a test particle becomes

$$\gamma\beta mc\Delta r' = \int_{-\infty}^{\infty} dt F_{\mathrm{r}}(r,s,t) \tag{2.25}$$

as

$$F_{\mathrm{r}}(r,s,t) = \frac{Nq^2(1+\beta^2)}{2\pi\epsilon_0 r\sigma_s}\left(1-e^{-\frac{r^2}{2\sigma^2}}\right)\left(e^{-\frac{(s+vt)^2}{2\sigma_s^2}}\right), \tag{2.26}$$

and, by integration,

$$\Delta r' = \frac{1}{mc\beta\gamma}\int_{-\infty}^{+\infty} dt F(r,s,t) = \frac{2nr_0}{\gamma r}\left(1-e^{-\frac{r^2}{2\sigma^2}}\right), \tag{2.27}$$

with $r_0 = \frac{e^2}{4\pi\epsilon_0 mc^2}$ the classical particle radius, n the charge line density in the lab frame. In the asymptotic limit for $r \to 0$

$$\Delta r' = \frac{nr_0}{\gamma\sigma^2} r = kr\,, \tag{2.28}$$

being k the gradient induced by the beam-beam force, equivalent to the action of a thin lens element of gradient k, causing the change of tune of a quantity

$$\Delta Q = \frac{1}{4\pi}\frac{\beta^* nr_0}{\gamma\sigma^2} = \frac{1}{4\pi}\frac{nr_0}{\gamma\varepsilon} = \xi\,. \tag{2.29}$$

The luminosity can be defined using the beam-beam parameter, as

$$L = \frac{kf_{\mathrm{rev}}n}{r_0\beta^*}\xi\gamma\,, \tag{2.30}$$

with $\xi \ll 0.5$.

Whenever the beam-beam interaction acts coherently on the entire bunch, if opposite bunches interact at a certain distance, each of them experiences a dipolar kick generated by the other bunch.

2.3 Luminosity with DA model

With the goal of generating a model describing reality in the most efficient way, the simplest ideal description of luminosity evolution, related only to collision-induced burn-off, must be modified to include non-linear beam dynamics behaviours.

A key concept that must be introduced to describe the evolution of beam losses in circular colliders, and so the luminosity lifetime, is that of dynamic aperture (DA) and its time evolution.

The DA is a metric that describes the extent of the stable phase-space region occupied by particles moving within the beam envelope, where bounded motion occurs. Non-linear effects reduce the DA, shrinking the volume available for stable motion. Since the 1990s, different models have been proposed to describe the evolution of DA as a function of the number of turns, highlighting the profound relations between DA, beam stability, and luminosity. In [31] different models have been tested and, for the purpose of this work, the so called *Model 2* is of particular relevance as an effective scaling law tied to the luminosity evolution:

$$D(N) = \rho \left(\frac{\kappa}{2e}\right)^{\kappa} \frac{1}{log^{\kappa}\frac{N}{N_0}}\,, \tag{2.31}$$

where ρ and κ are free parameters, N_0 is assumed equal to 1. The defined DA shows an inverse logarithmic decay as N increases. A luminosity evolution model has been developed in [32, 33, 34], as a function of turns including both effects from the burn-off losses and pseudo-diffusive effects from DA evolution. Assume the luminosity to be described by Eq. 2.12 and an additional term $F(\theta_{\mathrm{c}}, \sigma_s, \sigma^*)$ that accounts for the reduction in volume overlap (hour-glass effect excluded), the function of the half crossing angle $\theta_c/2$ and RMS dimensions σ_s and σ^*

$$F(\theta_c, \sigma_s, \sigma^*) = \frac{1}{\sqrt{1 + (\frac{\theta_c \sigma_s}{2\sigma^*})^2}}\,. \tag{2.32}$$

Assuming an ideal collider and excluding levelling or dynamic-beta effects, only emittances and bunch intensities may change over time, and luminosity burn-off stands out as the main mechanism driving beam losses during collisions. The evolution of the peak luminosity would then be driven by its own value and the beam intensity, derived from

$$N'(t) = -\sigma_{\mathrm{int}} n_{\mathrm{c}} L\,(t) = -\sigma_{\mathrm{int}} n_{\mathrm{c}} \Xi N^2(t)\,, \tag{2.33}$$

where $\Xi = \frac{\gamma_{\mathrm{r}} f_{\mathrm{rev}} F(\theta_c, \sigma_s, \sigma^*)}{4\pi\epsilon^* \beta^* k_b}$,admitting solution

$$N(t) = \frac{N_i}{(1 + \sigma_{\mathrm{int}} n_{\mathrm{c}} \Xi N_i t)^2}\,. \tag{2.34}$$

The luminosity decrease turns out to be well described by

$$L(t) = \frac{\Xi N_i^2}{(1 + \sigma_{\text{int}} n_{\text{c}} \Xi N_i t)^2} \,. \tag{2.35}$$

In the most general case, $N_1(t)$ and $N_2(t)$ are different. Introducing a time variable $\tau = 1 + f_{\text{rev}} t$ corresponding to the number of turn a particle completed in the ring, their behaviours with respect to the defined variable and due only to the burn-off effect can be described by

$$\begin{cases} N_1^{\text{bo}}(\tau) = N_2^{\text{bo}}(\tau) + \xi \\ \dot{N}_2^{\text{bo}}(\tau) = -\varepsilon N_2^{\text{bo}}(\tau)[N_2^{\text{bo}}(\tau) + \xi] \,, \end{cases} \tag{2.36}$$

where $\varepsilon = \sigma_{\text{int}} n_{\text{c}} \Xi / f_{\text{rev}}$. Under the assumption of equal intensities and beam losses related only to the burn-off effect, the luminosity would be described as

$$L_{\text{bo}}(\tau) = \frac{L_i}{[1 + \varepsilon N_i(\tau - 1)]^2} \,, \tag{2.37}$$

being L_i the initial peak luminosity, decreasing with the number of turns τ and the intensity of the beam N_i. Accounting for diffusive effects, a more refined model is introduced

$$L(\tau) = L_{\text{bo}}(\tau)[1 + \zeta(\tau) f(DA(\tau))] \tag{2.38}$$

where ζ describes the pseudo-diffusive effects and $f(DA(\tau))$ maps the evolution of the DA over turns. As burn-off effects target the core of the bunch distributions, whereas diffusive effects affect the bunches' tails, their effects can be considered to be independent. Redefining the initial intensities by introducing the pseudo-diffusive term $\mathcal{D}_i$, the evolution of the luminosity would be

$$L(\tau) = \frac{L_i}{[1 + \varepsilon N_i(\tau - 1)]^2} - [1 + D^2(\tau)] e^{-D^2(\tau)} [2 - (1 + D^2(\tau)) e^{-D^2(\tau)/2}] \,. \tag{2.39}$$

2.4 Luminosity levelling

A fundamental consideration in collider design concerns the distinction between peak and integrated luminosity. Although peak instantaneous luminosity serves as the traditional figure of merit for collider performance, from an experimental perspective, the integrated luminosity—representing the total accumulated collision statistics—is the quantity of primary interest. Several strategies exist to maximise integrated luminosity: increasing peak performance, extending the duration of physics fills, or exploring alternative operational schemes. However, these approaches must be balanced against the

fundamental constraints imposed by the detector technology and the failure probability of the accelerator.

Modern particle detectors face intrinsic limitations on event processing capabilities, including restrictions on the number of simultaneous interactions per bunch crossing (pile-up), longitudinal event density, and total event rate. These constraints arise from charge collection times, trigger bandwidth, data acquisition throughput, and event reconstruction complexity. Equally important is the luminosity stability: prolonged operation at constant luminosity simplifies systematic uncertainty evaluation and optimises detector performance, as many subsystems are calibrated for specific pile-up conditions.

Within this framework, *luminosity levelling* emerges as an optimal operational strategy. Rather than allowing the luminosity to follow its natural exponential decay due to beam degradation and particle losses, levelling deliberately maintains a constant luminosity plateau over extended periods. This is achieved by initially operating the machine below its maximum potential—effectively "spoiling" the peak luminosity—and progressively relaxing these constraints as the beam quality naturally deteriorates. The machine is thus designed to achieve a virtual peak luminosity substantially exceeding the maximum value tolerable by detector pile-up limitations, with active control mechanisms reducing this peak to sustainable operational levels. The efficacy of luminosity levelling depends critically on the maximisation ofthe initial beam quality and the virtual peak luminosity, as this determines the duration over which constant luminosity can be maintained [35, 36]. By sacrificing peak instantaneous performance in favour of operational stability and extended data-taking periods, levelling schemes can significantly enhance integrated luminosity delivery while respecting detector constraints. Different types of technique can be used to approach the levelling purpose:

- separation offset,
- crossing angle variation,
- crab cavity RF voltage modulation,
- dynamic β^* squeeze .

In each case, a collision-related beam parameter is varied as a function of storage time, so as to lower the actual luminosity compared with the maximal achievable one at the beginning of the physics collisions and increase the luminosity value during the fill. As a result, the luminosity is roughly constant during the data collection. In the following, the main techniques are described, evaluating both advantages and disadvantages. Figure 12 provides a schematic illustration of these levelling methodologies.

Among the most relevant levelling techniques, beam separation through *transverse offsets* offers several practical advantages.

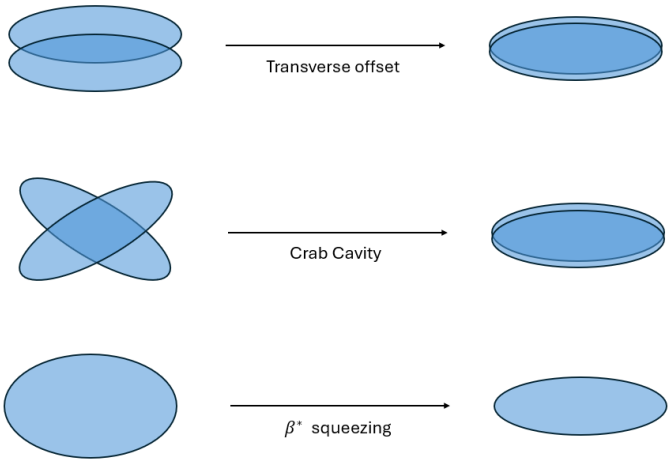

Figure 12: Visual representations of luminous regions for different levelling approaches

This technique is based on the controlled reduction of the overlap area between the two beams at the interaction point. At the beginning of the fill, when the beam intensity is maximum, a transverse separation Δx is introduced between the trajectories of the two beams. This separation reduces the overlap integral of the transverse profiles, consequently decreasing the instantaneous luminosity to a predefined target value L_{target}.

The instantaneous luminosity in the presence of an offset can be expressed as:

$$L = \frac{N_1 N_2 f_{\text{rev}} k_b}{4\pi \sigma_x^* \sigma_y^*} \exp\left(-\frac{\Delta x^2}{4\sigma_x^{*2}}\right) \tag{2.40}$$

where N_1 and N_2 represent the bunch populations, f_{rev} the revolution frequency, k_b the number of bunches, σ_x^* and σ_y^* the transverse beam sizes and Δx the applied transverse separation. During the fill, the beams undergo natural degradation as a result of beam-beam collisions, interactions with residual gas, and other loss mechanisms. To compensate for this intensity reduction and maintain constant luminosity, the offset is progressively reduced according to a time-dependent function $\Delta x(t)$, thus increasing the effective overlap area as the bunch populations decrease.

This method is straightforward to implement, provides rapid response, and can be applied independently at each interaction point using local orbit bumps. Furthermore, it enables precise control of pile-up, maintaining a constant average number of collisions per bunch crossing—a critical requirement for optimal detector performance and event reconstruction.

However, this approach introduces significant operational challenges. The beam separation generates a position-dependent beam-beam force that modifies the tune

spread and potentially reduces the beam stability region. Studies indicate the existence of a critical separation value that minimises the tune footprint, beyond which beam stability deteriorates considerably. This constraint poses serious complications for maintaining stable conditions in all circulating bunches.

At hadron colliders, another parameter may be dynamically adjusted during a fill to control instantaneous luminosity: the *crossing angle* between colliding beams. In this scheme, the crossing angle is progressively reduced during the fill to counteract the natural luminosity degradation caused by beam burn-off, thus recovering instantaneous luminosity and maximising the integrated luminosity delivered over the full duration of the fill. In the LHC, crossing angles are a crucial operational parameter, designed to provide sufficient beam separation and mitigate long-range beam-beam interactions at points adjacent to the main collision regions [37]. However, larger crossing angles impose a luminosity penalty, with experimental measurements indicating that high-luminosity experiments observe approximately 60% of the theoretical luminosity achievable in the absence of crossing angles, due to the geometric luminosity reduction factor that depends on the crossing angle, bunch length, and beam size [37]. To optimise integrated luminosity delivery, an anti-levelling strategy based on dynamic cross-angle reduction has been operationally implemented at the LHC [38]. This technique exploits the natural decrease in beam intensity during fills due to luminosity burn-off: as bunch populations diminish over time, the long-range beam-beam effects become less severe, allowing for a stepwise reduction of the crossing angle while maintaining acceptable beam separation [38].

The beam-beam constraints that limit the crossing angle reduction in anti-levelling schemes can be overcome through the use of crab cavities, introducing a technologically advanced levelling mechanism that exploits RF-induced bunch rotations to dynamically control the luminosity. These specialised cavities impart a longitudinally-dependent transverse kick to the particles within each bunch, effectively rotating the bunch in the transverse-longitudinal phase space and allowing precise modulation of the beam overlap at the interaction point. In modern colliders, the beams cross at an angle θ_c necessary to separate the beams outside the interaction point and avoid unwanted parasitic collisions. Due to the elongated longitudinal structure of the bunches ($\sigma_s \gg \sigma_x^*, \sigma_y^*$), the crossing angle significantly reduces the effective overlap between the bunches during collision, introducing a geometric luminosity reduction factor. Crab cavities compensate for this effect by applying an oscillating transverse electromagnetic field that varies along the bunch length. For a bunch traversing a crab cavity, the imparted transverse deflection is given by:

$$\Delta x'(s) = \frac{eV_{\mathrm{crab}}}{pc} \sin\left(\frac{\omega_{\mathrm{RF}} s}{c}\right), \tag{2.41}$$

where V_{crab} is the crab-cavity voltage, ω_{RF} the angular frequency of the RF, and z the longitudinal coordinate within the bunch. This s-dependent deflection induces a ro-

tation of the bunch in the (x, s) plane, allowing the bunches to present themselves head-on at the interaction point despite the crossing angle. The luminosity with fully activated crab cavities recovers the maximum geometric value:

$$L_{\text{crab}} = \frac{N_1 N_2 f_{\text{rev}} k_b}{4\pi \sigma_x^* \sigma_y^*} \cdot F_{\text{crossing}} \tag{2.42}$$

where $F_{crossing}$ is the geometric reduction factor that can be arbitrarily close to unity by varying the crabbing amplitude. For luminosity levelling, the amplitude of the voltage of the crab cavity $V_{\text{crab}}(t)$ is modulated over time. By reducing the crabbing, the effective overlap between bunches is decreased in a controlled manner, allowing constant luminosity to be maintained at the target value while beam intensities decay. This technique offers the advantage of keeping the beams perfectly centred at the interaction point, eliminating the need for transverse separations and preserving the geometric optimality of the collisions.

Although successfully deployed in electron-positron colliders, their application to hadron machines for luminosity levelling remains novel. This technique offers several compelling features: independent luminosity control at each interaction point, operational flexibility through simple voltage adjustments, and the ability to maintain constant luminosity by progressively compensating for natural beam degradation.

Nevertheless, several concerns must be addressed. The limited operational experience with crab cavities in proton beams introduces uncertainties regarding long-term stability and beam dynamics. In addition, the system imposes stringent requirements on the longitudinal distribution of the vertex and the position of the beam, potentially increasing the susceptibility to collective instabilities. Perhaps most critically, the technique demands exceptional precision: cavity jitter—manifested as phase or timing fluctuations—can cause beam misalignment at the interaction point, degrading luminosity, or even preventing collisions completely [39, 35].

In the context of this work, the *dynamic squeeze* β^* would be the levelling scheme chosen to perform the desired analysis.

This method starts with a beam that has a larger-than-nominal cross-section. As the luminosity naturally decays, the beam is progressively ”squeezed” to maintain a constant luminosity. The fundamental principle is that the stability of the beam is ensured by a tune spread, which is achieved through non-linearities like those from the beam-beam effect or from octupole magnets. The procedure has different advantages to be considered:

- Stable event density: Experiments benefit from a constant longitudinal vertex density, which is critical for event detection;
- Consistent tunes: The beam tunes remain constant throughout the fill, which improves operational stability;

- Enhanced stability: This method offers a larger and more stable region of Landau damping, especially when the squeeze is performed while the beams are already in head-on collision. This avoids the negative effects associated with octupole magnets, such as a reduction in DA;
- Constant stability diagram: Unlike levelling with an offset, the stability diagram remains constant during the procedure because the tune spread from head-on beam-beam interactions does not depend on the beam size.

However, some drawbacks should be analysed, first of all the operational complexity, related to the beam orbit: the orbit must be kept perfectly constant during the squeeze to ensure the beams remain in collision, requiring a robust feed-forward system, which deviates from standard operational procedures. In addiction, while this method is generally more stable than the offset method, its reliance on precise orbit control and nonlinear effects introduces the potential for complications if not managed carefully [35].

2.5 β^* levelling: model 1

The starting point for a rigorous theoretical description of β^* levelling is the fundamental equation

$$\frac{dN}{dt} = -\sigma_{\mathrm{int}} n_{\mathrm{c}} L(t) \tag{2.43}$$

describing the time variation of the intensity of the beam. Assuming the luminosity to be kept constant in time, as happens during the levelling process, $L(t) = L_\ell$, Eq. (2.43) has a simple solution:

$$N(t) = N_i - \sigma_{\mathrm{int}} n_{\mathrm{c}} L_\ell t \,. \tag{2.44}$$

Taking into account the equation describing the evolution of intensity over time and the definition of luminosity with time-dependent β^*

$$L(t) = \frac{f_{\mathrm{rev}} \gamma_{\mathrm{r}} N(t)^2}{4\pi\epsilon^* \beta(t)^* k_b} F \tag{2.45}$$

where

$$F(\theta_c, \sigma_s, \sigma^*) = \frac{1}{\sqrt{1 + \left(\frac{\theta_c \sigma_s}{2\sigma^*}\right)^2}} \,. \tag{2.46}$$

It is evident how the dependence on $\beta^*(t)$ is both explicit and implicit in the definition of luminosity, by the term F, as

$$\sigma^* = \sqrt{\frac{\epsilon^* \beta^*}{\gamma_{\mathrm{r}}}} \,. \tag{2.47}$$

The luminosity definition in Eq. (2.45) can be rewritten as

$$L(t) = \frac{\lambda_1}{\beta^*(t)} N(t)^2 \frac{1}{\sqrt{1 + \frac{\lambda_2}{\beta^*(t)}}} \tag{2.48}$$

where

$$\lambda_1 = \frac{\gamma_{\mathrm{r}} f_{\mathrm{rev}}}{4\pi \epsilon^* k_b} \,, \qquad\qquad \lambda_2 = \frac{\theta_c^2 \sigma_s^2 \gamma_{\mathrm{r}}}{4\epsilon^*} \,. \tag{2.49}$$

As the levelling process takes place whenever $\beta^*(t)$ is varied, an analytical rule may be derived connecting $\beta^*(t)$ and $N(t)$, so that the time-evolution required for the levelling of β^* can be computed.

$$\beta^*(t) = \frac{-\lambda_2 + \sqrt{\lambda_2^2 + 4\left(\frac{\lambda_1}{L_\ell}\right)^2 N_i^4 \left(1 - \frac{\sigma_{\mathrm{int}} n_{\mathrm{c}} L_\ell}{N_i}\right)^2}}{2} \,. \tag{2.50}$$

The levelling process ends when $\beta^*(t) = \beta^*(t_{\max}) = \beta^*_{\min}$, so after a time

$$t_\ell = \frac{N_i}{\sigma_{\mathrm{int}} n_{\mathrm{c}} L_\ell} \left(1 - \sqrt{\frac{L_\ell}{\hat{L}}}\right) \,. \tag{2.51}$$

The introduced parameter $\hat{L}$, defined as $\hat{L} = \Xi_{\max} N_i^2 = \frac{\tilde{\Xi}}{\beta^*_{\min}} N_i^2$ represents the virtual instantaneous peak luminosity of the collider at the beginning of the fill, i.e. the luminosity obtained using the initial beam parameters and assuming $\beta^*(t=0) = \beta^*_{\min}$ and we have $L_\ell < \hat{L}$. This definition of $\hat{L}$ is the natural way to compare the virtual performance of a collider designed with an optics that achieves $\beta^*_{\min}$ at the collision point with the case where levelling is performed. In particular, it is evident that for $L_\ell \to \hat{L}$, the levelling time $t_\ell \to 0$ and the levelling process results are erased. The levelling time model of Eq. (2.51) seems to agree with the one presented by [36]. However, comparing the model with the data for t_ℓ and $\beta^*(t)$ from the LHC Run 3, the model seems not to perfectly adapt.

2.6 Limits of the levelling model 1

When analysing the levelling model in 2.5, a key point should be taken into account. The integrated luminosity of a single fill without luminosity levelling, using the luminosity model in Eq. (2.35) reads as

$$\mathcal{L}_{\rm int}(t_{\rm fill}) = \int_0^{t_{\rm fill}} dt L(t) = \frac{\Xi N_i^2 t_{\rm fill}}{1 + \sigma_{\rm int} n_{\rm c} \Xi N_i t_{\rm fill}} \tag{2.52}$$

The assumption that naturally arises is that the case of levelling should leave invariant the integral luminosity, and it is required then that

$$\mathcal{L}_{\rm int}(t_{\rm fill}) = L_\ell t_\ell + \int_0^{t_{\rm end}} dt L(t)\,, \tag{2.53}$$

where L_ℓ and t_ℓ are, respectively, the levelled luminosity and the levelling time, t_{end} the time interval for the luminosity decay and $L(t)$ the model describing the luminosity decay after the levelling ends.

However, it is possible to show that, using the levelling time defined in Eq. (2.51), the integrated luminosity shows a decrease in the levelling case, invalidating the expected Eq. (2.53). In particular,

$$\mathcal{L}_{\rm int}(t_{\rm fill}) \approx \hat{L} t_{\rm fill} \qquad t_{\rm fill} \ll 1 \tag{2.54}$$

$$\lim_{t_{\rm fill}\to\infty} \mathcal{L}_{\rm int}(t_{\rm fill}) = \frac{N_i}{\sigma_{\rm int} n_{\rm c}} \tag{2.55}$$

and

$$\begin{aligned}\mathcal{L}_{\rm int}(t_\ell, t_{\rm fill} - t_\ell) &= L_\ell t_\ell + \int_0^{t_{\rm fill}-t_\ell} dt\, L(t) \\ &= \frac{N_i}{n_c \sigma_{\rm int}} \left(1 - \sqrt{\frac{L_\ell}{\hat{L}}}\right) \frac{1 - 2\frac{\hat{L}}{L_\ell}\left(1 - \sqrt{\frac{L_\ell}{\hat{L}}}\right)^2 + 2\frac{\hat{L}}{N_i}\left(1 - \sqrt{\frac{L_\ell}{\hat{L}}}\right)\sigma_{\rm int} n_{\rm c} t_{\rm fill}}{1 - \frac{\hat{L}}{L_\ell}\left(1 - \sqrt{\frac{L_\ell}{\hat{L}}}\right)^2 + \frac{\hat{L}}{N_i}\left(1 - \sqrt{\frac{L_\ell}{\hat{L}}}\right)\sigma_{\rm int} n_{\rm c} t_{\rm fill}}\,,\end{aligned} \tag{2.56}$$

from which one derives

$$\mathcal{L}_{\rm int}(t_\ell, t_{\rm fill} - t_\ell) \approx L_\ell t_{\rm fill} \qquad t_{\rm fill} \ll 1 \tag{2.57}$$

and

$$\lim_{t_{\rm fill}\to\infty} \mathcal{L}_{\rm int}(t_\ell, t_{\rm fill} - t_\ell) = \frac{2N_i}{\sigma_{\rm int} n_{\rm c}} \left(1 - \sqrt{\frac{L_\ell}{\hat{L}}}\right) \tag{2.58}$$

The integrated luminosity is a monotonically increasing function and it can be verified that if

$$\sqrt{\frac{L_\ell}{\hat{L}}} < \frac{1}{2} \tag{2.59}$$

then the limit of $\mathcal{L}(t_\ell, t_{\rm fill} - t_\ell)$ is greater than the limit of $\mathcal{L}(t_{\rm fill})$.

One can also evaluate the value of $t_{\rm fill}$ for which the levelling of luminosity accumulates luminosity in the same way as in the case without levelling. A quadratic equation provides the answer to this question, namely

$$a t_{\rm fill}^2 + b t_{\rm fill} + c = 0\,, \tag{2.60}$$

where

$$\begin{cases} a = \frac{L_\ell \hat{L} \sigma_{\rm int}^2 n_c^2}{2N_i} \left(\sqrt{\frac{L_\ell}{\hat{L}}} - 1\right) \left(\sqrt{\frac{L_\ell}{\hat{L}}} - \frac{1}{2}\right) \\ b = 2\sigma_{\rm int} n_c \hat{L} \left(\frac{L_\ell}{\hat{L}} \sqrt{\frac{L_\ell}{\hat{L}}} - \frac{L_\ell}{\hat{L}} - 2\sqrt{\frac{L_\ell}{\hat{L}}} + 1\right) \left(\sqrt{\frac{L_\ell}{\hat{L}}} - \frac{1}{2}\right) \\ c = N_i \left(\sqrt{\frac{L_\ell}{\hat{L}}} - 1\right) \left(\frac{L_\ell}{\hat{L}} - 4\sqrt{\frac{L_\ell}{\hat{L}}} + 2\right) \end{cases} \tag{2.61}$$

2.7 β^* levelling: model 2

The model presented in 2.5 can be improved taking into account the DA model, as presented in 2.3. In particular, the model considering only burn-off information has the advantage of being analytically handled, but can not include losses due to non linearities. This means that the luminosity may be described as

$$\begin{aligned} \frac{L(\bar{t})}{L(0)} &= \frac{L_i}{[1 + \frac{\varepsilon N_i}{f_{\rm rev}}(\bar{t} - 1)]^2} - [1 + D^2(\bar{t})] e^{-D^2(\bar{t})} \left[2 - (1 + D^2(\bar{t})) e^{-D^2(\bar{t})/2}\right] \\ &= \mathcal{F}(\bar{t}) - \mathcal{G}(\bar{t})\,. \end{aligned} \tag{2.62}$$

This definition of the luminosity model may be used to redefine Eq. (2.43) as

$$\frac{dN}{d\bar{t}} = \frac{-\sigma_{int} n_c}{f_{rev}} L(\bar{t}) = \frac{-\sigma_{int} n_c}{f_{rev}} \mathcal{F}(\bar{t}) + \frac{\sigma_{int} n_c}{f_{rev}} \mathcal{G}(\bar{t}). \tag{2.63}$$

Keeping then the luminosity value constant at $L(t) = L_\ell$, the solution of Eq. (2.63) is the same as Eq. (2.44). However, It should be noted that the beta variation with respect to time is different and is given by the positive solution of the

$$\beta^{*2}(\bar{t}) + \lambda_2 \beta^*(\bar{t}) - \left(\frac{\hat{L}}{L_\ell}\right)^2 \left(\frac{\beta^*_{min}}{F_{min}}\right)^2 \left(\frac{1}{1 - \frac{L(0)}{L_\ell} \mathcal{G}(\bar{t})}\right)^2 \left(1 - \frac{\sigma_{int} n_c L_\ell}{f_{rev} N_i}\right)^4 = 0\,, \tag{2.64}$$

so that

$$\beta^*(\bar{t}) = \frac{-\lambda_2 + \sqrt{\lambda_2^2 + 4\left(\frac{\hat{L}}{L_\ell}\right)^2\left(\frac{\beta^*_{\min}}{F_{\min}}\right)^2\left(\frac{1}{1-\frac{L(0)}{L_\ell}\mathcal{G}(\bar{t})}\right)^2\left(1-\frac{\sigma_{\text{int}}n_c L_\ell}{f_{\text{rev}}N_i}\right)^4}}{2}\,. \tag{2.65}$$

The levelling time $\bar{t}_\ell$ is defined for $\beta^*(\bar{t}_\ell) = \beta^*_{\min}$, so

$$\frac{\sigma_{\text{int}}n_c L_\ell}{f_{\text{rev}}N_i}\bar{t}_\ell + \sqrt{\frac{L_\ell}{\hat{L}}}\sqrt{1-\frac{L(0)}{L_\ell}\mathcal{G}(\bar{t}_\ell)} - 1 = 0\,. \tag{2.66}$$

2.8 HL-LHC

The analysis of the optimal levelling scheme represents a fundamental point for the optimisation of the integrated luminosity of the successor to the LHC, *High Luminosity LHC*, or, briefly, *HL-LHC* [17].

HL-LHC represents the luminosity upgrade of the LHC, which will remain the world's highest-energy accelerator for decades. This upgrade is a top priority of the European Strategy for Particle Physics Update with the primary goals being a fivefold increase in the instantaneous collision rate and a tenfold increase in integrated luminosity compared to the nominal design. Achieving this requires substantial research and development, including advanced technologies like: $11\,\mathrm{T}$ to $12\,\mathrm{T}$ superconducting magnets, superconducting crab cavities for beam rotation, advanced beam collimation technologies, high-current superconducting links. The major upgrades are resumed in Fig. 13

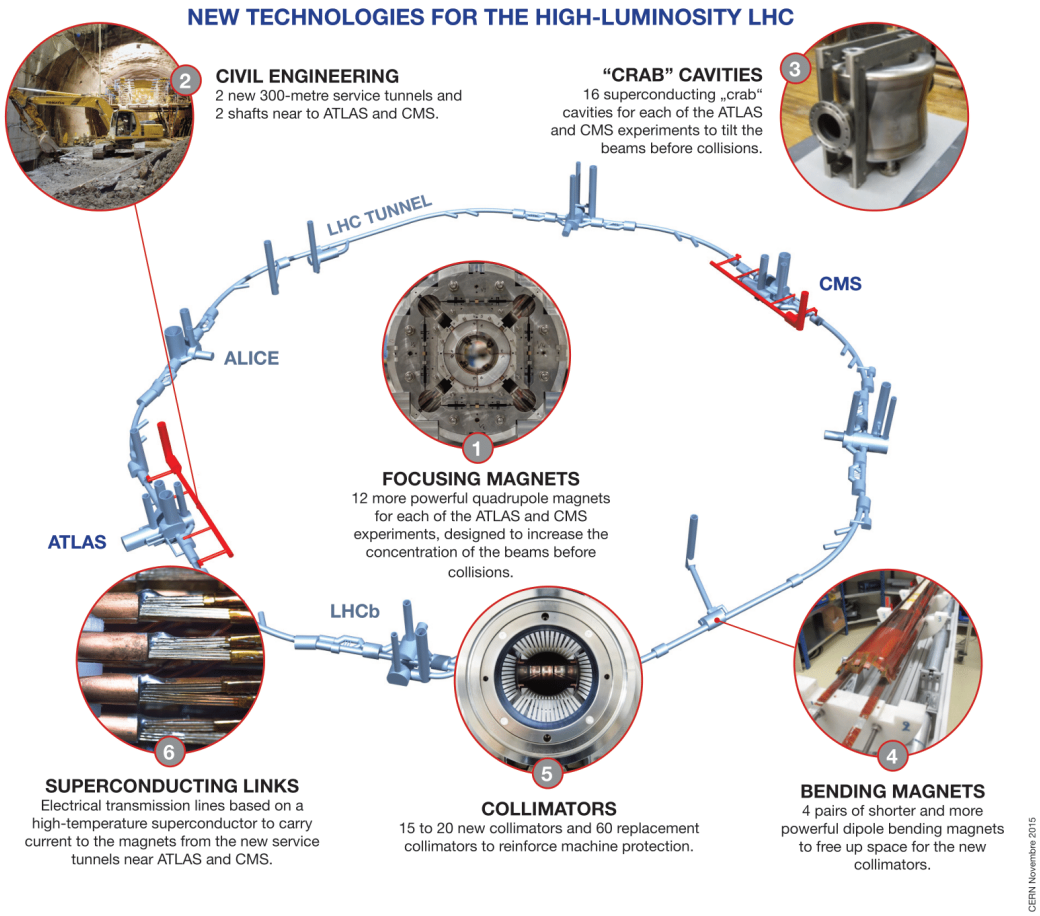

Figure 13: The HL-LHC designed upgrades [40]

The project is a global effort, with contributions from institutions and universities in CERN non-member states such as the USA, Japan, China, Canada, and Russia, as well as leading institutions from member states like INFN (Italy), CIEMAT (Spain), and STFC (UK).

Different elements of the existing LHC would undergo a drastic change and improvement, as they would become either vulnerable to breakdown and accelerated ageing or because they may become a bottleneck for operation at higher performance levels and in a higher radiation environment. In particular, the upgrades will affect mainly the triplet magnets and the associated correctors, which fail above $300\,\mathrm{fb}^{-1}$, cryogenics, collimation, dispersion suppression (DS) region and superconducting (CS) links.

The HL-LHC upgrade aims to achieve high performance in a wide range of parameters. The intensity of the bunch will increase from 1.15×10^{11} to 2.2×10^{11} protons. The beam emittance will be reduced from $3.75\,\mu\mathrm{m}$ to $2.50\,\mu\mathrm{m}$. The baseline operation will

be a $25\,\mathrm{ns}$ bunch spacing. One of the main challenges is reducing the β^* value at the interaction point. This reduces the transverse beam size, increasing luminosity. However, a smaller β^* requires larger and more powerful triplet quadrupoles to compensate for aberrations and increase acceptance and a larger crossing angle, which reduces the geometric overlap of the beams and consequently luminosity. This effect is quantified by the reduction factor F. The most elegant solution to this problem is the use of crab cavities, which tilt the bunches to make them collide head-on, neutralising the effect of the crossing angle. With crab cavities, the reduction factor F increases from 0.34 to 0.72. This allows the full potential of low β^* values, such as $15\,\mathrm{cm}$, to be exploited. Peak luminosity is also limited by factors such as heat deposited from collision debris and the cooling limits of superconducting magnets. To mitigate these effects, the HL-LHC project is exploring new strategies, such as increasing engineering margins for magnet power and using a dynamic β^* "squeeze" scheme to optimise the event pile-up density throughout the beam fill. The design performance of the upgraded machine is still evolving, but some forecasts and predictions have been made: the peak luminosity value would be kept at $5 \times 10^{34}\,\mathrm{cm}^{-2}\mathrm{Hz}$ during all the working periods of the machine, including and initial phase of "luminosity learning", when the peak luminosity value would be lowered to gain familiarity with the new framework. If the performance could go beyond the designed ones and the upgraded detectors accepted a higher pile-up, the performance would reach a higher peak luminosity value, of about $7.5 \times 10^{34}\,\mathrm{cm}^{-2}\mathrm{Hz}$ with levelling. This would lead to about $350\,\mathrm{fb}^{-1}/\mathrm{year}$, for a total of $4000\,\mathrm{fb}^{-1}$ at the end of the last year of operational run, 2041 [41, 42].

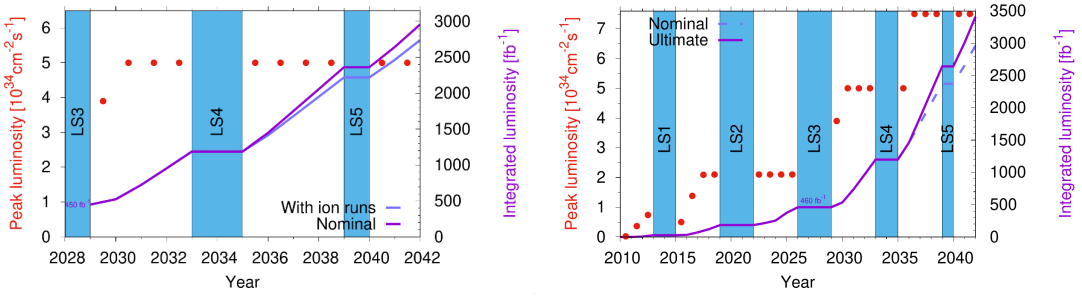

Figure 14: On the left, forecast for peak luminosity (red dots) and integrated luminosity (violetline) of the HL-LHC era with nominal HL-LHC parameters; on the right, peak luminosity (red dots) and integrated luminosity (violetline) as an overview of the LHC operations and HL-LHC nominal and ultimate trends [42].

3 LHC Run 3 analysis

To evaluate the performance of the optimization scheme described in Section 4, Monte Carlo simulations are employed (see Section 5). This chapter presents a discussion of the LHC Run 3 data used to construct the distributions for the Monte Carlo simulation framework.

3.1 Run 3 Data analysis

Before introducing the implemented optimisation strategy, the data analysis performed on LHC-Run 3 parameters will be presented and discussed in detail. The purpose of this analysis is to characterise the distributions of key parameters in the three years of the ongoing Run 3 (2022, 2023, and 2024). The resulting distributions will serve as input for Monte Carlo simulations, which are used to evaluate the feasibility of the proposed optimisation process. The analysed data have been collected by the ATLAS collaboration at IP1, even though the beam separation data are from IP1 and IP5.

For each physical parameter under investigation, a curated collection of LHC fill data was preprocessed and stored in serialised Python pickle format. The selection criterion adopted for the fills consisted in choosing those characterized by the highest instantaneous luminosity values. These datasets, prepared by PhD candidate Maria Aquilina, were subsequently analysed using custom Python scripts developed for this work.

For clarity, the operational scheme investigated and the key terminology used in subsequent sections are here defined. An LHC *fill* is a complete operational cycle of the accelerator, from the moment particle beams are injected until they are safely disposed of. One single fill is composed by different steps: the process begins with injection, where particle beams are delivered from the pre-accelerators into the main LHC ring. Next, the beams undergo an energy ramp phase, being gradually accelerated to their final collision energy. This process takes a significant amount of time (about 20 minutes), but is critical for reaching the energy required for groundbreaking physics. After acceleration, the beams are squeezed at the interaction points, increasing their density to maximise the chances of particle-on-particle collisions. This leads to the most important part of the fill: the collision and data-taking phase. For many hours, the beams collide in the centre of the detectors, and experiments collect collision data. As the beams lose particles over time, the luminosity gradually decreases. Finally, when the luminosity drops below a useful level, or if a technical issue occurs, the fill is brought to an end by dumping the beams into a safe absorber. The time interval between the end of a fill and the start of the next is called *turnaround time*.

Different types of fills exist, e.g. proton physics, ions physics, special run, intensity ramp-up, etc.. However, the interest of this work focuses only on the high-luminosity proton physics fills.

The analysis characterises the entire operational cycle of an LHC fill, which includes both the zero-luminosity setup phase and the non-zero luminosity collision phase. The goal is to provide a complete description of the fill, highlighting the importance of considering the entire process and not just the data-taking period.

The most important LHC and beam characteristics to be analysed are:

1. **Instantaneous luminosity**, $L(t)$ [$\mu\mathrm{b}^{-1}\mathrm{Hz}$] (or [$\mathrm{cm}^{-2}\,\mathrm{Hz}$]), it will be analysed with a strong focus on the levelling value L_ℓ, kept constant during the levelling time;

2. **Levelling time**, t_ℓ [h] (or [s]) and the **decay time**, t_{dec}, [h] (or [s]), the time duration of the levelling and the time interval between the end of the levelling and the end of the fill, respectively;

3. **Beam intensity** [charge] as a function of time, $N(t)$, with a special emphasis on the value measured at the start of levelling (N_i) and that at the end of the levelling ($N(t_\ell)$);

4. **The beta function value at the interaction point** β^* [cm] as a function of time $\beta^*(t)$, in particular its value at the start of stable beams (β_0^*) and that evaluated at t_ℓ, $\beta^*(t_\ell)$;

5. **Turnaround time** t_{ta} [h], defined as the time interval between the end of a fill and the start of the next fill;

6. **Time between Failure** TBF [h], a metric used in reliability engineering and representing the average time a system or a repairable component operates correctly before a failure occurs; for an accelerator like the LHC, a “failure” is not necessarily a catastrophic event. Instead, it is any unexpected issue that forces an LHC fill—the complete operational cycle from injection to beam dump—to end prematurely.

7. **The characteristic of the DA model** as presented in 2.3, in particular the decay part of the luminosity was analysed to obtain the value of ρ, κ and ε.

Data analysis was performed for each year of LHC Run 3, looking for the distributions of the various physical parameters.

In Fig. 15, three examples of real LHC fills, one for each year, have been reported. In particular, the reader may appreciate the evolution of luminosity over time (blue line), the evolution of the beam intensity (red line) and the evolution of the β^* (green line).

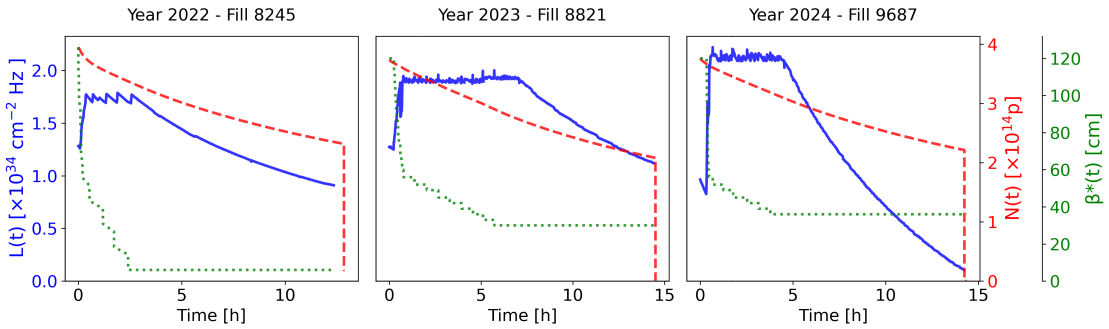

Figure 15: From left to right, examples of fills of 2022, 2023, 2024

The instantaneous luminosity data inevitably contain irregularities arising from various sources, primarily beam repositioning operations performed to re-optimise the luminosity. The main irregularities were preprocessed and removed from the raw Massi files [43] prior to analysis, ensuring that the dataset under examination was free of such artefacts.

For each fill, the values of L_ℓ, t_ℓ, t_{dec} have been extracted by analysing the data of $L(t)$. Knowing these characteristic times, it was possible to extract the value of N_i, $N(t_\ell)$, β_i^* and $\beta^*(t_\ell)$ from the $N(t)$ and $\beta^*(t)$ data. By analysis of the decay part of $L(t)$, it has been possible to fit the DA model 2.3, to extract the $\rho, \kappa, \varepsilon$ values. In particular, in Fig. 16, the fitting process of the DA model on the Fill 9687 of 2024 reported in Fig. 15 is presented. t_{ta} and MTBF data were also analysed.

The most stable, coherent, and reliable data were found to be those of the 2024 LHC run. In particular, the 2022 data exhibited a lack of consistency between parameter values. This may be attributed to the fact that 2022 marked the first year of Run 3, during which operational parameters were still being established and optimised. The 2023 dataset, instead, suffered from reduced reliability due to operational difficulties encountered during that year. Multiple faults requiring extended repair and recovery periods significantly reduced the data-taking period , including a vacuum leak that caused approximately 50 days of downtime and RF finger module problems that limited beam intensity. All of these factors led to the choice of 2024 data to feed the Monte Carlo simulator.

The values extracted from each year will be reported in table 1. The parameter analysis for year 2024 is reported in the following.

Regarding the values of L_ℓ, the data have been modelled with a uniform distributed, as shown in Fig. 17, with a mean value of $19\,945\,\mu\mathrm{b}^{-1}/\mathrm{Hz}$ and a standard deviation of $\sigma = \pm 575\,\mu\mathrm{b}^{-1}/\mathrm{Hz}$. In the right part of 17, the values of L_ℓ are reported as a function of the number of fills, so as a function of time: in fact, the number of each fill is assigned sequentially, making each assignment a chronological mirror of fill production. In particular, the plot shows a tendency to explore different values for the L_ℓ parameter, with

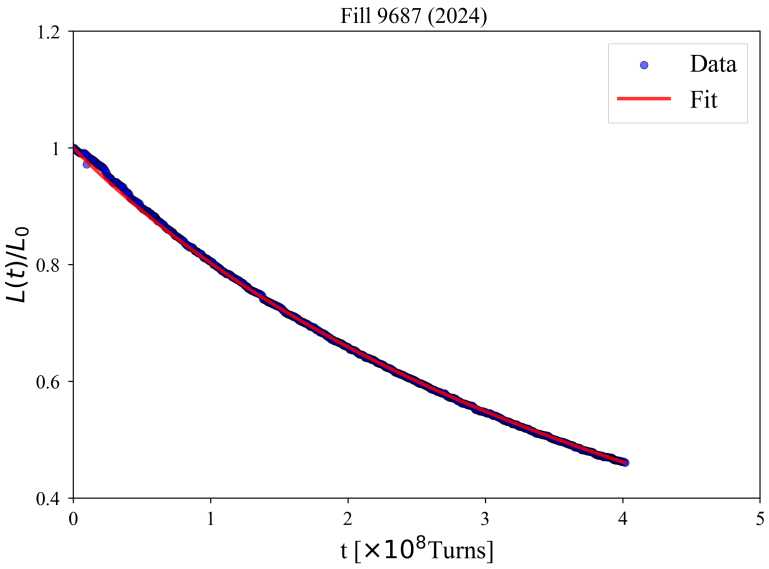

Figure 16: the decay part of the luminosity has been fitted using the DA model. Luminosity data were normalised over the maximum value ($L_\ell = L_0$) and time was expressed in units of turns

a trend of exploring higher values rather than lower ones.

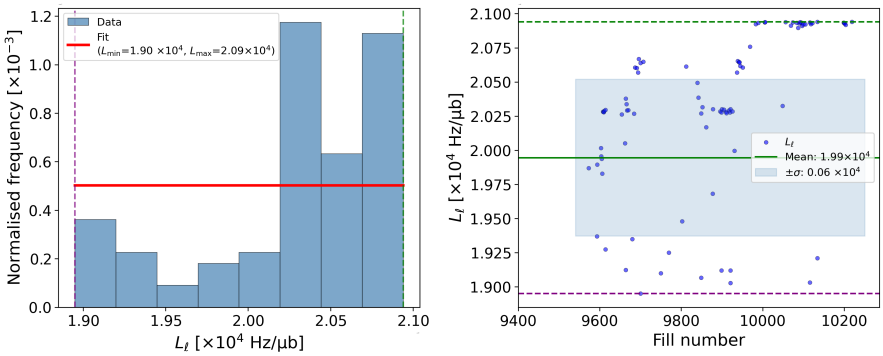

Figure 17: On the left, the histogram of the L_ℓ values, on the right L_ℓ as a function of the fill number

The L_ℓ acted as a descriptive measure to characterise the luminosity-levelling part of the fill, the decay time t_{dec} was used as one of the descriptors for the decay part of the fill. The decay time of each fill was extracted by the definition of the interval between the end time of the fill and the end time of levelling, that is, $t_{\mathrm{end}} - t_\ell$. As one may appreciate in Fig. 18, the distribution of t_{dec} for 2024 was found to be a Gaussian distribution with mean value $5.75\,\mathrm{h}$ and $\sigma = 2.26\,\mathrm{h}$. The scatter plot showed a tendency,

over the year, to explore a region between $4\,\mathrm{h}$ and $8\,\mathrm{h}$. In particular, a truncation at $1.5\,\mathrm{h}$ is visible, whereas t_{dec} values above $8\,\mathrm{h}$ are rare.

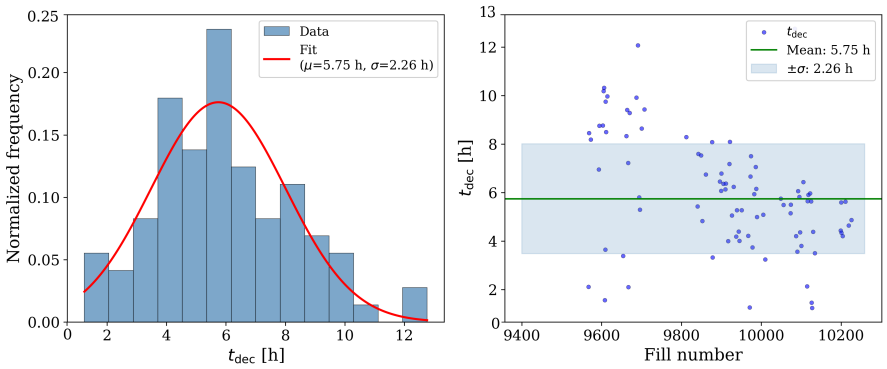

Figure 18: On the left, the histogram of t_{dec} values, on the right t_{dec} as a function of fill number

Each fill was also described by the intensity value of the beam at $t = 0$ (N_i) and the beta function values at the interaction point β^*, both at $t = 0$ and $t = t_\ell$.

In 2024, as shown in Fig. 19, the initial intensity was normally distributed, with a cut at $3.85 \times 10^{14}\,\mathrm{p}$, a mean value of $3.75 \times 10^{14}\,\mathrm{p}$ and $\sigma = 0.07 \times 10^{14}\,\mathrm{p}$. As shown in Fig. 20, for each fill the initial value of β^* was $120\,\mathrm{cm}$, while the value at t_ℓ was $36\,\mathrm{cm}$ for the first part of the year and $30\,\mathrm{cm}$ for the remaining part.

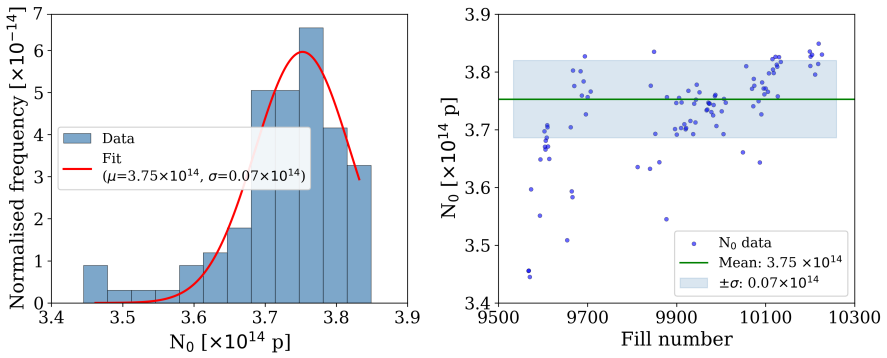

Figure 19: On the left, the distribution of the N_i parameter, on the right N_i as a function of fill number

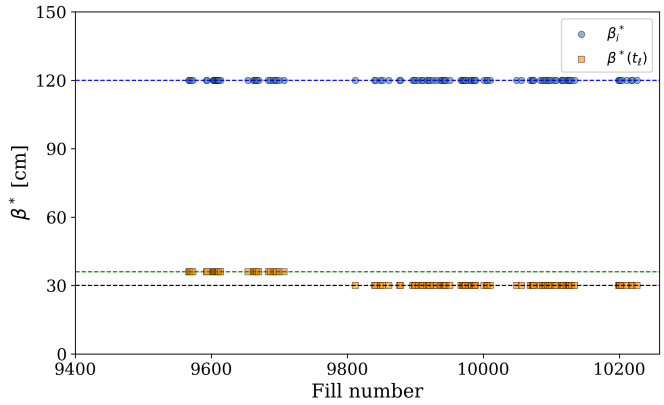

Figure 20: Two symbols describe, for each fill, the values of the β^* at the start of the fill (blue dot) and at the end (orange square)

The decay part of the luminosity, occurring at t_{dec}, was further examined by fitting the DA model described in 2.3, to evaluate the distribution of the fundamental parameters ρ and ε. A preliminary analysis was performed on the selected fills, scanning all possible values of the κ parameter (in a range between 0.5 and 1.5, found to be the typical range of this parameter) to evaluate which was related to the minimum chi-squared value (as shown in Fig. 21). The determined value of $\kappa = 0.92$ is valid for the year.

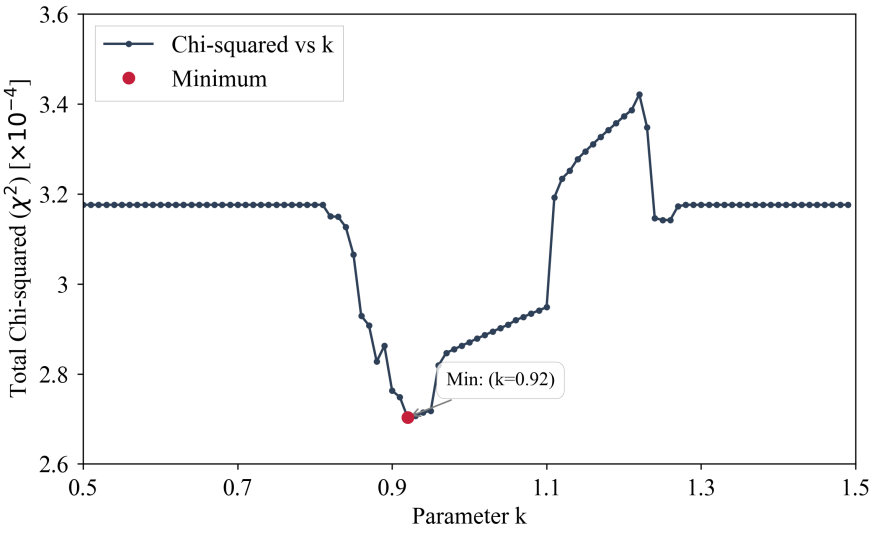

Figure 21: The value of the chi-squared as a function of the k value

The fitting process was then performed setting the parameter κ to the value found and then fitting Eq. (2.39) to the data (as shown in Fig. 16), and the distributions of

ε and ρ are reported, respectively, in Figs. 22 and 23. It was decided to model both distributions with uniform distributions. The mean value of the ε was found to be 3.66×10^{-24}, with a standard deviation of 0.26×10^{-24}; the mean value of the ρ parameter was found to be 210.4 with a standard deviation of 15.2.

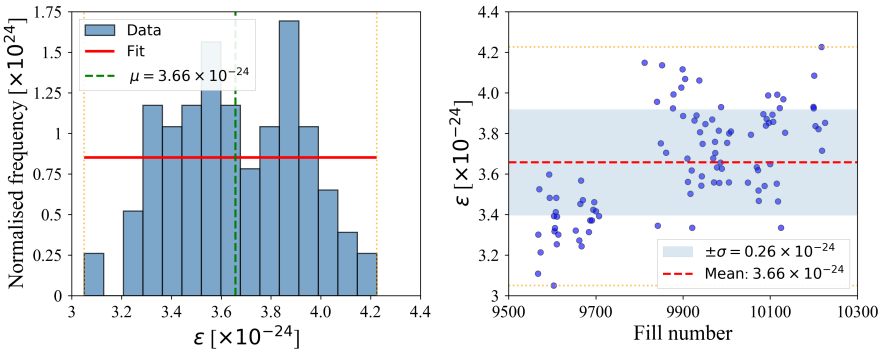

Figure 22: on the left, the distribution of the ε parameter, on the right, ε as a function of fill number

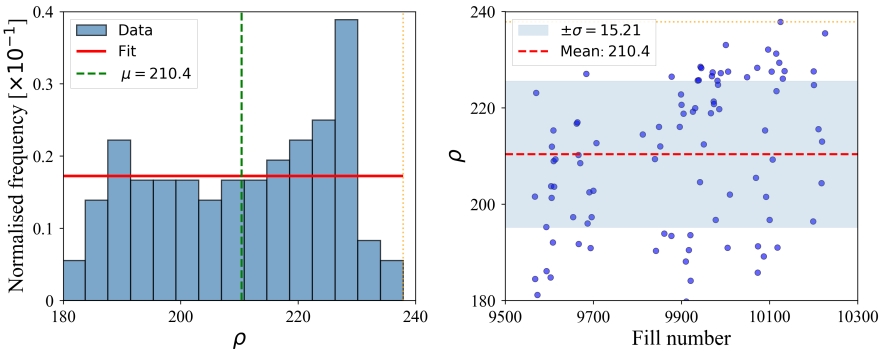

Figure 23: on the left, the distribution of the ρ parameter, on the right, ρ as a function of fill number

The analysis of the LHC 2024 run was completed with the evaluation of the turnaround time (t_{ta}) distribution, and the distribution of the time between failure (TBF). In particular, the t_{ta} distribution was found to be a decaying exponential, namely

$$\rho(t_{\mathrm{ta}}) = \mu_{\mathrm{ta}} e^{-\mu_{\mathrm{ta}} t_{\mathrm{ta}}}\,, \tag{3.1}$$

with mean value $\langle t_{\mathrm{ta}} \rangle = 1/\mu_{\mathrm{ta}} = 2.52\,\mathrm{h}$, as shown in Fig. 24

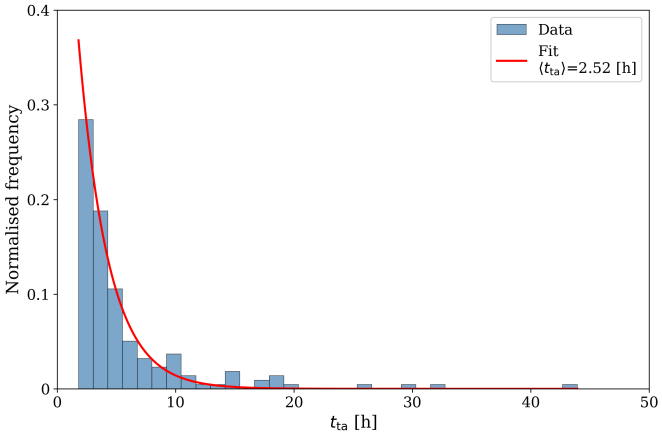

Figure 24: t_{ta} distribution for 2024

The TBF distribution was instead found to be a Weibull distribution,namely

$$\rho(t_{\mathrm{fail}}) = \mu_{\mathrm{f}}\kappa(\mu_{\mathrm{f}}t_{\mathrm{fail}})^{\kappa-1}e^{-(\mu_{\mathrm{f}}t_{\mathrm{fail}})^{\kappa}}\,, \tag{3.2}$$

as reported in Fig. 25, described by parameters $\langle\mathrm{MTBF}\rangle = 1/\mu_{\mathrm{f}} = 12.69\,\mathrm{h}$ and $\kappa = 1.06$.

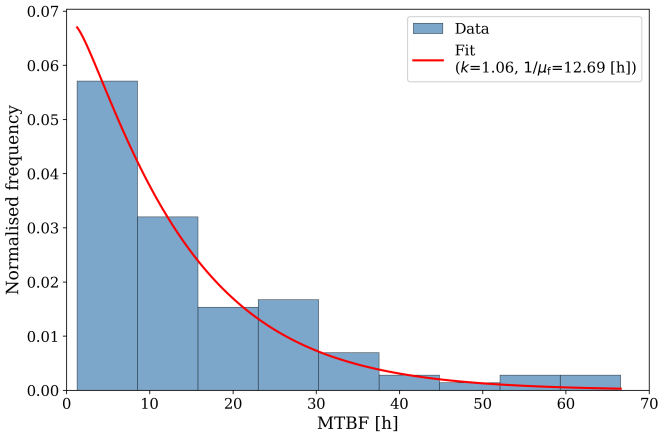

Figure 25: Distribution of MTBF

All the values discussed up to now are summarised in table 1, but the values of β^*, which is an external parameter set by the operators, which does not fluctuate statistically. Some other features of the 2024 fills are reported in 7, but they will not be used for the Monte Carlo simulation.

In 7, a table is reported that recaptures all the values for the data analysis of the three years of Run 3.

Table 1: Statistical analysis of each parameter for year 2024

Parameter	Mean	Standard deviation
L_ℓ [$\mu b^{-1}Hz$]	19945	575
t_{dec} [h]	5.75	2.26
N_i [p]	3.75×10^{14}	0.067×10^{14}
ε	3.66×10^{-24}	0.26×10^{-24}
ρ	210	15
t_{ta} [h]	2.52	0.18
MTBF [h]	12.69	1.24

An additional analysis required for the Monte Carlo simulation was the correlation between the chosen parameters. The correlation matrix generated for the Monte Carlo simulation is described in 5 . In Fig. 26, all the correlations studied and their values are reported.

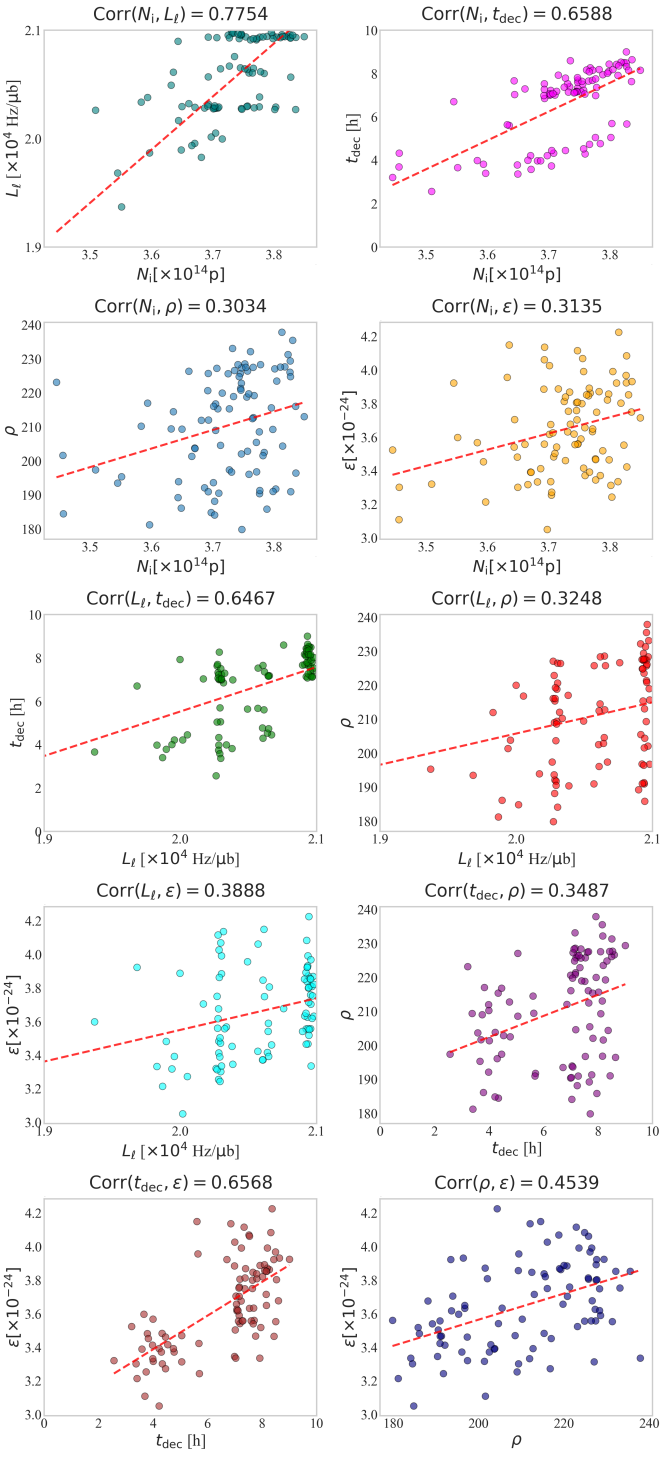

Figure 26: Plots of correlations for year 2024

4 Optimisation strategy

Maximising the number of recorded physics events is a fundamental goal in collider experiments looking for new physics. Although detector and data acquisition upgrades can increase event rates, the most direct approach to accumulating more events is to maximise the integrated luminosity delivered to the experiments. Integrated luminosity optimisation schemes are therefore essential for achieving experimental objectives.

Recent work by Capoani et al. [43] has demonstrated the potential of such optimisation strategies for LHC Run 2, providing encouraging results that warrant further investigation. A natural extension of this approach is the development and implementation of optimisation schemes specifically tailored for luminosity levelling operations. Such developments would benefit not only the final year of LHC operation, but also provide valuable insights for the upcoming High-Luminosity LHC (HL-LHC) upgrade, where levelling techniques will play a central role in luminosity delivery.

Having defined the data that will be used to test the optimisation scheme, one of the cores of this work lies on the definition of the optimisation scheme. In particular, different approaches have been evaluated, trying to generalise the model to be applied and considering problems rising from the functioning of the machine.

4.1 The simplest case

The integrated luminosity in the presence of luminosity levelling reads as

$$\mathcal{L}(t_\ell, t_{\mathrm{dec}}) = L_\ell t_\ell + \int_0^{t_{\mathrm{dec}}} dt L(t)\,, \tag{4.1}$$

where L_ℓ represents the levelled luminosity value, t_ℓ the levelling time, strictly related to L_ℓ according to Eq. (2.51), t_{dec} the luminosity $L(t)$ decay interval. The levelling part and the decay part are treated separately as independent, taking into account that relations shown in Eqs. (2.50) and (2.51) define the crossing from one regime to the next. The first step to be considered in the maximisation process is the pure deterministic one, considering then L_ℓ (and consequently t_ℓ) a given parameter. The equation to be maximised is

$$\mathcal{L}_{\mathrm{tot}}(t_{\mathrm{fill}}) = N_{\mathrm{fill}}\mathcal{L}(t_\ell, t_{\mathrm{dec}}) = \frac{T + t_{\mathrm{ta}}}{t_{\mathrm{ta}} + t_\ell + t_{\mathrm{dec}}} \left(L_\ell t_\ell + \int_0^{t_{\mathrm{dec}}} dt L(t) \right)\,, \tag{4.2}$$

where N_{fill} represents the total number of fills produced during time T, total time for physics, and t_{ta} represents the turn-around time, time, the total time required to prepare the accelerator for a new collision run, or “fill”, after the previous one has ended, comprehending different steps (beam dump, preparation, injection, ramping, squeeze

and alignment, stability checks). Under these assumptions, the optimisation is performed by evaluating the expression

$$\frac{d\mathcal{L}_{\mathrm{tot}}}{dt_{\mathrm{dec}}} = 0\,. \tag{4.3}$$

Using the calculations of [43] for pure burn-off and beams of equal intensity, the optimal fill time t_{dec} is the solution of the equation

$$\varepsilon N_i \left[1 + \left(1 - \sqrt{\frac{L_\ell}{\hat{L}}}\right) t_{\mathrm{dec}}^2 + 2\sqrt{\frac{\hat{L}}{L_\ell}}\left(1 - \sqrt{\frac{L_\ell}{\hat{L}}}\right)\right] - t_{\mathrm{ta}} = 0\,. \tag{4.4}$$

The Equation (4.4) allows for two real solutions of opposite signs and at least for one real and positive solution. Solutions for the optimal decay part are given by

$$\hat{t}_{\mathrm{dec}} = \frac{-\sqrt{\frac{\hat{L}}{L_\ell}}\left(1 - \sqrt{\frac{L_\ell}{\hat{L}}}\right) \pm \sqrt{\frac{\hat{L}}{L_\ell}\left(1 - \sqrt{\frac{L_\ell}{\hat{L}}}\right)^2 + \varepsilon N_{\mathrm{i}} t_{\mathrm{ta}}\left[1 + \left(1 - \sqrt{\frac{L_\ell}{\hat{L}}}\right)\right]}}{\varepsilon N_{\mathrm{i}}\left[1 + \left(1 - \sqrt{\frac{L_\ell}{\hat{L}}}\right)\right]}\,. \tag{4.5}$$

It is evident how taking $L_\ell = \hat{L}$ and $t_\ell = 0$, so no levelling, the solutions are those found in [43] for the LHC Run 2 case. The solutions of Eq. (4.5) have been evaluated, and plots of them are reported here. In particular, these simulations have been obtained using $T = 3121\,\mathrm{h}$, $\varepsilon = 3.6 \times 10^{-24}$, $\hat{L} = 2.691 \times 10^{38}\,\mathrm{m^{-2}\,Hz}$, $N_i = 3.5 \times 10^{14}\,\mathrm{p}$, $t_{\mathrm{ta}} = 3\,\mathrm{h}$. In particular, it should be noted that the optimisation procedure exhibits a tendency to extend the decay time proportionally to the ratio $L_\ell/\hat{L}$, whilst simultaneously increasing $\hat{t}_{\mathrm{dec}}$ in response to higher turnaround time values (see Fig. 4.1). A remarkable observation emerges when considering the total fill time, defined as the sum of the optimised decay time $\hat{t}_{\mathrm{dec}}$ and the levelling time t_ℓ (computed using Eq. (2.51)). The solution exhibits singular behaviour below a critical threshold of the ratio $L_\ell/\hat{L}$, whereby the total time diverges. This divergence can be attributed to the levelling time that assumes substantially large values in the regime of intensive levelling schemes, characterised by $L_\ell \ll \hat{L}$ (see 4.1).

The evaluation of the optimisation procedure is completed by analysing the total integrated luminosity obtained through this scheme and the behaviour of the instantaneous luminosity, both the levelled value L_ℓ and the virtual value $\hat{L}$, at the end of the fill. The total integrated luminosity, computed over the physics time T during Run 3 and plotted as a function of the levelling ratio $L_\ell/\hat{L}$, exhibits a monotonic increase as the levelling ratio approaches unity. This behaviour indicates that more intensive levelling schemes impose a constraint on the maximum achievable integrated luminosity, thereby suggesting that minimisation of the levelling procedure is beneficial for luminosity accumulation.

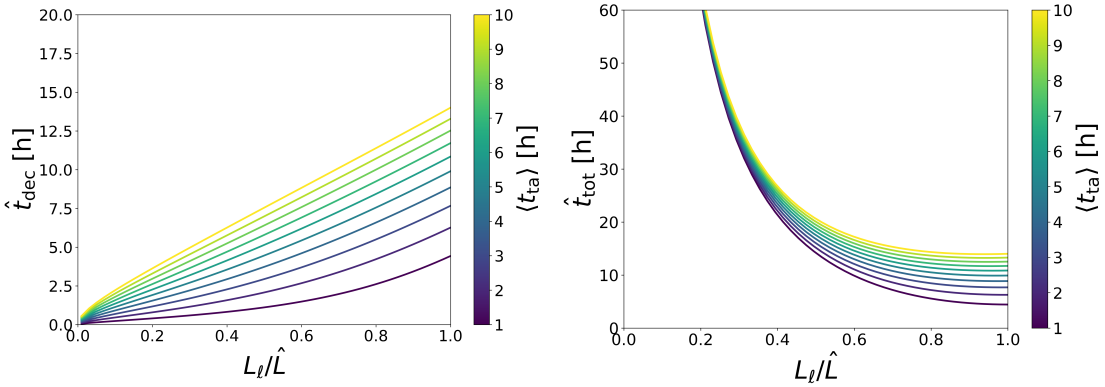

Figure 27: On the left, solutions of Eq. (4.5); on the right, solutions of Eq. (4.5) summed with the t_ℓ calculated for each $L_\ell/\hat{L}$

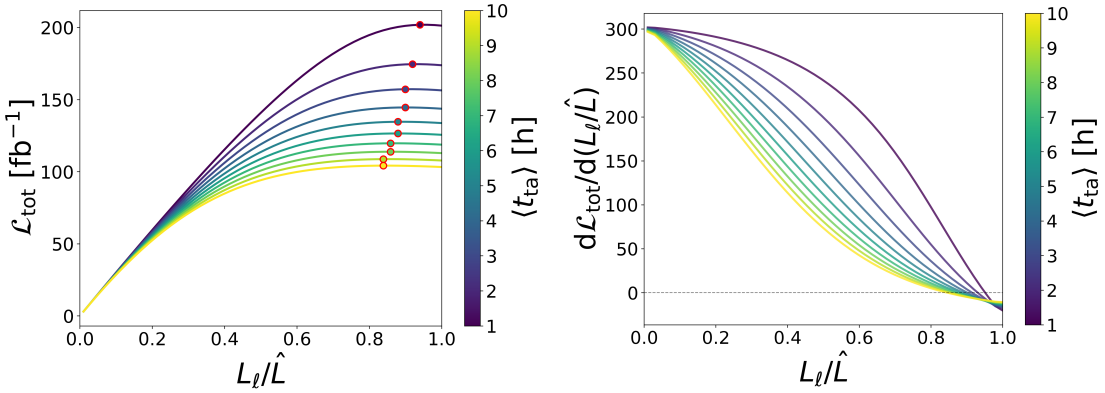

Figure 28: On the right, the behaviour of the optimised $\mathcal{L}_{\text{tot}}$ with respect to the ratio $L_\ell/\hat{L}$, with the maximum values circled in red; on the left, the derivative of the $\mathcal{L}_{\text{tot}}$

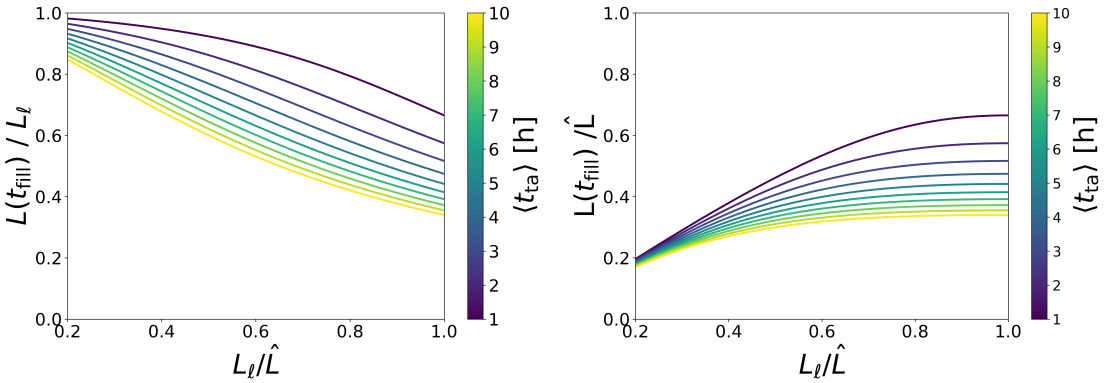

Figure 29: On the left, the behaviour of the ratio of $L(t_{\text{fill}})/L_\ell$ with respect to the ratio $L_\ell/\hat{L}$; on the right, the behaviour of $L(t_{\text{fill}})/\hat{L}$ with respect to the ratio $L_\ell/\hat{L}$

4.2 Two-parameter model

It is essential to note that the model presented in Eq. (4.2) has an intrinsic limitation. In fact, the turnaround time cannot be considered fixed, as it varies from fill to fill. The model in Eq. (4.2) represents just an indicative behaviour of the system, but cannot be taken as the final one to be used for the optimisation process.

Then a new model should be introduced, modifying, for the levelling case, the one proposed in [43]. In particular, the global function to be optimised turns out to be

$$\begin{aligned}\mathcal{L}_{\mathrm{tot}}(L_\ell, t_{\mathrm{dec,c}}, t_{\mathrm{dec,f}}) = &\sum_{j=1}^{i-1} \mathcal{L}_{\mathrm{int}}(L_l, \hat{t}_{\mathrm{dec},j}) + L_{\ell,\mathrm{c}} t_{\ell,\mathrm{c}} + \int_0^{t_{\mathrm{dec,c}}} L(t)\, dt \\ &+ \frac{T - \left[\sum_{j=1}^{i-1}(t_{\mathrm{ta},j} + \hat{t}_{\mathrm{dec},j} + t_{\ell,j}) + t_{\mathrm{ta},i} + t_{\ell,\mathrm{c}} + t_{\mathrm{dec,c}}\right]}{\frac{1}{i}\sum_{j=1}^{i} t_{\mathrm{ta},j} + t_{\ell,\mathrm{f}} + t_{\mathrm{dec,f}}} \\ &\times \left(L_\ell t_{\ell,\mathrm{f}} + \int_0^{t_{\mathrm{dec,f}}} L_{\mathrm{mp}}(t)\, dt\right) \\ = &\sum_{j=1}^{i-1} \mathcal{L}_{\mathrm{int}}(L_\ell, \hat{t}_{\mathrm{dec},j}) + \mathcal{L}_{\mathrm{c}}(L_\ell, t_{\mathrm{dec,c}}) + \mathcal{L}_{\mathrm{f}}(L_\ell, t_{\mathrm{dec,c}}, t_{\mathrm{dec,f}})\,,\end{aligned} \tag{4.6}$$

where the three terms of the sum refer, respectively, to the past $i-1$ fills, to the current fill, the i-th one, and to the future fill. $t_{\mathrm{ta},j}$ ($1 \leq j \leq i$) and $\hat{t}_{\mathrm{dec},j}$ ($1 \leq j \leq i-1$), represent, respectively, the optimal turnaround and fill-decay times for all fills from 1 to i. For fills 1 to $i-1$, $\mathcal{L}_{\mathrm{int}}$ represents the integrated luminosity of a single fill, including also the levelling part. The fill i is the current one, associated with the integrated luminosity $\mathcal{L}_{\mathrm{c}}$. The model also includes an estimate of the integrated luminosity collected in future fills, which is globally indicated as $\mathcal{L}_{\mathrm{f}}$ and built using estimates of future fills. $L_{\mathrm{mp}}(t)$ represents the most probable value of the function representing the evolution of the luminosity after levelling. When the luminosity function is Gaussian distributed, the most probable value corresponds to the average value. It is clear that the knowledge about this function comes, when data are available, from the past fills. The value of $t_{\ell,\mathrm{f}}$ is defined through the most probable value of $\hat{L}$. With respect to the model discussed in Eq. (4.2), the one presented in Eq. (4.6) introduces one additional parameter to be optimised, $t_{\mathrm{dec,f}}$, representing the optimal fill-decay time for all future fills: the third term in Eq. (4.6) introduces a relationship between $t_{\mathrm{dec,c}}$ and $t_{\mathrm{dec,f}}$. Furthermore, Eq. (4.6) assumes that the target value of the levelled luminosity is constant for all fills and is defined as a parameter not to be optimised. As a consequence, the values of the levelling time for future and current fills, $t_{\ell,\mathrm{f}}$ and $t_{\ell,\mathrm{c}}$, are generally different. The optimisation strategy focusses on $t_{\mathrm{dec,c}}$ and $t_{\mathrm{dec,f}}$ as free parameters, determining the

values that set the gradient of $\mathcal{L}_{\rm tot}$ to zero, namely,

$$\begin{cases} \frac{\partial \mathcal{L}_{\rm tot}}{\partial t_{\rm dec,c}} = L(t_{\rm dec,c}) - \frac{1}{\langle t_{\rm ta}\rangle + t_{\ell,\rm f} + t_{\rm dec,f}} \left(L_\ell t_{\ell,\rm f} + \int_0^{t_{\rm dec,f}} dt L_{\rm mp}(t) \right) = 0 \\ \frac{\partial \mathcal{L}_{\rm tot}}{\partial t_{\rm dec,f}} = L_{\rm mp}(t_{\rm dec,f}) - \frac{1}{\langle t_{\rm ta}\rangle + t_{\ell,\rm f} + t_{\rm dec,f}} \left(L_\ell t_{\ell,\rm f} + \int_0^{t_{\rm dec,f}} dt L_{\rm mp}(t) \right) = 0 \end{cases} \tag{4.7}$$

which gives

$$\begin{cases} L(\hat{t}_{\rm dec,c}) = L_{\rm mp}(\hat{t}_{\rm dec,f}) \\ L_{\rm mp}(\hat{t}_{\rm dec,f}) = \frac{1}{\langle t_{\rm ta}\rangle + t_{\ell,\rm f} + \hat{t}_{\rm dec,f}} \left(L_\ell t_{\ell,\rm f} + \int_0^{\hat{t}_{\rm dec,f}} dt L_{\rm mp}(t) \right) \end{cases} \tag{4.8}$$

The second equation is used to determine the optimal fill decay-time value for future fills, $\hat{t}_{\rm dec,f}$, and the first to determine $t_{\rm dec,c}$. It is evident how the optimisation scheme takes into consideration only the levelling parameters of the future fills, which are critically dependent on $L_{\rm mp}(t)$, the maximum luminosity corresponding to the parameters for the most probable luminosity. The system of equations (4.8) is conceptually similar to the one derived in [43], even though here the levelling process has been included. The system of equations (4.8) can be solved analytically. Setting $\varepsilon = \sigma_{\rm int} n_{\rm c} \Xi_{\rm max} = \sigma_{\rm int} n_{\rm c} \frac{\hat{L}}{N_{\rm i}^2}$ and $\alpha = N_{\rm i}/N_{\rm mp}$ as a description of the relationship between the current fill and the most probable one, the model to describe the evolution of the instantaneous luminosity would be

$$L(t) = L_{\rm mp} = \frac{\Xi_{\rm max} N_{\rm mp}^2 (1-\rho_{\ell,\rm mp})^2}{[1+\varepsilon N_{\rm mp}(1-\rho_{\ell,\rm mp})t]^2}\,, \tag{4.9}$$

where

$$\rho_{\ell,\rm mp} = 1 - \sqrt{\frac{L_\ell}{\hat{L}_{\rm mp}}} = 1 - \alpha \sqrt{\frac{L_\ell}{\hat{L}}}\,, \tag{4.10}$$

taking into account the levelling process previously applied at a value L_ℓ with respect to the virtual maximum level $\hat{L}$. The first equation of (4.8) implies $\hat{t}_{\rm dec,c} = \hat{t}_{\rm dec,f}$ and $\hat{t}_{\rm dec,f}$ is a solution of quadratic equation

$$a\hat{t}_{\rm dec,f}^2 + b\hat{t}_{\rm dec,f} + c = 0\,, \tag{4.11}$$

where

$$a = \frac{\varepsilon N_{\mathrm{i}}}{\alpha} \tag{4.12}$$

$$b = -\frac{2}{\alpha}\left(\sqrt{\frac{L_\ell}{\hat{L}}} - \alpha\frac{L_\ell}{\hat{L}}\right) \tag{4.13}$$

$$c = \langle t_{\mathrm{ta}} \rangle \, . \tag{4.14}$$

It is evident that, assuming $L_\ell = \hat{L}$, the coefficients of Eq. (4.11) reduce to the form analysed in [43]. Regarding 4.1, a qualitative analysis of the optimisation path has been given. In particular, plots of the behaviour of the three free parameters $\left(\langle t_{\mathrm{ta}} \rangle \, , \frac{L_\ell}{\hat{L}}, \frac{N_{\mathrm{i}}}{N_{\mathrm{mp}}}\right)$ have been created. In Fig. 30 the different behaviours of the optimisation are plotted as a function of the parameter α for different cases of $L_\ell/\hat{L}$. The logic is quite clear: the optimiser tends to increase the value of t_{dec} whenever the intensity is low ($N_{\mathrm{mp}} < N_i$ for $\alpha > 1$). Furthermore, the optimiser tends to increase the decay part as the ratio $L_\ell/\hat{L}$ increases and the levelling is less strong. In Fig. 31 the behaviour has been plotted as a function of the ratio $L_\ell/\hat{L}$ for different values of $\langle t_{\mathrm{ta}} \rangle$. It is evident how the optimiser tends to increase the t_{dec} value whenever both the ratio $L_\ell/\hat{L}$ and the α values increase. In Fig. 32 the behaviour has been studied considering the optimal $\hat{t}_{\mathrm{dec}}$ with respect to the ratio $L_\ell/\hat{L}$ for different α values. It is instructive to note that the case for $\alpha = 1$ is the same as studied for 4.1. The optimiser tends to increase the decay part for increasing $L_\ell/\hat{L}$, increasing α and increasing $\langle t_{\mathrm{ta}} \rangle$

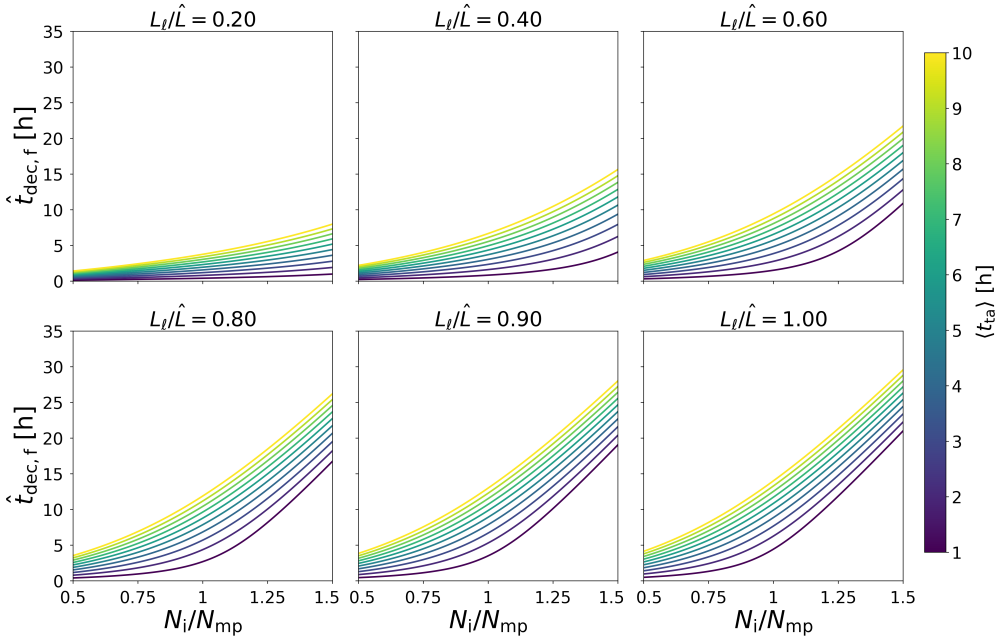

Figure 30: In the plot, the optimal $\hat{t}_{\mathrm{dec,f}}$ has been plot as a function of the α parameter for different values of the ratio $L_\ell/\hat{L}$; simulation run using $\varepsilon = 3.66 \times 10^{-24}$

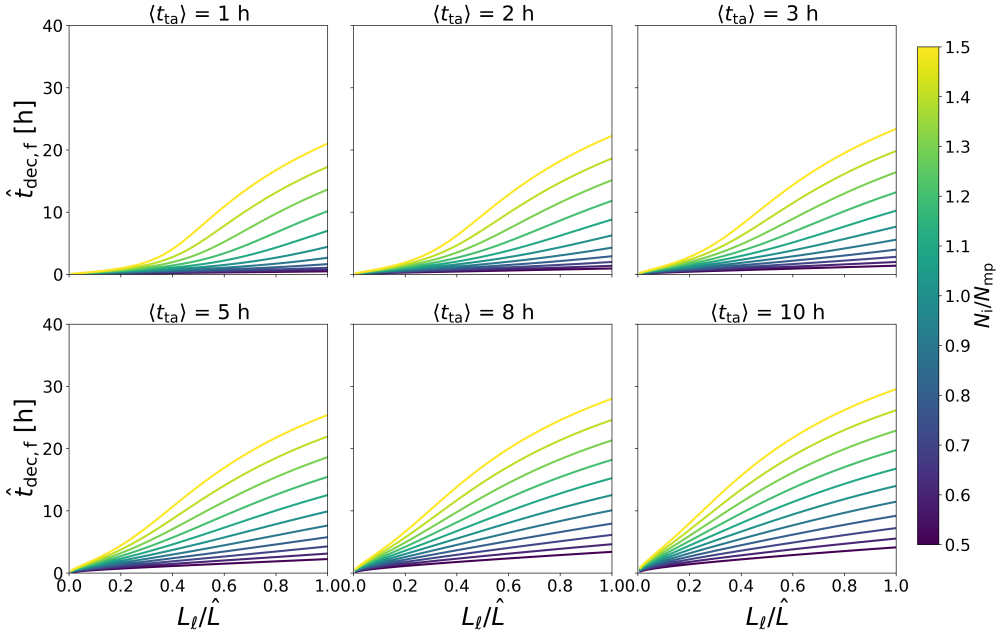

Figure 31: In the plot, the optimal $\hat{t}_{\mathrm{dec,f}}$ has been plot as a function of the ratio $L_\ell/\hat{L}$ for different values of the t_ta; simulation run using $\varepsilon = 3.66 \times 10^{-24}$

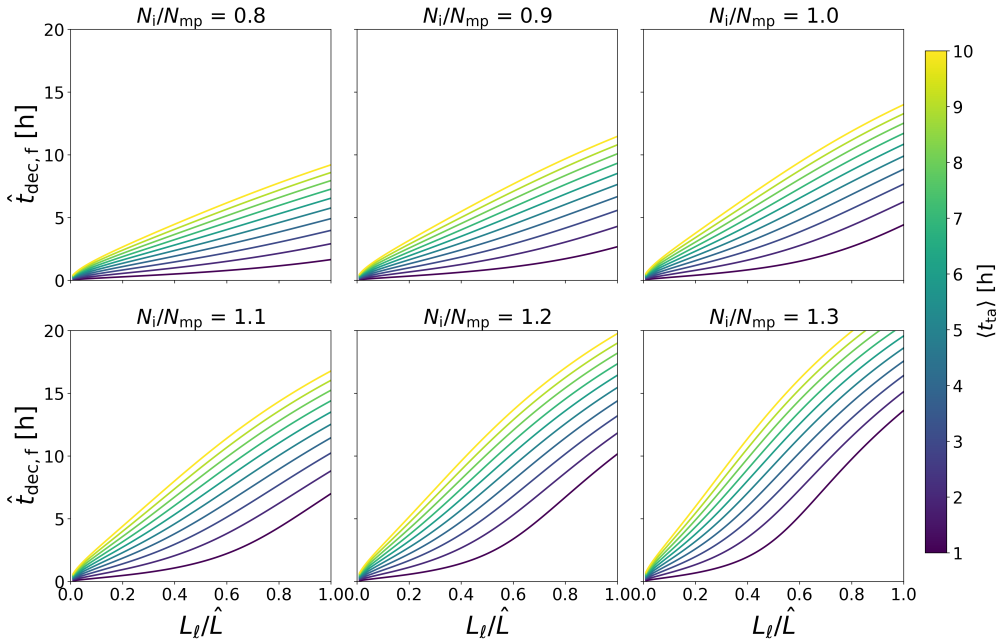

Figure 32: In the plot, the optimal $\hat{t}_{\mathrm{dec,f}}$ has been plot as a function of the ratio $L_\ell/\hat{L}$ for different values of the α; simulation run using $\varepsilon = 3.66 \times 10^{-24}$

4.3 Four-parameter model

The optimisation procedure discussed up to this point considers only $t_{\mathrm{dec,c}}$ and $t_{\mathrm{dec,f}}$ as parameters to be optimised. Therefore, it is possible to also include two additional parameters in the scheme: the levelled luminosity value, namely $L_{\ell,\mathrm{f}}$ and $L_{\ell,\mathrm{c}}$. This implies that two additional derivatives must be taken into consideration:

$$\begin{cases} \frac{\partial \mathcal{L}_{tot}}{\partial L_{\ell,\mathrm{c}}} = t_{\ell,\mathrm{c}} + L_{\ell,\mathrm{c}} \frac{\partial t_{\ell,\mathrm{c}}}{\partial L_{\ell,\mathrm{c}}} - \frac{\partial t_{\ell,\mathrm{c}}}{\partial L_{\ell,\mathrm{c}}} \frac{1}{\langle t_{\mathrm{ta}} \rangle + t_{\ell,\mathrm{f}} + t_{\mathrm{dec,f}}} \left(L_{\ell,\mathrm{f}} t_{\ell,\mathrm{f}} + \int_0^{t_{\mathrm{dec,f}}} dt L_{\mathrm{mp}}(t) \right) = 0 \\ \frac{\partial \mathcal{L}_{\mathrm{tot}}}{\partial L_{\ell,\mathrm{f}}} = t_{\ell,\mathrm{f}} + L_{\ell,\mathrm{f}} \frac{\partial t_{\ell,\mathrm{f}}}{\partial L_{\ell,\mathrm{f}}} - \frac{\partial t_{\ell,\mathrm{c}}}{\partial L_{\ell,\mathrm{c}}} \frac{1}{\langle t_{\mathrm{ta}} \rangle + t_{\ell,\mathrm{f}} + t_{\mathrm{dec,f}}} \left(L_{\ell,\mathrm{f}} t_{\ell,\mathrm{f}} + \int_0^{t_{\mathrm{dec,f}}} dt L_{\mathrm{mp}}(t) \right) = 0 \,. \end{cases} \tag{4.15}$$

The complete set of equations to be solved reads

$$\begin{cases} \frac{\partial \mathcal{L}_{tot}}{\partial t_{\mathrm{dec,c}}} = L(t_{\mathrm{dec,c}}) - \frac{1}{\langle t_{\mathrm{ta}} \rangle + t_{\ell,\mathrm{f}} + t_{\mathrm{dec,f}}} \left(L_\ell t_{\ell,\mathrm{f}} + \int_0^{t_{\mathrm{dec,f}}} dt L_{\mathrm{mp}}(t) \right) = 0 \\ \frac{\partial \mathcal{L}_{\mathrm{tot}}}{\partial t_{\mathrm{dec,f}}} = L_{\mathrm{mp}}(t_{\mathrm{dec,f}}) - \frac{1}{\langle t_{\mathrm{ta}} \rangle + t_{\ell,\mathrm{f}} + t_{\mathrm{dec,f}}} \left(L_\ell t_{\ell,\mathrm{f}} + \int_0^{t_{\mathrm{dec,f}}} dt L_{\mathrm{mp}}(t) \right) = 0 \\ \frac{\partial \mathcal{L}_{\mathrm{tot}}}{\partial L_{\ell,\mathrm{c}}} = t_{\ell,\mathrm{c}} + L_{\ell,\mathrm{c}} \frac{\partial t_{\ell,\mathrm{c}}}{\partial L_{\ell,\mathrm{c}}} - \frac{\partial t_{\ell,\mathrm{c}}}{\partial L_{\ell,\mathrm{c}}} \frac{1}{\langle t_{\mathrm{ta}} \rangle + t_{\ell,\mathrm{f}} + t_{\mathrm{dec,f}}} \left(L_{\ell,\mathrm{f}} t_{\ell,\mathrm{f}} + \int_0^{t_{\mathrm{dec,f}}} dt L_{\mathrm{mp}}(t) \right) = 0 \\ \frac{\partial \mathcal{L}_{\mathrm{tot}}}{\partial L_{\ell,\mathrm{f}}} = t_{\ell,\mathrm{f}} + L_{\ell,\mathrm{f}} \frac{\partial t_{\ell,\mathrm{f}}}{\partial L_{\ell,\mathrm{f}}} - \frac{\partial t_{\ell,\mathrm{c}}}{\partial L_{\ell,\mathrm{c}}} \frac{1}{\langle t_{\mathrm{ta}} \rangle + t_{\ell,\mathrm{f}} + t_{\mathrm{dec,f}}} \left(L_{\ell,\mathrm{f}} t_{\ell,\mathrm{f}} + \int_0^{t_{\mathrm{dec,f}}} dt L_{\mathrm{mp}}(t) \right) = 0 \,. \end{cases} \tag{4.16}$$

The system above can be cast in the following form

$$\begin{cases} L(t_{\mathrm{dec,c}}) = L_{\mathrm{mp}}(t_{\mathrm{dec,f}}) \\ L_{\mathrm{mp}}(t_{\mathrm{dec,f}}) = \frac{1}{\langle t_{\mathrm{ta}} \rangle + t_{\ell,\mathrm{f}} + t_{\mathrm{dec,f}}} \left(L_\ell t_{\ell,\mathrm{f}} + \int_0^{t_{\mathrm{dec,f}}} dt L_{\mathrm{mp}}(t) \right) \\ L_{\ell,\mathrm{c}}^{3/2} + L_{\ell,\mathrm{c}}^{1/2} L(t_{\mathrm{dec,c}}) - 2L(t_{\mathrm{dec,c}}) \hat{L}^{1/2} = 0 \\ L_{\ell,\mathrm{f}}^{3/2} + L_{\ell,\mathrm{f}}^{1/2} L(t_{\mathrm{dec,f}}) - 2L(t_{\mathrm{dec,f}}) \hat{L}^{1/2} = 0 \,. \end{cases} \tag{4.17}$$

The depressed cubic equations of (4.17) have a single positive solution. In particular, from the fourth equation of the system, one can determine the optimal value for $L_{\ell,\mathrm{f}}$ as a function of $L_{\mathrm{mp}}(t_{\mathrm{dec,f}})$, from which the value $t_{\ell,\mathrm{f}}$ can be derived. The value obtained can be substituted in the second equation, in order to compute the optimal decay-fill time $\hat{t}_{\mathrm{dec,f}}$. The first equation is used to evaluate the optimal time $\hat{t}_{\mathrm{dec,c}}$. As a last step, the optimised result should be replaced in the last two equations to determine the actual values of the levelled luminosity for the current and future fills. In this case, analytical solutions are extremely difficult to evaluate, making numerical methods the most suitable approach to be chosen. Also for this optimisation model, a plot has been created (see Fig. 33), which is numerically solved for (4.17). The behaviour of the optimisation parameters has been considered with respect to the values of α and t_{ta}.

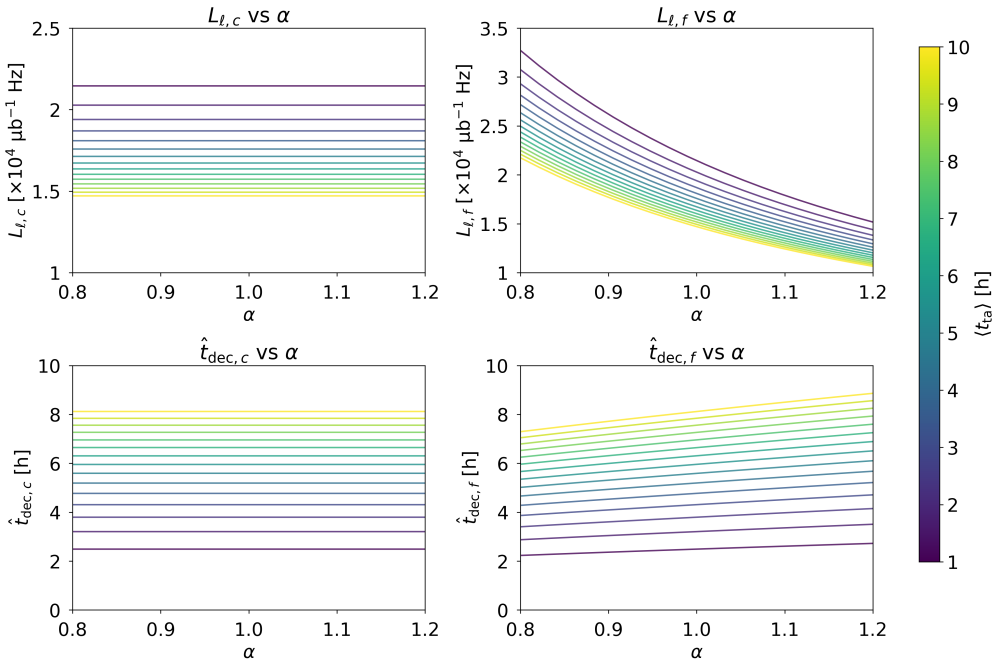

Figure 33: The behaviour of each optimisation parameter has been plotted with respect to the α value for different $\langle t_{\mathrm{ta}} \rangle$ values; simulation run using $\varepsilon = 3.66 \times 10^{-24}$

4.4 Failure probability

In the optimisation process described in sections 4.2 and 4.3 the failure probability of a fill has never been taken into account. An efficient optimisation strategy should also take this aspect into account. Assume $f(t)$ to be the probability of failure of a fill between t and $t + dt$ and $F(t)$ the probability of failure before t. As a consequence, $S(t) = 1 - F(t)$ is the survival probability. If t is the time at which a fill should be terminated, then the expected fill time would be

$$t_{\mathrm{e}}(t) = \int_0^\infty d\tau \tilde{t}(\tau)\,, \tag{4.18}$$

where the function $\tilde{t}(\tau)$ is defined as

$$\tilde{t}(\tau) = \begin{cases} \tau & \text{if } \tau < t \\ t & \text{if } \tau \geq t\,. \end{cases} \tag{4.19}$$

This means that the typical duration of a fill may be defined as

$$t_{\mathrm{e}}(t) = \int_0^t d\tau \tau f(\tau) + t \int_t^\infty d\tau f(\tau) \tag{4.20}$$

$$= tF(t) - \int_0^t d\tau F(\tau) \quad + t(1 - F(t)) \tag{4.21}$$

$$= \int_0^t d\tau \;\; S(\tau)\,. \tag{4.22}$$

This allows for the redefinition of the expected luminosity as

$$\mathcal{L}_e(t) = \int_0^t d\tau L(\tau) f(\tau) + L(t) \int_t^\infty d\tau f(\tau) = \int_0^t d\tau \;\; L(\tau) S(\tau)\,. \tag{4.23}$$

The function to be optimised becomes

$$\mathcal{L}_{\mathrm{c}}(L_{\ell,\mathrm{c}} t_{\mathrm{dec,c}}) = L_{\ell,\mathrm{c}} \int_0^{t_{\ell,\mathrm{c}}} d\tau S(\tau) + \int_0^{t_{\mathrm{dec,c}}} d\tau L(\tau) S(\tau + t_\ell, \mathrm{c}) \tag{4.24}$$

$$\mathcal{L}_{\mathrm{f}}(L_{\ell,\mathrm{f}}, t_{\mathrm{dec,c}}, t_{\mathrm{dec,f}}) = \frac{T - \left[\sum_{j=1}^{i-1} (t_{\mathrm{ta},j} + \hat{t}_{\mathrm{dec},j}) + t_{\mathrm{ta},i} + \int_0^{t_{\ell,\mathrm{c}}} d\tau\, S(\tau) + \int_0^{t_{\mathrm{dec,c}}} d\tau\, S(\tau + t_{\ell,\mathrm{c}})\right]}{\frac{1}{i}\sum_{j=1}^{i} t_{\mathrm{ta},j} + \int_0^{t_{\ell,\mathrm{f}}} d\tau\, S(\tau) + \int_0^{t_{\mathrm{dec,f}}} d\tau\, S(\tau + t_{\ell,\mathrm{f}})} \times \left(L_{\ell,\mathrm{f}} \int_0^{t_{\ell,\mathrm{f}}} d\tau\, S(\tau) + \int_0^{t_{\mathrm{dec,f}}} d\tau\, L_{\mathrm{mp}}(\tau) S(\tau + t_{\ell,\mathrm{f}}) \right)\,. \tag{4.25}$$

The optimisation of $\mathcal{L}_{\mathrm{c}} + \mathcal{L}_{\mathrm{f}}$, assuming only two optimisation parameters, gives the following equations

$$\begin{cases} L(t_{\mathrm{dec,c}}) = \dfrac{1}{\langle t_{\mathrm{ta}} \rangle + \int_0^{t_{\ell,\mathrm{f}}} d\tau\, S(\tau) + \int_0^{t_{\mathrm{dec,f}}} d\tau\, S(\tau + t_{\ell,\mathrm{f}})} \times \\ \qquad \times \left(L_\ell \int_0^{t_{\ell,\mathrm{f}}} d\tau\, S(\tau) + \int_0^{t_{\mathrm{dec,f}}} d\tau\, L_{\mathrm{mp}}(\tau) S(\tau + t_{\ell,\mathrm{f}}) \right) \\ L_{\mathrm{mp}}(t_{\mathrm{dec,f}}) = \dfrac{1}{\langle t_{\mathrm{ta}} \rangle + \int_0^{t_{\ell,\mathrm{f}}} d\tau\, S(\tau) + \int_0^{t_{\mathrm{dec,f}}} d\tau\, S(\tau + t_{\ell,\mathrm{f}})} \times \\ \qquad \times \left(L_\ell \int_0^{t_{\ell,\mathrm{f}}} d\tau\, S(\tau) + \int_0^{t_{\mathrm{dec,f}}} d\tau\, L_{\mathrm{mp}}(\tau) S(\tau + t_{\ell,\mathrm{f}}) \right)\,. \end{cases} \tag{4.26}$$

The result of the optimisation scheme proposed in (4.26) will be evaluated in the Monte Carlo simulation. In addition, the four-parameter optimisation model presented in (4.17) can be recast to include the failure probability, so that

$$
\begin{cases}
\dfrac{\partial \mathcal{L}_{\mathrm{tot}}}{\partial t_{\mathrm{dec,c}}} = L(t_{\mathrm{dec,c}}) - \dfrac{1}{\langle t_{\mathrm{ta}} \rangle + \displaystyle\int_0^{t_{\ell,\mathrm{f}}} d\tau\, S(\tau) + \int_0^{t_{\mathrm{dec,f}}} d\tau\, S(\tau + t_{\ell,\mathrm{f}})} \times \\
\qquad \times \left(L_{\ell,\mathrm{f}} \displaystyle\int_0^{t_{\ell,\mathrm{f}}} d\tau\, S(\tau) + \int_0^{t_{\mathrm{dec,f}}} d\tau\, L_{\mathrm{mp}}(\tau) S(\tau + t_{\ell,\mathrm{f}}) \right) = 0 \\
\dfrac{\partial \mathcal{L}_{\mathrm{tot}}}{\partial t_{\mathrm{dec,f}}} = L_{\mathrm{mp}}(t_{\mathrm{dec,f}}) - \dfrac{1}{\langle t_{\mathrm{ta}} \rangle + \displaystyle\int_0^{t_{\ell,\mathrm{f}}} d\tau\, S(\tau) + \int_0^{t_{\mathrm{dec,f}}} d\tau\, S(\tau + t_{\ell,\mathrm{f}})} \times \\
\qquad \times \left(L_{\ell,\mathrm{f}} \displaystyle\int_0^{t_{\ell,\mathrm{f}}} d\tau\, S(\tau) + \int_0^{t_{\mathrm{dec,f}}} d\tau\, L_{\mathrm{mp}}(\tau) S(\tau + t_{\ell,\mathrm{f}}) \right) = 0 \\
\dfrac{\partial \mathcal{L}_{\mathrm{tot}}}{\partial L_{\ell,\mathrm{c}}} = \displaystyle\int_0^{t_{\ell,\mathrm{c}}} d\tau\, S(\tau) + \frac{\partial t_{\ell,\mathrm{c}}}{\partial L_{\ell,\mathrm{c}}} \left[L_{\ell,\mathrm{c}} - \dfrac{1}{\langle t_{\mathrm{ta}} \rangle + \displaystyle\int_0^{t_{\ell,\mathrm{f}}} d\tau\, S(\tau) + \int_0^{t_{\mathrm{dec,f}}} d\tau\, S(\tau + t_{\ell,\mathrm{f}})} \times \right. \\
\qquad \left. \times \left(L_{\ell,\mathrm{f}} \displaystyle\int_0^{t_{\ell,\mathrm{f}}} d\tau\, S(\tau) + \int_0^{t_{\mathrm{dec,f}}} d\tau\, L_{\mathrm{mp}}(\tau) S(\tau + t_{\ell,\mathrm{f}}) \right) \right] = 0 \\
\dfrac{\partial \mathcal{L}_{\mathrm{tot}}}{\partial L_{\ell,\mathrm{f}}} = \displaystyle\int_0^{t_{\ell,\mathrm{f}}} d\tau\, S(\tau) + \frac{\partial t_{\ell,\mathrm{f}}}{\partial L_{\ell,\mathrm{f}}} \left[L_{\ell,\mathrm{f}} - \dfrac{1}{\langle t_{\mathrm{ta}} \rangle + \displaystyle\int_0^{t_{\ell,\mathrm{f}}} d\tau\, S(\tau) + \int_0^{t_{\mathrm{dec,f}}} d\tau\, S(\tau + t_{\ell,\mathrm{f}})} \times \right. \\
\qquad \left. \times \left(L_{\ell,\mathrm{f}} \displaystyle\int_0^{t_{\ell,\mathrm{f}}} d\tau\, S(\tau) + \int_0^{t_{\mathrm{dec,f}}} d\tau\, L_{\mathrm{mp}}(\tau) S(\tau + t_{\ell,\mathrm{f}}) \right) \right] = 0.
\end{cases}
\tag{4.27}
$$

The failure probability distribution is assumed to be a Weibull distribution, hypothesis supported also by the time between failure data analysis for LHC Run 3. In particular

$$
S(t) = \mu_{\mathrm{f}} k (\mu_{\mathrm{f}} t)^{k-1} e^{-(\mu_{\mathrm{f}} t)^k}\,, \tag{4.28}
$$

where μ_{f} is the inverse of the mean time between failures (MTBF). In particular, the failure rate scales with time as t^{k-1}, representing an ageing process. Another interesting analysis would be the strategy to deal with the last part of the Run, considering the

failure probability model. In particular, when the remaining time $t_{\mathrm{r}} \approx 2t_{\mathrm{fill}} + t_{\mathrm{ta}}$, the function to be optimised turns out to be

$$\begin{aligned}\mathcal{L}_{\mathrm{tot}}(t_{\mathrm{dec,c}}, t_\ell, l_{\mathrm{ta}}, L_{\ell,\mathrm{c}}, L_{\ell,\mathrm{f}}) = {} & L_{\ell,\mathrm{c}} t_e(t_{\ell,\mathrm{c}}) + \int_0^{t_{\mathrm{e}}(t_{\mathrm{dec,c}})} d\tau\, L(\tau) S(\tau + t_{\ell,\mathrm{c}}) \\ & + L_{\ell,\mathrm{f}} t_{\mathrm{e}}(t_{\ell,\mathrm{f}}) \\ & + \int_0^{t_{\mathrm{r}} - t_{\mathrm{ta}} - t_{\mathrm{e}}(t_{\ell,\mathrm{c}}) - t_{\mathrm{e}}(t_{\ell,\mathrm{f}}) - t_{\mathrm{e}}(t_{\mathrm{dec,c}})} d\tau\, L_{\mathrm{mp}}(\tau) S(\tau + t_{\ell,\mathrm{c}} + t_{\ell,\mathrm{f}})\,,\end{aligned} \tag{4.29}$$

where the optimisation parameters are $L_{\ell,\mathrm{c}}$, $L_{\ell,\mathrm{f}}$, $t_{\mathrm{dec,c}}$.

5 Monte Carlo evaluation

The best tool to evaluate the performance of the optimisation strategy analysed so far is represented by Monte Carlo simulation. This is a computational technique that employs repeated random sampling to obtain numerical results for complex systems, characterised by unavailable analytical solutions. The method is able to generate a large number of possible scenarios, each drawn from specified probability distributions, representing the system's uncertainty parameters. Through the analysis of the simulation results, it is possible to evaluate the probability distributions, expected values, and confidence intervals for the variables of interest. This approach has found a wide spectrum of applications in different fields, including quantitative finance, particle physics, and even risk analysis. However, some limitations of the method must be considered. The accuracy of estimates depends critically on the number of iterations performed, requiring a critical evaluation of the trade-off between computational cost and statistical precision [44, 45].

The core idea of the simulation implemented is to simulate a given large number of years of operations of the LHC machine, from 1×10^3 to 1×10^4. In this work, due to computational cost and time constraints, 1×10^3 years have been generated for each simulation. In the Monte Carlo framework, each fill is simulated generating each characterising parameter according to the parameters' distribution described in 3. The 2024 Run 3 parameters have been chosen, due to their stability and statistical consistency. It should be noted that the levelling time t_ℓ is not generated from a distribution, but is generated by using Eq. (2.51). The correlations between the parameters have also been included through the correlation matrix R, defined as

$$R = \begin{pmatrix} 1.00 & \mathrm{corr}(N_i, L_\ell) & \mathrm{corr}(N_i, t_{\mathrm{dec}}) & \mathrm{corr}(N_i, \rho) & \mathrm{corr}(N_i, \varepsilon) \\ \mathrm{corr}(N_i, L_\ell) & 1.00 & \mathrm{corr}(L_\ell, t_{\mathrm{dec}}) & \mathrm{corr}(L_\ell, \rho) & \mathrm{corr}(L_\ell, \varepsilon) \\ \mathrm{corr}(N_i, t_{\mathrm{dec}}) & \mathrm{corr}(L_\ell, t_{\mathrm{dec}}) & 1.00 & \mathrm{corr}(t_{\mathrm{dec}}, \rho) & \mathrm{corr}(t_{\mathrm{dec}}, \varepsilon) \\ \mathrm{corr}(N_i, \rho) & \mathrm{corr}(L_\ell, \rho) & \mathrm{corr}(t_{\mathrm{dec}}, \rho) & 1.00 & \mathrm{corr}(\rho, \varepsilon) \\ \mathrm{corr}(N_i, \varepsilon) & \mathrm{corr}(L_\ell, \varepsilon) & \mathrm{corr}(t_{\mathrm{dec}}, \varepsilon) & \mathrm{corr}(\rho, \varepsilon) & 1.00 \end{pmatrix}. \tag{5.1}$$

Each run is also defined by a maximum time, the physics time recorded in 2024, namely $2253.9\,\mathrm{h}$. For each simulated run, a pool of 1×10^3 eligible fills has been created. The fill pool feeds, at the same time and with the same fills, two "Run" generators: the basic Monte Carlo generator and the Optimised Monte Carlo generator. In the following, they will be referred to as *MC* and *Opt*, respectively. The Optimised generator is able to numerically solve the optimisation systems defined in 4.2 and 4.4. In particular, the optimisation framework tested is that described in Eqs. (4.6) and (4.26), respectively. This means that for each simulation performed, the optimisation parameters taken into account were the decay times $\hat{t}_{\mathrm{dec,c}}$ and $\hat{t}_{\mathrm{dec,f}}$. The latter was used to solve

the second equations of (4.6), to solve the first one and obtain the value of $\hat{t}_{\mathrm{dec,c}}$, which represents the best time to end the fill. The analysed optimisation framework allows for the selection, just for the optimised generator, of the values L_ℓ, called L_ℓ^* in this work and tested for each simulation, for the values $1.6 \times 10^4\,\mu\mathrm{b}^{-1}\mathrm{Hz}$, $1.8 \times 10^4\,\mu\mathrm{b}^{-1}\mathrm{Hz}$, $2.0 \times 10^4\,\mu\mathrm{b}^{-1}\mathrm{Hz}$, $2.2 \times 10^4\,\mu\mathrm{b}^{-1}\mathrm{Hz}$, $2.4 \times 10^4\,\mu\mathrm{b}^{-1}\mathrm{Hz}$, $2.6 \times 10^4\,\mu\mathrm{b}^{-1}\mathrm{Hz}$. Here, a first limitation of the implemented optimisation is evident: there will not be a direct comparison between unoptimised and optimised fills with the same L_ℓ, at least not for all the L_ℓ^* values scanned, as the unoptimised generator is based on the 2024 parameters' distributions. However, there exists a simulation for which the L_ℓ^* value chosen allows a direct comparison with the scenario of 2024, that is, $L_\ell^* = 2.0 \times 10^4\,\mu\mathrm{b}^{-1}\mathrm{Hz}$.

For each year generated, both the *MC* and the *Opt* informations are stored in Python's pickle serialisation format. In particular, for both strategies the total integrated luminosity $\mathcal{L}_{\mathrm{tot}}$ and the total number of fills generated N_{fills} are stored. For the simulator including the probability of failure, also the total number of failures is also stored, N_{fail}. Each fill is stored as a Python dictionary object, in each of which all fill characteristics are stored: the initial intensity N_{i}, the value of the virtual peak luminosity $\hat{L}$, the levelled luminosity value L_ℓ, the value of the luminosity at the end of the fill L_{end}, the time duration of levelling t_ℓ and of the decay part t_{dec}, the characteristics of the DA model $(\varepsilon, \rho, \kappa)$ and the turnaround time t_{ta}. It is clear that, for the *Opt* generator that includes the probability of failure, the dictionary will also record the failure time t_{fail}. In this case, whenever $t_{\mathrm{fail}} < t_\ell$, that is, a failure occurs during the levelling process, L_{end} is set to nan (being equal to L_ℓ) and $t_{\mathrm{dec}} = 0$. In the following, the main results of the two approaches are described.

5.1 Monte Carlo simulation without failure

This section shows the main results of the simulations obtained using the optimisation approach in Eq. (4.6), i.e. the model that does not include the failure probability.

The optimisation approach has been compared with the unoptimised Monte Carlo generated data. The distributions of the mean values for each year have been reported in the following figures, which highlight the main characteristics of the unoptimised approach. The distributions of t_{dec}, t_ℓ, t_{tot}, N_{fill}, L_ℓ, $\hat{L}$, $L_{\mathrm{end}}/\hat{L}$ and $\mathcal{L}_{\mathrm{tot}}$ are reported in Fig. 34 .

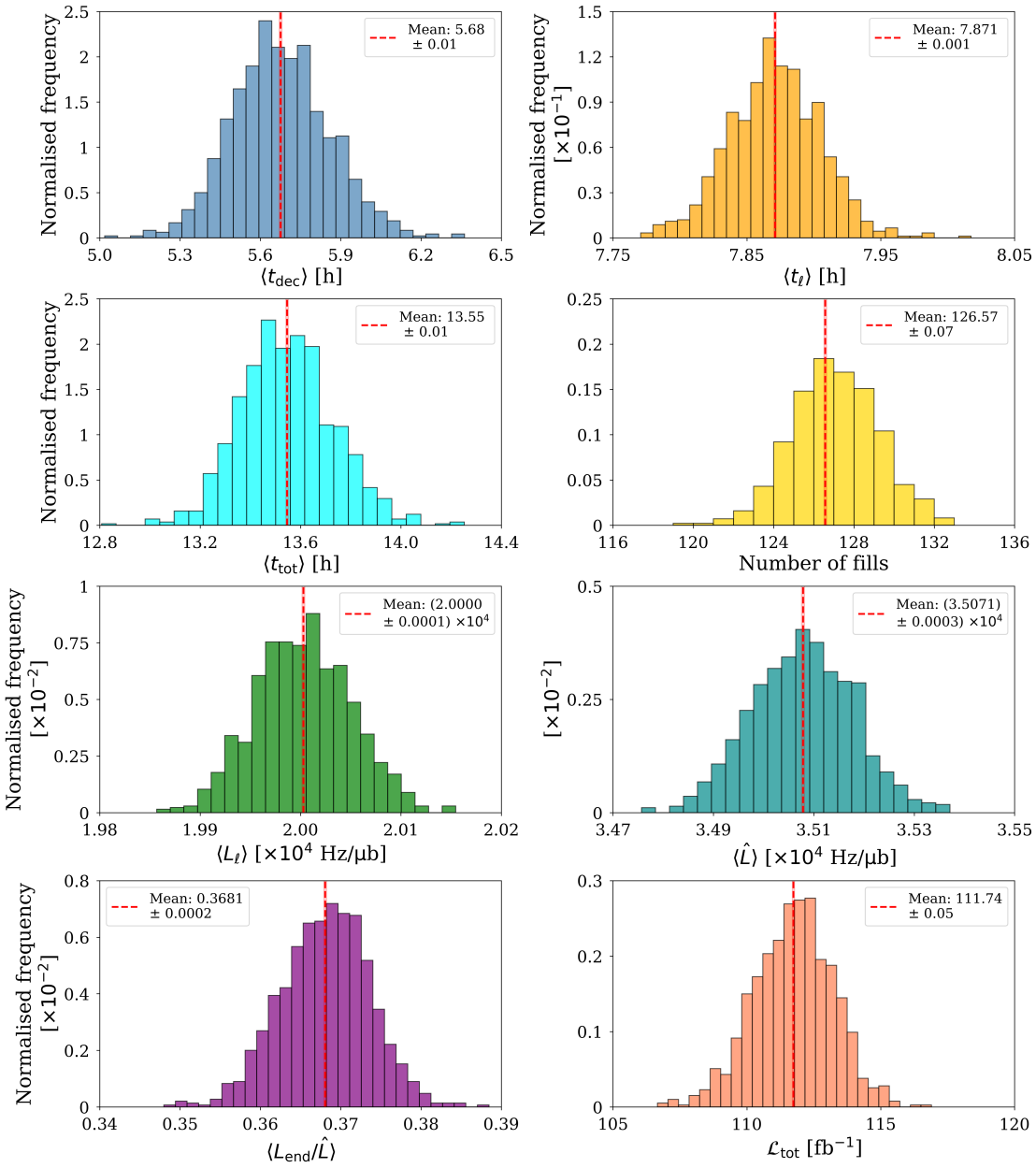

Figure 34: Distributions of t_{dec}, t_ℓ, t_{tot}, N_{fill}, L_ℓ, $\hat{L}$, $L_{\mathrm{end}}/\hat{L}$ and $\mathcal{L}_{\mathrm{tot}}$

The distributions obtained are to be compared with those generated for each analysed case of the simulated optimisation process. However, it should be noted that each *Opt* distribution is compared with the *MC* distribution, generated each time using the 2024 parameter' distributions. This means that the optimisation scheme does not have a direct comparison with its unoptimised case.

In particular, evaluating the optimisation scheme using different values of L_ℓ^*, the results are plotted in Fig. 35, as a function of the ratio of the fixed L_ℓ^* and the mean value of $\langle \hat{L} \rangle$ of each simulated scenario.

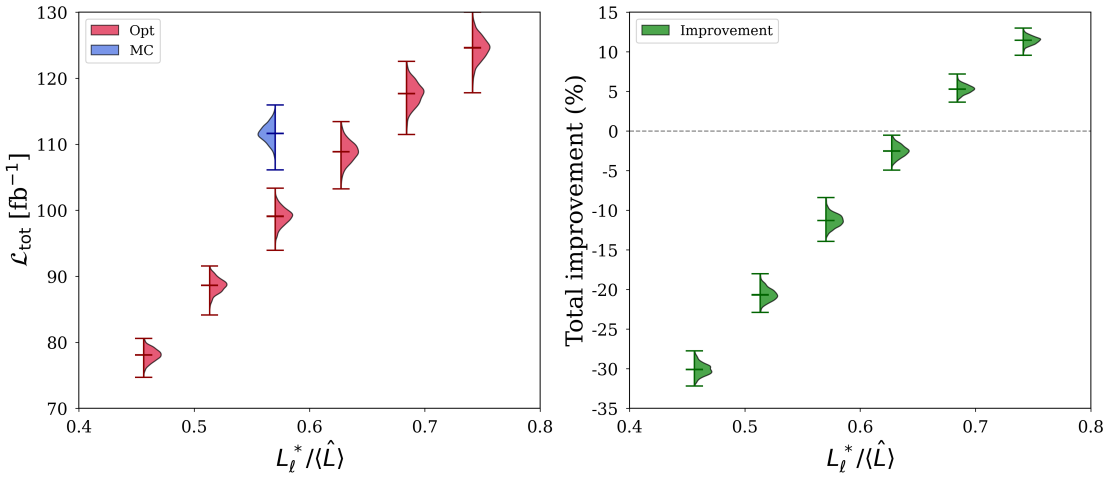

Figure 35: on the left, the violin plots of each $L_\ell^*/\hat{L}$ case of the *Opt*, with a comparison with the *MC* case for $L_\ell^*/\hat{L} = 2 \times 10^4\,\mu\text{b}^{-1}\text{Hz}$; on the right, the violin plots of the improvement of the Opt compared to MC for each $L_\ell^*/\hat{L}$ case.

It is evident that the optimisation scheme, in this framework, is not working as expected. In fact, the optimiser seems to drastically reduce the value of $\mathcal{L}_{\text{int}}$. Even setting $L_\ell^* = 2.0 \times 10^4\,\mu\text{b}^{-1}\text{Hz}$, the optimiser reduces, instead of maximising, the integrated luminosity value per day. In particular, it is evident how the increase in $\mathcal{L}_{\text{tot}}$ starts only for values of $L_\ell^* > 2.0 \times 10^4\,\mu\text{b}^{-1}\text{Hz}$, that is, $L_\ell^* > 2.4 \times 10^4\,\mu\text{b}^{-1}\text{Hz}$ and $L_\ell^* > 2.6 \times 10^4\,\mu\text{b}^{-1}\text{Hz}$. The reason for this behaviour may become clearer by analysing the distributions of the other parameters, in particular t_{dec}, t_ℓ, t_{tot}, and N_{fill}.

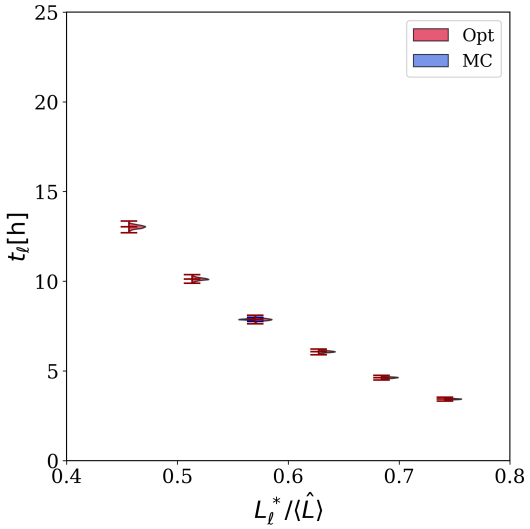

Figure 36: The distributions of the t_ℓ for different values of L_ℓ^*

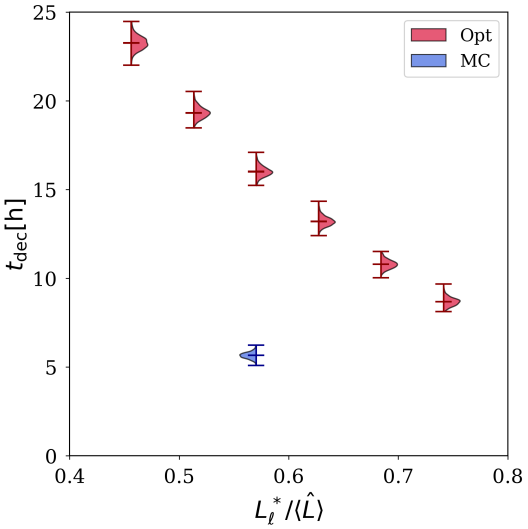

Figure 37: The distributions of the t_{dec} for different values of L_ℓ^*

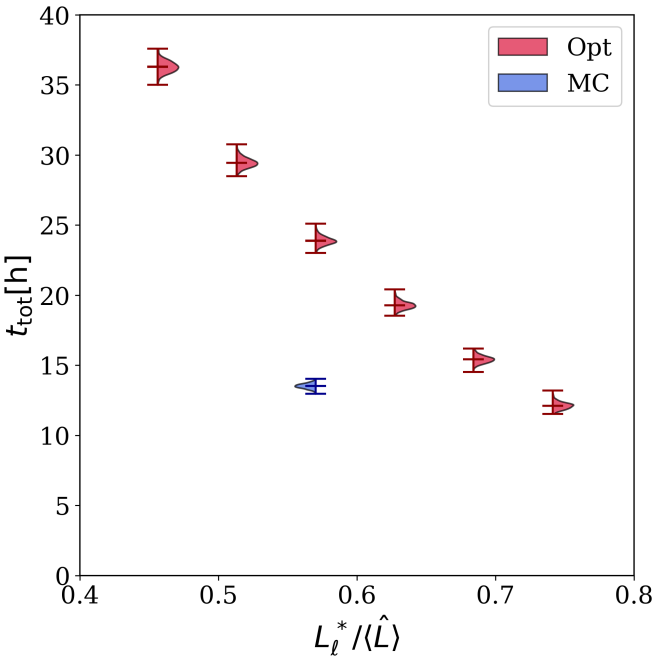

Figure 38: The distributions of the t_{tot} for different values of L_ℓ^*

As is evident, in Fig. 36 the distributions for the levelling time in case $L_\ell^* = 2.0 \times 10^4\,\mu\mathrm{b}^{-1}\mathrm{Hz}$ are the same for the *MC* and the *Opt*. The only difference between the two

approaches is the t_{dec} distributions: in fact, the optimiser tends to drastically increase the duration of the decay part (see Fig. 37), as it cannot find another clever solution. That is, setting the same t_ℓ (as is supposed when building the simulation framework), the optimiser's choice is to drastically elongate the duration of a fill(see Fig. 38), as a way to increase the value $\mathcal{L}_{\mathrm{tot}}$. In addition, the $L_{\mathrm{end}}/\hat{L}$ distributions shown in Fig. 39 seem to confirm that the t_{tot} is deeply elongated.

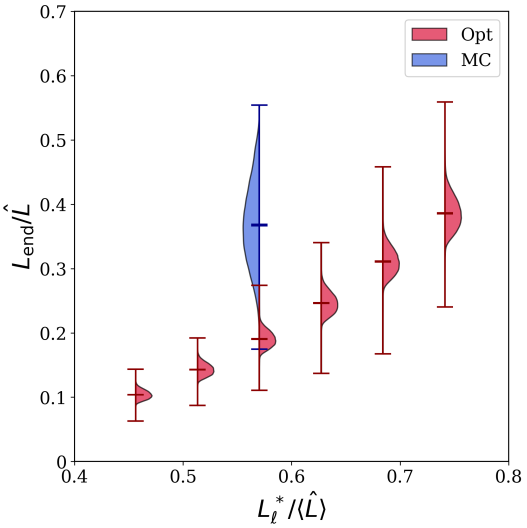

Figure 39: $L_{\mathrm{end}}/\hat{L}$ distributions for each L_ℓ^* case

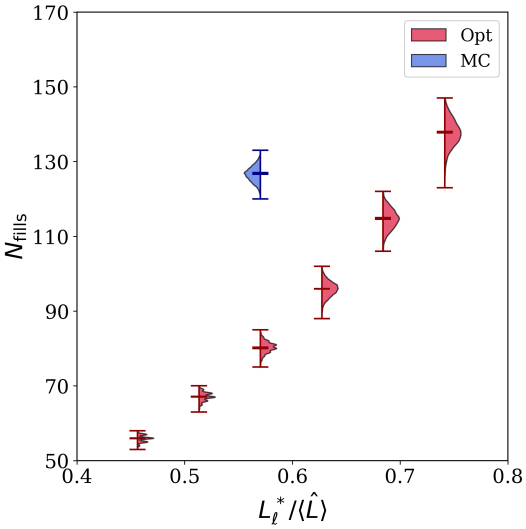

Figure 40: The distributions of the number of fills N_{fill} for each L_ℓ^* case

This is also evident in the remaining simulated scenarios. In particular, setting $L_\ell^* = 1.6 \times 10^4\,\mu\mathrm{b}^{-1}\mathrm{Hz}$, well below the *MC* value. However, increasing the duration of a fill , the number of fills to be generated in a year long run decreases. In fact, as shown in Fig. 40, the number of total fills in a physics run scenario is drastically reduced, in particular for smaller values of L_ℓ^*. As a result, for values of $L_\ell^* < 2.4 \times 10^4\,\mu\mathrm{b}^{-1}\mathrm{Hz}$ the optimisation strategy does not apply. For higher values of L_ℓ^*, the optimiser deals with a relatively short levelling time t_ℓ and a higher luminosity value: increasing the decay part, the increase in $\mathcal{L}_{\mathrm{tot}}$ is quite natural.

It is also important to note that to have additional information about the behaviour of the optimiser, one may analyse how the total time for physics changes. In particular, in this scenario, the optimiser tends to increase, especially for $L_\ell^* < 2.4 \times 10^4\,\mu\mathrm{b}^{-1}\mathrm{Hz}$, the total time for physics, as is evident in Fig. 41.

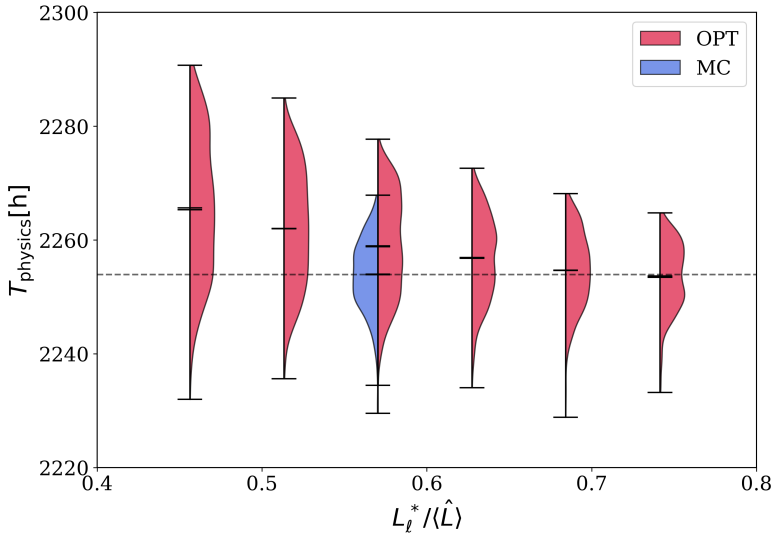

Figure 41: Time for physics distributions for each case studied; the dashed line represents the nominal time for physics for the LHC Run 3

5.2 Monte Carlo simulation with failure

To have a more realistic case of study, the same approach followed for the previous scenario has been implemented in the analysis of the system, including a failure probability. The optimisation scheme analysed is the one presented in Eq. (4.26). Clearly, the failure probability is present both in the *MC* and in the *Opt* approaches. For the *MC*, some statistics are reported as in the previous section, to set the comparison with the optimised model. In particular, t_{dec}, t_ℓ, t_{tot}, N_{fill}, t_{fail},N_{fail}, L_ℓ, $\hat{L}$, $L_{\text{end}}/\hat{L}$, $\mathcal{L}_{\text{tot}}$ are shown in Fig. 42. It is evident how, comparing the distributions with those of the previous case (see Fig 34), some differences are present. In particular, while the distributions for L_ℓ and $\hat{L}$ admit the same mean value, some deviations are observed in all other distributions. Indeed, the mean values of the distributions of t_{dec}, t_ℓ and t_{tot} are reduced compared to those of Fig 34: this is attributed to the inclusion of failure probability of a fill, which acts as a reducing factor of the fill duration. The distributions for the failure time, t_{fail}, and the number of failures, N_{fail}, are reported in Fig. 42. It is evident that reducing the fill duration leads to an increase in the number of N_{fill}, compared to the case without failure. Furthermore, the shorter fill duration affects the ratio $L_{\text{end}}/\hat{L}$: the longer t_{dec} of the no-failure scenario allows the luminosity to decrease to lower L_{end} values, resulting in a lower $L_{\text{end}}/\hat{L}$, compared to the case with failure. Consequently, the presence of failures limits the integrated luminosity over one year,$\mathcal{L}_{\text{tot}}$ compared to the no-failure scenario.

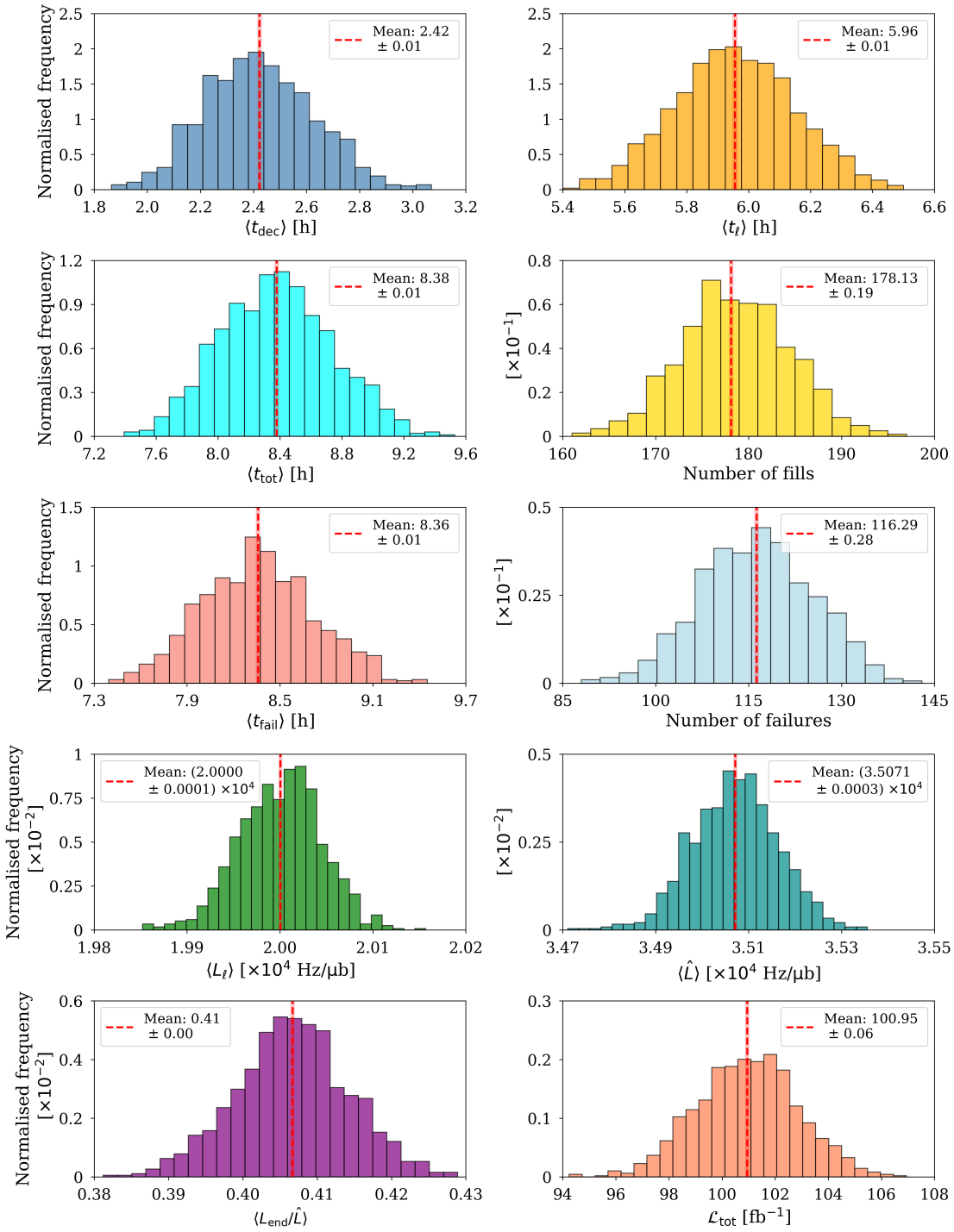

Figure 42: Distributions of t_{dec}, t_ℓ, t_{tot}, N_{fill}, t_{fail},N_{fail}, L_ℓ, $\hat{L}$, $L_{\mathrm{end}}/\hat{L}$, $\mathcal{L}_{\mathrm{tot}}$

As in the previous case, the results of the application of the optimisation scheme

are shown below. It is interesting to note that, introducing the failure probability, the optimiser behaviour changes compared to the previous case. In particular, analysing the results in Fig. 43, optimisation seems possible since $L_\ell^* = 2.0 \times 10^4\,\mu\mathrm{b}^{-1}\mathrm{Hz}$. In fact, the distribution of the $\mathcal{L}_{\mathrm{tot}}$ for the *Opt* case is slightly shifted toward higher values compared to the distribution of the *MC* case. Also, the mean value of the two distributions shows this result. Looking at the right side of Fig. 43, for case $L_\ell^* = 2.0 \times 10^4\,\mu\mathrm{b}^{-1}\mathrm{Hz}$ the increase distribution is concentrated almost entirely in positive values. Furthermore, for higher values of the parameter L_ℓ^*, the gain in $\mathcal{L}_{\mathrm{tot}}$ seems to improve.

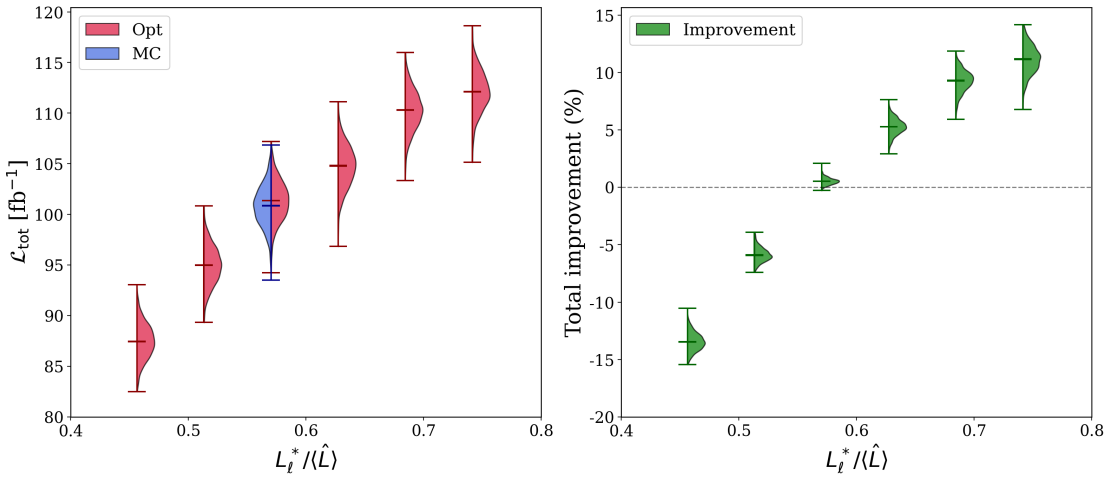

Figure 43: In the plot, the distribution of $\mathcal{L}_{\mathrm{tot}}$ for each L_ℓ^* analysed

In this scenario, the optimiser seems to behave in a completely different way with respect to the previous case. In fact, as may be evident considering Fig. 45, the t_{dec} values are much shorter, even considering the existing failure probability, with respect to the scenario without failure probability. Its value is still slightly elongated by the optimiser increasing the L_ℓ^* value, but in conjunction with a shortening of the t_ℓ (see Fig. 44). The optimiser seems to find the best solution in creating shorter fills and increasing the number of fills for each year (as shown in Figs. 47 and 46). Thus, increasing the L_ℓ^* value together with a reduction in the fill duration, the optimiser seems to be able to effectively solve the problem.

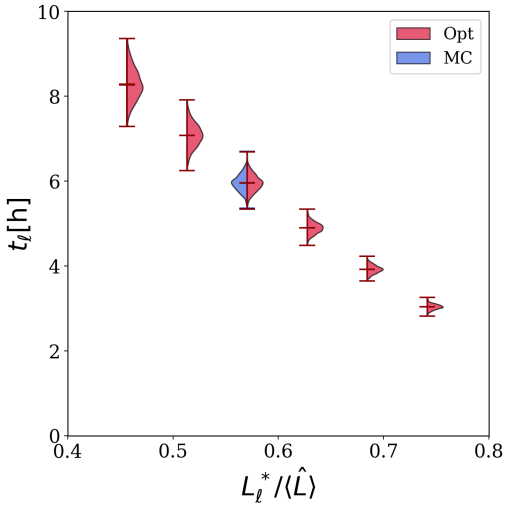

Figure 44: Distribution of the t_ℓ parameter for different L_ℓ^*

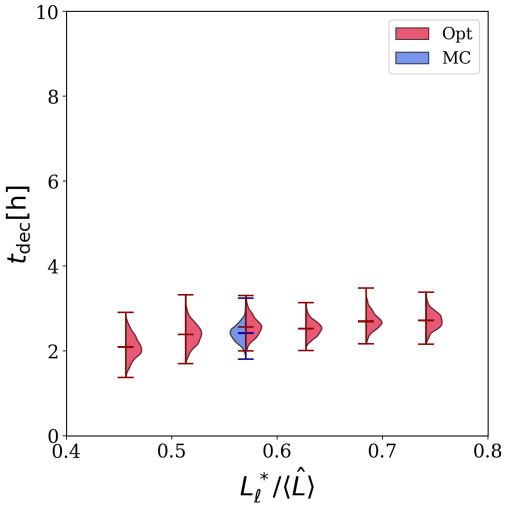

Figure 45: Distribution of the t_{dec} parameter for different L_ℓ^*

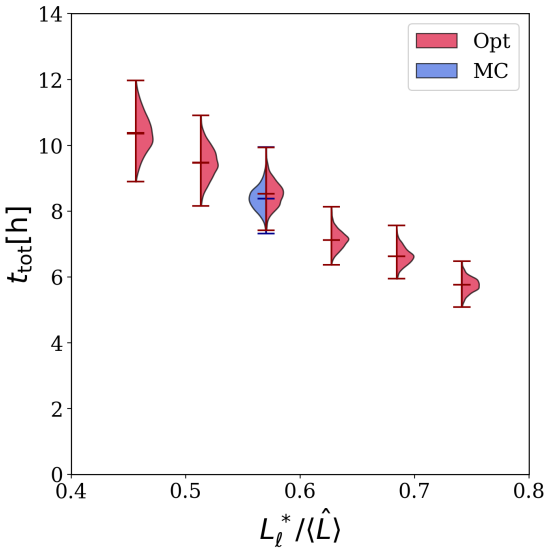

Figure 46: Distribution of the t_{tot} parameter for different L_ℓ^*

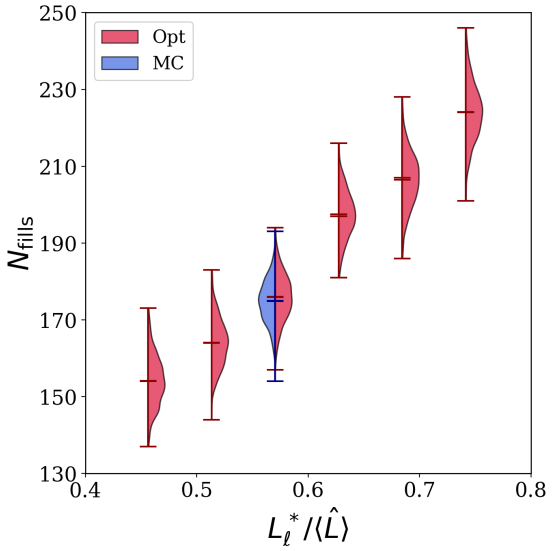

Figure 47: N_{fill} distributions for different value of the L_ℓ^*

Additional information is reported in Figs. 48 and 49, on the number of failed fills N_{fail} and $L_{\text{end}}/\hat{L}$. In particular, failure was shown to affect primarily the levelled part of the fill for a lower value of L_ℓ^* and the decay part of it for higher values of the parameter: for $L_\ell^* = 1.6\times10^4\,\mu\text{b}^{-1}\text{Hz}$, the percentage of fills that failed was $\approx 64\%$ during levelling and $\approx 35\%$ during decay; in contrast, for $L_\ell^* = 2.6\times10^4\,\mu\text{b}^{-1}\text{Hz}$, the percentage of fills that failed was $\approx 22\%$ during levelling and $\approx 77\%$ during decay.

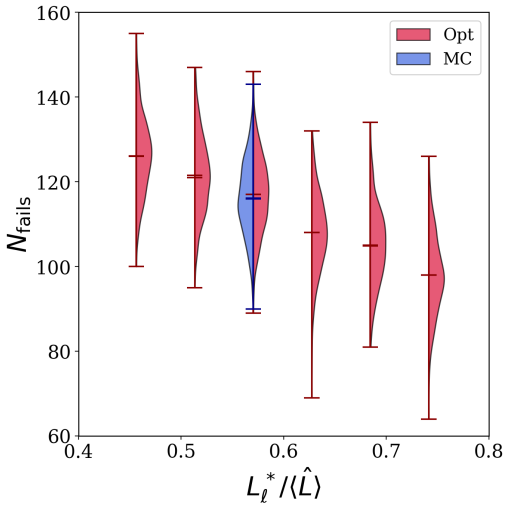

Figure 48: N_{fail} distributions for different value of the L_ℓ^*

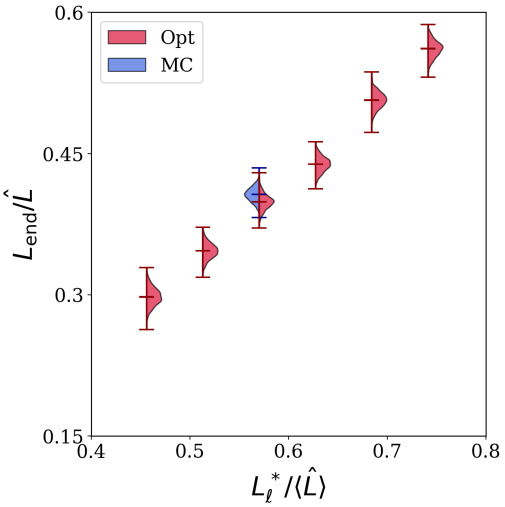

Figure 49: $L_{\text{end}}/\hat{L}$ distributions for different value of the L_ℓ^*

Note that during all the simulations, a control of the total physics time has to be accounted for. In fact, the optimiser must not resolve the issue by elongating the total time for physics. In particular, for each case analysed, It seemed that the optimiser did not exceed the total time given, with a tendency, instead, to slightly reduce the total time as L_ℓ^* increases, as shown in Fig. 50.

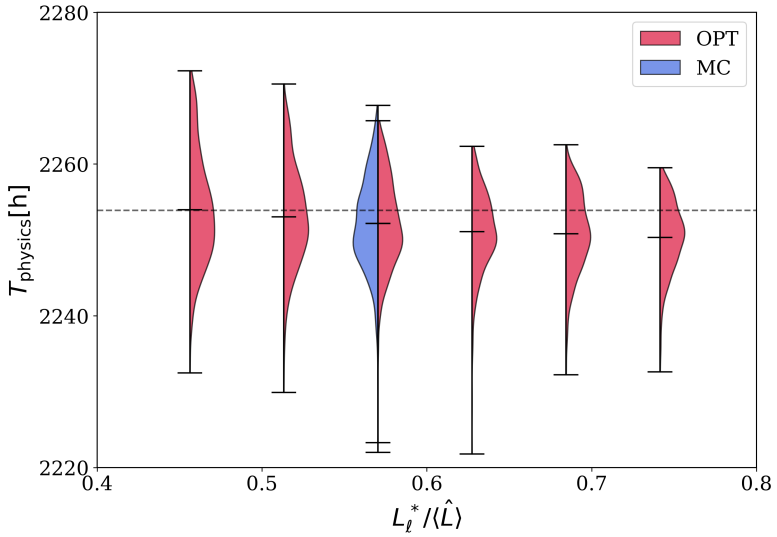

Figure 50: Total time for physics distributions for each case studied; the dashed line represents the nominal time for physics for the LHC Run 3

6 Conclusions and outlook

In this work, a model to define the levelling scheme through variation of β^* has been developed and studied (2). Furthermore, a model addressing the problem of integrated luminosity optimisation in the presence of luminosity levelling has been proposed. Its theoretical behaviour and statistical performance have been evaluated both through analytical methods (4) and through numerical methods (5).

The results are encouraging, as a path to solving the problem of maximising the integrated luminosity has been traced, although some limitations must be taken into account.

The optimisation scheme presented in Subsection 4.3, which also incorporates $L_{\ell,\mathrm{f}}$ and $L_{\ell,\mathrm{c}}$ as optimisation parameters, should be evaluated to assess whether the optimisation strategy would follow the same behaviour observed in the present analysis, or whether a different scenario would arise.

The levelling model considered in this work is the pure variation of β^*. It is possible that a more comprehensive approach to the overarching problem would involve analysing a levelling strategy that includes additional levelling methods and exploring their optimal combination. Within such a framework, the problem of maximising integrated luminosity may find an alternative and potentially more effective solution.

7 Acknowledgements

From this thesis, I take home not so much the final result, which remains a work in progress, still subject to improvements and revisions, but rather the journey itself.

I would like to sincerely thank my supervisor, Professor Massimo Giovannozzi, for guiding me through this path and for teaching me that doing research is not merely about publishing one paper after another. It is about taking a problem, analysing it in depth, making mistakes, revisiting it, and searching for a solution with persistence and rigour. He taught me the importance of critically reading results, of self-reflection, and that teamwork is essential: collaboration should always be sought, never neglected.

I also would like to thank my co-supervisors: Maria, the PhD student who assisted me throughout this work, whose calmness and dedication I deeply appreciated. Without her, this thesis would not have been the same. I am equally grateful to Federico, for his invaluable help in implementing the simulation code, and for his thoughtful corrections and advice.

I am deeply grateful to my family, without whom this journey would not have been possible. By family, I mean the entire network of friends and relatives who have never failed to offer their support and encouragement. My father and my legion of *aunts*, not by blood but by affection.

I would also like to thank my friends for their unwavering support and for always lending an ear: my dear friend Chiara, and my friends scattered across Emilia, from Parma to Bologna. Special thanks go to Lu, Licia, and Simo for always being there when it mattered most.

Finally, I want to thank Luca, without whose love, care, attention, and support I would not be the person I am today.

Appendix

A. 2024 analysis: further details

Some additional parameters have been analysed during the data analysis, but they have not been selected to perform the Monte Carlo simulation. In particular, the distribution of the levelling time t_ℓ and the distribution of the intensity at levelling time $N(t_\ell)$.

In particular, the t_ℓ data were distributed according to a double gaussian distribution, showing two different peaks. The analysis seems to be supported by the scattered plot, where two main data cores seemed evident. However, the lack of data in between may be related to the failure probability of a fill, or the data selected and recorded. In this scenario, the distribution may be reveal to be a uniform one.

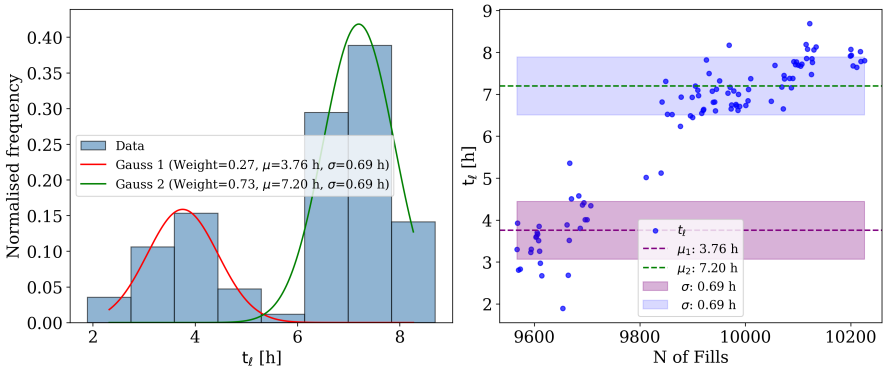

Figure 51: On the left, the distribution of the t_ℓ data, on the right, the scattered plot

Also for the $N(t_\ell)$ values, data seemed to follow a double gaussian distribution, with two cores in the scattered plot.

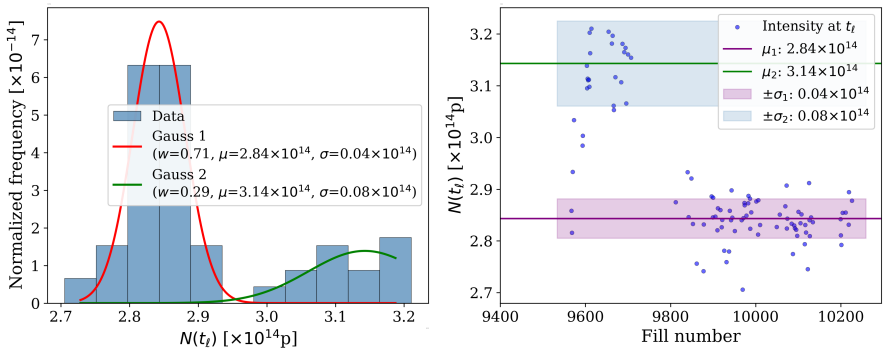

Figure 52: On the left, the distribution of the $N(t_\ell)$ data, on the right, the scattered plot

B. Run 3 analysis: further details

All the values of the examined parameter for the three years have been reported in the following table

Table 2: Statistical analysis of each parameter for years 2022, 2023 and 2024

Parameter	Year	Mean	Standard deviation
L_ℓ [$\mu b^{-1} Hz$]	2022	1.61×10^4	1.08×10^3
	2023	1.94×10^4	2.32×10^2
	2024	1.99×10^4	5.7×10^2
t_ℓ [h]	2022	3.54	1.99
	2023	3.77	0.75
	2024	3.75	0.66
		7.20	0.65
t_{dec} [h]	2022	7.68	3.40
	2023	7.31	1.62
	2024	5.75	2.26
N_i [p]	2022	3.04×10^{14}	2.65×10^{13}
	2023	3.56×10^{14}	2.00×10^{13}
	2024	3.75×10^{14}	6.70×10^{12}
$N(t_\ell)$ [p]	2022	2.62×10^{14}	1.62×10^{13}
	2023	2.83×10^{14}	4.10×10^{12}
		3.01×10^{14}	9.96×10^{12}
	2024	2.84×10^{14}	3.80×10^{12}
		3.14×10^{14}	8.22×10^{12}
t_{ta} [h]	2022	3.16	0.45
	2023	4.94	0.75
	2024	2.52	0.19
TBF [h]	2022	15.57	3.17
	2023	16.14	3.52
	2024	12.42	1.24

In addition, the data for the DA model are presented for each year:

Table 3: DA model parameters for Run 3

Year	κ	ε	ρ
2022	0.94	$(3.39 \pm 0.30) \times 10^{-24}$	219 ± 13
2023	0.92	$(3.79 \pm 0.21) \times 10^{-24}$	206 ± 9
2024	0.92	$(3.66 \pm 0.26) \times 10^{-24}$	210 ± 15

References

[1] American Institute of Physics. *Ernest O. Lawrence and the EPA (Electromagnetic Proton Accelerator)*. Web Exhibit. Consulted on 18/08/2025. 2021. URL: https://history.aip.org/exhibits/lawrence/epa.htm.

[2] L. Bonolis. "Una rivoluzione culturale nel mondo degli acceleratori di particelle: Bruno Touschek e il primo anello di collisione materia-antimateria". In: *Le Scienze* (Sept. 2008). Numero speciale: settembre 2008. URL: https://www.analysis-online.net/wp-content/uploads/2013/03/bonolis_rivoluzione.pdf.

[3] American Physical Society. "This Month in Physics History: June 1930: Lawrence's First Cyclotron". In: *APS News* 12.6 (June 2003). URL: https://www.aps.org/apsnews/2003/06/lawrence-first-cyclotron.cfm.

[4] American Institute of Physics. *The First Cyclotrons – Ernest Lawrence and the Cyclotron*. Web Exhibit. Consulted on 18/08/2025. 2021. URL: https://history.aip.org/exhibits/lawrence/first.htm.

[5] D. W. Kerst. "The Acceleration of Electrons by Magnetic Induction". In: *Phys. Rev.* 60 (1 July 1941), pp. 47–53. DOI: 10.1103/PhysRev.60.47. URL: https://link.aps.org/doi/10.1103/PhysRev.60.47.

[6] CERN Courier. *A comparison*. Web page. Consulted on 18/08/2025. URL: https://cerncourier.com/a/a-comparison/.

[7] CERN. *CERN70: The heart of CERN's accelerator chain*. Web article. Consulted on 18/08/2025. URL: https://home.cern/news/series/cern70/cern70-heart-cerns-accelerator-chain.

[8] L. Bonolis and G. Pancheri. "Bruno Touschek: Particle physicist and father of the e^+e^- collider". In: *Eur. Phys. J. H* 36 (2011), pp. 1–61. DOI: 10.1140/epjh/e2011-10044-1. arXiv: 1103.2727 [physics.hist-ph].

[9] A. De Roeck. "Physics at the Electron-Proton Collider Hera". In: *NATO Sci. Ser. C* 554 (2000). Ed. by W. Kittel, PJ. Mulders, and O. Scholten, pp. 353–383. DOI: 10.1007/978-94-011-4126-0_13.

[10] CERN. *The LEP story*. Press Release. Consulted on 18/08/2025. June 2003. URL: https://home.cern/news/press-release/cern/lep-story.

[11] High Energy Accelerator Research Organization (KEK). *High Energy Accelerator Research Organization (KEK)*. Website. Consulted on 18/08/2025. 2025. URL: https://www.kek.jp/en/.

[12] Brookhaven National Laboratory. *SuperKEKB Collider Achieves the World's Highest Luminosity*. Newsroom Article. Consulted on 18/08/2025. June 2020. URL: https://www.bnl.gov/newsroom/news.php?a=117285.

[13] A. Kazunori, F. Kazuro, and K. Haruyo. “SuperKEKB collider”. In: *Nuclear Instruments and Methods in Physics Research Section A: Accelerators, Spectrometers, Detectors and Associated Equipment* 907 (Nov. 2018), pp. 188–199. ISSN: 0168-9002. DOI: 10.1016/j.nima.2018.08.017. URL: http://dx.doi.org/10.1016/j.nima.2018.08.017.

[14] M. Meddahi et al. “Chapter 21: Beam from Injectors: The LHC Injectors Upgrade (LIU) Project”. In: *Adv. Ser. Direct. High Energy Phys.* 31 (2024). Ed. by Oliver Brüning and Lucio Rossi, pp. 457–473. DOI: 10.1142/9789811278952_0021.

[15] R. Steerenberg. *Rende Steerenberg, Head of the Operations Group in the Beams Department – Run 3 of the LHC*. June 2022. DOI: 10.17181/videos.2296146. URL: https://videos.cern.ch/record/2296146.

[16] M. Chalmers. “Discovery machines”. In: *CERN Courier* (June 2024). Consulted on 18/08/2025. URL: https://cerncourier.com/a/discovery-machines/.

[17] O. Bruning et al. *LHC Design Report Volume I: The LHC Main Ring*. Design Report CERN-2004-003. Editorial Board. CERN, 2004, pp. 21–42. URL: http://cds.cern.ch/record/782076.

[18] V. Frigo. “LHC structure.” AC Collection. Legacy of AC. Pictures from 1992 to 2002. 1997. URL: https://cds.cern.ch/record/842611.

[19] H. Bartosik and G. Rumolo. *Performance of the LHC injector chain after the upgrade and potential development*. 2022. arXiv: 2203.09202 [physics.acc-ph]. URL: https://arxiv.org/abs/2203.09202.

[20] A. A. Gorzawski. “Luminosity control and beam orbit stability with beta star leveling at LHC and HL-LHC”. PhD thesis. Ecole Polytechnique, Lausanne, 2016. DOI: 10.5075/epfl-thesis-7338.

[21] T. Zolkin. “Sector magnets or transverse electromagnetic fields in cylindrical coordinates”. In: *Physical Review Accelerators and Beams* 20.4 (Apr. 2017). ISSN: 2469-9888. DOI: 10.1103/physrevaccelbeams.20.043501. URL: http://dx.doi.org/10.1103/PhysRevAccelBeams.20.043501.

[22] *CAS - CERN Accelerator School : 5th Advanced Accelerator Physics Course*. CERN. Geneva: CERN, 1995. DOI: 10.5170/CERN-1995-006. URL: https://cds.cern.ch/record/254747.

[23] C. Bernardini et al. “Measurements of the rate of interaction between stored electrons and positrons”. In: *Il Nuovo Cimento (1955-1965)* 34 (1964), pp. 1473–1478. DOI: 10.1007/BF02750550.

[24] R. W. Assmann et al. *A Brief History of the LEP Collider*. Tech. rep. CERN-SL-2002-009-DI. CERN, 2002. URL: https://cds.cern.ch/record/590837.

[25] H. Burkhardt et al. *LEP Operation and Performance with Electron-Positron Collisions at 209 GeV*. Tech. rep. CERN-SL-2001-003-BI. CERN, 2001. URL: https://cds.cern.ch/record/484968.

[26] KEK. *SuperKEKB collider achieves the world's highest luminosity*. KEK Press Release. June 2020. URL: https://www.kek.jp/en/newsroom/2020/06/26/1400/.

[27] J. Seeman et al. "PEP-II at 1.2×10^{34}/cm^2/s luminosity". In: *Proceedings of PAC07*. IEEE, 2007. URL: https://proceedings.jacow.org/p07/PAPERS/MOZAKI03.PDF.

[28] CERN. *LHC Report: Protons: mission accomplished*. CERN News. Oct. 2018. URL: https://home.cern/news/news/physics/lhc-report-protons-mission-accomplished.

[29] K. Wille. *The Physics of Particle Accelerators: An Introduction*. Oxford University Press, Feb. 2001. ISBN: 9780198505501. DOI: 10.1093/oso/9780198505501.001.0001. URL: https://doi.org/10.1093/oso/9780198505501.001.0001.

[30] W. Herr and B. Muratori. *Concept of luminosity*. Tech. rep. Cern, 2006. DOI: 10.5170/CERN-2006-002.361. URL: https://cds.cern.ch/record/941318.

[31] A. Bazzani et al. "Advances on the modeling of the time evolution of dynamic aperture of hadron circular accelerators". In: *Phys. Rev. Accel. Beams* 22 (10 Oct. 2019), p. 104003. DOI: 10.1103/PhysRevAccelBeams.22.104003. URL: https://link.aps.org/doi/10.1103/PhysRevAccelBeams.22.104003.

[32] M. Giovannozzi and F. F. Van Der Veken. "Description of the luminosity evolution for the CERN LHC including dynamic aperture effects, Part I: The model". In: *Nuclear Instruments and Methods in Physics Research Section A: Accelerators, Spectrometers, Detectors and Associated Equipment* 905 (Oct. 2018), pp. 171–179. ISSN: 0168-9002. DOI: 10.1016/j.nima.2018.07.063. URL: http://dx.doi.org/10.1016/j.nima.2018.07.063.

[33] M. Giovannozzi and F. F. Van Der Veken. "Description of the luminosity evolution for the CERN LHC including dynamic aperture effects. Part II: application to Run 1 data". In: *Nuclear Instruments and Methods in Physics Research Section A: Accelerators, Spectrometers, Detectors and Associated Equipment* 908 (Nov. 2018), pp. 1–9. ISSN: 0168-9002. DOI: 10.1016/j.nima.2018.08.019. URL: http://dx.doi.org/10.1016/j.nima.2018.08.019.

[34] T. Amezza. "Dynamic aperture model for LHC integrated luminosity optimisation". MA thesis. Alma Mater University of Bologna, 2023. URL: https://amslaurea.unibo.it/id/eprint/30109/.

[35] T Pieloni and B Muratori. *Luminosity levelling techniques for the LHC*. en. 2014. DOI: 10.5170/CERN-2014-004.177. URL: http://cds.cern.ch/record/1957033.

[36] M. Benedikt, D. Schulte, and F. Zimmermann. "Optimizing integrated luminosity of future hadron colliders". In: *Phys. Rev. ST Accel. Beams* 18 (10 Oct. 2015), p. 101002. DOI: 10.1103/PhysRevSTAB.18.101002. URL: https://link.aps.org/doi/10.1103/PhysRevSTAB.18.101002.

[37] M. Lamont. "LHC Report: playing with angles". In: *CERN Bulletin* 38 (2016). URL: https://cds.cern.ch/journal/CERNBulletin/2016/38/News%20Articles/2216373.

[38] LHC Team. *LHC Report: The LHC is full!* Tech. rep. CERN News. CERN, May 2018. URL: https://home.cern/news/news/accelerators/lhc-report-lhc-full.

[39] B. Salvachúa. "LHC Luminosity Levelling and Beam". In: *ICFA Mini-Workshop on Beam-Beam Effects in Circular Colliders*. Presented at the Beam-Beam Workshop 2018. Berkeley, USA, Feb. 2018. URL: https://indico.physics.lbl.gov/event/586/contributions/1434/attachments/1319/1465/LHC-LumiLeveling-BB-Belen.pdf (visited on 08/22/2025).

[40] F. Marcastel. *New technologies for the High-Luminosity LHC*. General Photo. 2015. URL: https://cds.cern.ch/record/2063308.

[41] O Brüning and L Rossi. *Chapter 1: High-Luminosity Large Hadron Collider*. Tech. rep. CERN, 2020, pp. 1–16. DOI: 10.23731/CYRM-2020-0010.1. URL: https://cds.cern.ch/record/2750437.

[42] G. Arduini et al. *Chapter 2: Machine layout and performance*. Tech. rep. CERN, 2020, pp. 17–46. DOI: 10.23731/CYRM-2020-0010.17. URL: https://cds.cern.ch/record/2750438.

[43] F. Capoani et al. *Optimisation of integrated luminosity in a circular collider with application to the LHC Run 2*. 2025. arXiv: 2504.12751 [physics.acc-ph]. URL: https://arxiv.org/abs/2504.12751.

[44] R. L. Harrison. "Introduction To Monte Carlo Simulation". In: *AIP Conference Proceedings* 1204 (Jan. 2010), pp. 17–21. DOI: 10.1063/1.3295638.

[45] J. Qiang. *Monte Carlo Simulation Techniques*. 2020. arXiv: 2006.10506 [physics.comp-ph]. URL: https://arxiv.org/abs/2006.10506.